UNIVERSITY OF CALIFORNIA, SAN DIEGO

On breaking waves and turbulence at the air-sea interface

A dissertation submitted in partial satisfaction of the
requirements for the degree
Doctor of Philosophy

in

Oceanography

by

Peter Sutherland

Committee in charge:

W. Kendall Melville, Chair
Walter Munk
Daniel L. Rudnick
Sutanu Sarkar
Jerome A. Smith

2013

The dissertation of Peter Sutherland is approved, and it is acceptable in quality and form for publication on microfilm and electronically:

_____

_____

_____

_____

_____
Chair

University of California, San Diego

2013

EPIGRAPH

"Now when I was a little chap I had a passion for maps. I would look for hours at South America, or Africa, or Australia, and lose myself in all the glories of exploration. At that time there were many blank spaces on the earth, and when I saw one that looked particularly inviting on a map (but they all look that) I would put my finger on it and say, 'When I grow up I will go there.' The North Pole was one of these places, I remember. Well, I haven't been there yet, and shall not try now. The glamour's off. Other places were scattered about the hemispheres. I have been in some of them, and... well, we won't talk about that. But there was one yet – the biggest, the most blank, so to speak – that I had a hankering after."

—Charlie Marlow, Heart of Darkness

TABLE OF CONTENTS

Signature Page iii

Epigraph iv

Table of Contents v

List of Figures vii

Acknowledgements xvii

Vita, Publications, and Fields of Study xix

Abstract of the Dissertation xx

Chapter 1 Introduction 1

Chapter 2 Experiments 4
2.1 Experimental setup 4
2.2 Field sites 7

Chapter 3 Stereo IR PIV processing 14

Chapter 4 Infrared measurements of Breaking Statistics 21
4.1 Introduction 21
4.2 Breaker Detection 23
4.2.1 Reflections in IR imagery 30
4.2.2 Visible breaker detection 32
4.3 Results 32
4.4 Scaling $\Lambda(c)$ 36
4.5 Discussion 40

Chapter 5 Measurements of surface and near-surface turbulence 47
5.1 Introduction 47
5.2 Separation of waves from turbulence 50
5.2.1 Helmholtz decomposition 50
5.2.2 Surface vorticity 51
Vertical vorticity (method of *Meyer et al.* 2001) . 51
Surface-normal vorticity (circulation method) . . 53
Vorticity spectra 54
5.3 Surface TKE Dissipation 58
5.3.1 Inertial subrange fit 58
5.3.2 Vorticity spectrum fit 59

5.3.3 Inertial scaling 61
5.3.4 Comparison of methods 62
5.4 Sources of error 64
5.5 Subsurface turbulence 65
5.6 Discussion 74
5.6.1 Integrated dissipation 82
5.6.2 Sampling an intermittent process 85
5.6.3 Wave coherence 86

Chapter 6 Conclusions 91

Appendix A Expected form of $\Lambda(\boldsymbol{c})$ 94

Appendix B Review of spectra of turbulence 96
B.1 Introduction 96
B.2 Isotropic turbulence 98
B.3 Vorticity spectra and dissipation 99
B.4 Two-dimensional turbulence 100
B.4.1 2D Isotropic Turbulence 102
B.4.2 Vorticity spectra in 2D turbulence 104

Appendix C Instrument wakes in a wave field with a mean flow. 106

Appendix D Energy input definitions 108

LIST OF FIGURES

Figure 2.1: Schematic of the instrument configuration aboard R/P FLIP during the SoCal 2010 experiment. The configuration during the RaDyO 2009 experiment was similar, but instruments were mounted on the opposite (port) boom. 5
Figure 2.2: Photo looking outwards along FLIP's port boom during the RaDyO 2009 experiment. 6
Figure 2.3: Subsurface lowered turbulence measurement device (LTMI). Not shown is a vane designed to keep the body of the Aquadopp orthogonal to the mean flow, with beam 2 pointing up-stream. . 7
Figure 2.4: 20-minute average wind and wave conditions during RaDyO 2009 experiment. The top panel shows wind speeds, U_{10}, as black circles connected by a black line, and wind directions as gray circles. The bottom panel shows significant wave height, H_s. 8
Figure 2.5: 20-minute average wind and wave conditions during Southern California 2010 experiment. The top panel shows wind speeds, U_{10}, as black circles, and wind directions as gray circles. The bottom panel shows significant wave height, H_s. 9
Figure 2.6: 20-minute average wind and wave conditions during the HiRes 2010 experiment. The top panel shows wind speeds, U_{10}, as black circles, and wind directions as gray circles. The bottom panel shows significant wave height, H_s. 10
Figure 2.7: Relationship between wind speed and wave age during these experiments. Each point represents a 20-minute average. Triangles are from the RaDyO 2009 experiment, circles are from the SoCal 2010 experiment. 11

Figure 3.1: Schematic overview of stereo IR processing sequence. Green boxes indicate input of raw images (with artifacts and mean removed). Yellow boxes are processing steps. White boxes are analysis steps. Sampling rates are indicated where appropriate. 15
Figure 3.2: Example stereo IR reconstruction of the sea surface. Images were taken starting at 2009/09/08 11:07:29.25 [UTC] and are separated by 0.25 s. Coloring shows surface temperature anomaly and black arrows show surface velocity. Arrows have been decimated to 1/4 resolution and scaled to 10%; a 10 cm arrow indicates 1 m/s velocity. The corresponding vorticity fields are shown in figure 3.3 19

Figure 3.3: Example stereo IR reconstruction of the sea surface showing surface vertical vorticity field. The corresponding temperature and velocity fields shown in figure 3.2. Images were taken starting at 2009/09/08 11:07:29.25 [UTC] and are separated by 0.25 s. The vorticity has been filtered with a 20 cm 2D Gaussian filter in order to highlight larger scale structure around the breaker. . 20

Figure 4.1: Measured $\Lambda(c)$ compared with the literature. Lines colored by wave age are from this work. Thick black lines are from the laboratory measurements of *Jessup and Phadnis* (2005). Field measurements are from: *Melville and Matusov* (2002) lines with small dots, *Gemmrich et al.* (2008) lines with squares, *Phillips et al.* (2001) lines with triangles, and *Kleiss and Melville* (2010) solid gray lines. The black and white dashed line is the modeled extrapolation by *Romero et al.* (2012) of the measurements of *Kleiss and Melville* (2010). Horizontal bars near the top indicate standard deviation of velocity error, calculated using synthetic data. 24

Figure 4.2: Example breaker detection sequence. a) Raw image with data cable and 20-minute mean removed. b) Image entropy (red corresponds to high entropy, blue to low). c) Regions above entropy threshold are selected (gray regions). d) Actively breaking fronts selected (black arrows). The final step is conversion from image to earth coordinates. The result is shown in Figure 4.7. 26

Figure 4.3: Probability density function of IR image entropy for a single example image (taken December 6, 2010 22:00 [UTC]) showing the features used for calculating the entropy threshold. $P_{E=1}$, the value of the PDF at an entropy value of $E = 1$ was found (point a). Then the lowest entropy value for which the distribution exceeded $1.2 \times P_{E=1}$ was located (point b) and set as the entropy threshold, $E_{threshold}$. 27

Figure 4.4: Typical sensitivity to entropy threshold used in breaker detection. 20-minute average breaker front length distribution starting December 6, 2010 22:00 [UTC]. (a) Log coordinates. (b) Linear coordinates. The black curve shows the value used in this analysis, with the entropy distribution at the threshold, $P_{E=E_{thresh}}$, equal to 1.2 times the entropy distribution value at $E = 1$, $P_{E=1}$. Choosing $P_{E=E_{thresh}} = 1.1 \times P_{E=1}$ gives the red curve, and choosing $P_{E=E_{thresh}} = 1.3 \times P_{E=1}$ gives the blue one. Clearly $\Lambda(c)$ has a dependence on the chosen threshold. However, for slow breakers, with c less than approximately 2 m/s, $\Lambda(c)$ is relatively insensitive to small changes in threshold value. For fast breakers the sensitivity is greater, but the threshold was chosen so that breakers detected in IR agreed with those detected in visible imagery at those speeds. 28

Figure 4.5: Effect of reflections from *FLIP*'s structure on 20-minute average $\Lambda(c)$, starting December 7, 2010 08:00 [UTC]. (a) Log coordinates. (b) Linear coordinates. Distributions calculated using the whole image, the bottom half (with reflections), or the top half (without reflections). This time period was chosen to be local midnight to ensure that the only reflections present would be from the vessel's booms and structure, not sunlight. 31

Figure 4.6: Snapshot of a breaker detected in co-located visible and IR imagery, taken during SoCal 2010 experiment, 2010/12/06 22:02:32.75 [UTC]. **(a)** IR image temperature with 20-minute mean removed. Black arrows indicate breaking front velocities [m/s] (scale given in image), Green dashed line indicates the boundary of the cutout in the visible image (white area in (b)). **(b)** Visible (black and white) image. Blue arrows indicate breaking front velocities detected in visible imagery, orange arrows indicate velocities detected in IR. The white area in the lower left was removed from analysis as it contained a subsurface instrument which was visible through the clear ocean water and thus affected breaker detection in visible imagery. Wide field of view versions of these images are shown in figure 4.7 and 4.8. 33

Figure 4.7: Snapshot of a breaker detected in IR imagery, taken during SoCal 2010 experiment, 2010/12/06 22:02:32.75 [UTC]. Wide field of view version of Figure 4.6 **(a)**; IR image temperature with 20-minute mean removed. Black arrows indicate breaker front velocities [m/s] (scale given in image), Green dashed line indicates the boundary of the cutout in the visible image. The blurry line, approximately 0.1 m wide, that extends from approximately (17.2,13.6) to (19.2,14.8) was the location of a cable that supported underwater instrumentation. The cable was removed from imagery and the resulting gap interpolated over. . 34

Figure 4.8: Snapshot of a breaker detected in visible imagery, taken during SoCal 2010 experiment, 2010/12/06 22:02:32.75 [UTC]. Wide field of view version of Figure 4.6 **(b)**; visible (black and white) image. Blue arrows indicate breaker front velocities detected in visible imagery, orange arrows indicate velocities detected in IR. The orange dashed line shows the boundary of the IR image. The white area in the lower left was removed from analysis as it contained a subsurface instrument which was visible through the clear ocean water and thus affected breaker detection in visible imagery. 35

Figure 4.9: Comparison of $\Lambda(c)$ measured using visible and IR video. Color corresponds to wave age. **(a)** Shows distributions from concurrent, co-located IR video (solid lines) and visible video (dashed lines) taken during the SoCal 2010 experiment. **(b)** Shows $\Lambda(c)$ measured during the RaDyO 2009 experiment using stereo IR (colored lines) compared with $\Lambda(c)$ measured during the same experiment by *Zappa et al.* (2012) using visible imagery (colored circles). The solid black line is the c^{-6} dependence predicted by *Phillips* (1985) as shown in *Zappa et al.* (2012). 37

Figure 4.10: Nondimensional breaking length distribution. Distributions have been binned by wave age with corresponding colors. Solid lines are measurements taken in this work using stereo IR imagery, dash-dot lines are from visible imagery in this work, and dashed lines are from the airborne measurements of *Kleiss and Melville* (2010). Scaling uses ballistic velocity, steepness, and wave age dependence from Equation 4.13. 39

Figure 4.11: **(a)** Dissipation by breaking (ordinate) compared with modelled wave field dissipation (abscissa). **(b)** Momentum flux from waves to currents due to wave breaking (ordinate) plotted against wind stress (abscissa). Color corresponds to wave age and solid line indicates 1:1 correspondence. 42

Figure 4.12: Moments of $\Lambda(c)$: a) zeroth, b) first, c) fourth, and d) fifth. Colored lines are data from this work, binned by wave age. Data from the literature is the same as in figure 4.1; thick black lines are from the laboratory measurements of *Jessup and Phadnis* (2005). Field measurements are from: *Melville and Matusov* (2002) lines with small dots, *Gemmrich et al.* (2008) lines with squares, and *Kleiss and Melville* (2010) solid gray lines. The thin black lines are c^{-6}. 44
Figure 4.13: Dissipation and stress calculated using only $c > 2$ m/s for comparison with figure 4.11. This represents only air-entraining breakers and removes the effect of microbreaking. **(a)** Dissipation by breaking (ordinate) compared with modelled wave field dissipation (abscissa). **(b)** Momentum flux from waves to currents due to wave breaking (ordinate) plotted against wind stress (abscissa). Color corresponds to wave age and solid line indicates 1:1 correspondence. 45
Figure 4.14: Effects of including microbreaking in the integration of a) $\Lambda(c)$, and b) the first moment of $\Lambda(c)$. The ordinate uses $c = 2$ m/s as the lower limit of integration whereas the abscissa uses the full range of c. Each point corresponds to a 20-minute average, and the coloring represents wave age. 46

Figure 5.1: Schematic of uneven points used in vorticity calculation. . . . 53
Figure 5.2: 20-minute average spectra of vertical vorticity taken during RaDyO 2009. *Left:* Directional wavenumber spectra, $S_{\omega_3\omega_3}(k_x, k_y)$. White arrows indicate mean wind direction and gray arrows indicate direction of wind-wave spectral peak. *Right:* Average measured 1D directional spectra (dashed black lines), theoretical spectra including resolution roll-off, $S_{MOD}(\epsilon; k_1)$ (solid dark gray lines), and $S_{MOD}(\epsilon; k_1)$ in fitted range (solid light gray lines). 55
Figure 5.3: Comparison of vorticity spectra using different methods for calculating vorticity. Spectra are 20-minute averages and are of a) surface-normal vorticity from the circulation technique b) vertical component of surface-normal vorticity c) the technique of *Meyer et al.* (2001). The corresponding 1D vorticity spectra are shown in figure 5.4. The sampling period started at 2009/09/08 03:00 [UTC]. 56

Figure 5.4: Comparison of 1D vorticity spectra using different methods for calculating vorticity in logarithmic (top) and linear (bottom) coordinates. Spectra are 20-minute averages for the period starting at 2009/09/08 03:00 [UTC]. Black curves are from the technique of *Meyer et al.* (2001), red curves are surface-normal vorticity from the circulation technique, blue curves are the vertical component of surface-normal vorticity. Solid lines are spectra in the east direction and dashed are north. The corresponding 2D spectra are shown in figure 5.3. 57
Figure 5.5: Theoretical vorticity spectra for 3D (—) and 2D (− −) isotropic turbulence with an energy spectrum of the form given in Equation 5.18. Shading indicates dissipation in units of $[m^2s^{-3}]$. . . . 60
Figure 5.6: Comparison of techniques for calculating dissipation, ϵ, at the surface. Each symbol corresponds to a 20-minute average. The abscissa is dissipation calculated using the vorticity spectral fit method. Red and green symbols are for the values on the ordinate calculated using Equations 5.14 and 5.15 respectively (using the rotational velocity component). Blue symbols are for the values calculated using the inertial (large eddy) method. Triangles are data collected during RaDyO 2009, and circles are data from the SoCal 2010 experiment. 63
Figure 5.7: Near-surface TKE dissipation. Data in green are from the stereo IR PIV measurements. a) shows dissipation measured using the vertical beam of the near-surface Aquadopp, averaged between 12 and 45 cm from the instantaneous surface (black) and between 45 and 72 cm from the surface (gray). b) shows dissipation measured using the horizontal beams in the up-wave (red) and across-wave (blue) directions. The mean depth of the horizontal beams was 1.05 m and the section of each horizontal beam used for dissipation calculation was a distance of 0.5 m to 1.2 m from the instrument head. 68
Figure 5.8: Subsurface dissipation measured by LTMI array over 20-minutes starting 2010/12/06 23:00 [UTC], compared against a wall layer (dash-dot line). Triangles are measurements from the horizontal beams of the LTMIs; upward triangles are from the up-current beam (beam 2), downward triangles are from the cross-current beam (beam 3). Colors correspond to LTMI number; 1, blue; 2, green; 3 red. Small triangles correspond to (overlapping) 2.5 s averages. All depths are relative to the instantaneous surface. . 69

Figure 5.9: Plan view of FLIP and subsurface profilers for the 20-minute period starting 2010/12/06 23:00 [UTC]. Scale is meters for spatial measurements, m/s for wind velocity, and cm/s for current velocities. The gray region is the superstructure and booms, the black circle (half obscured) is the sub-surface hull of FLIP. The thick red arrow is the wind direction, thin arrows are current directions. Ellipses, centered at those arrow tips, indicate the standard deviation of velocity at profiler (again, in cm/s). Color corresponds to LTMI, blue is the near-surface fixed depth LTMI, green is the upper of the two profiling LTMIs, and orange is the lower profiling LTMI. The dashed lines outline wedges of potential wake from FLIP's hull. 71

Figure 5.10: Measured subsurface dissipation profiles during SoCal 2010. Each triangle represents a 20-minute average in dissipation and depth. The line with dots are from the upward-looking beam of the near-surface LTMI and are relative to the instantaneous surface. The solid lines at the top of the plot are the simultaneous surface dissipation values measured using the stereo IR PIV system. Hollow triangles are data periods thought to be affected by the noise floor of the instrument. Color corresponds to wave age. 72

Figure 5.11: Measured subsurface dissipation profiles from the Aquadopp float during RaDyO 2009. Lines with dots are from the upward-looking beam and are relative to the instantaneous surface. Dashed lines are the wall layer, $\epsilon_{wl} = u_{*w}^3/\kappa z$. Diamonds are measured surface dissipation from the stereo IR. The dissipation values below the dash-dot line at $z = -0.55$ m are thought to be elevated due to the wake of the instrument. 73

Figure 5.12: Dependence of surface dissipation on band averaged dissipation, B_b. Data from *Gemmrich* (2010) are 40-minute averages of dissipation within 10 cm of the free surface. They are separated into measurements taken beneath wave crests (black up triangles) and wave troughs (gray down triangles). Stereo IR PIV measurements are 20-minute averages, colored by wave age. Triangles are from RaDyO 2009 and circles are from SoCal 2010. 75

Figure 5.13: Subsurface TKE dissipation scaled by energy input, F, and significant wave height, H_s, as in T96. All data from this work used $F = F_{dsJ}$, whereas the data from T96 and D96 used $F = F_{TD}$ (see appendix D). Color corresponds to wave age and each line or symbol represents a 20-minute average. The dashed lines are the wall layer scaling, $\epsilon_{wl} = u_{*w}^3/\kappa z$. Solid lines are the surface IR measurements extended downwards using an exponential curve with an e-folding scale of $0.075H_s$. From SoCal 2010, lines with dots are from the vertical beam of the near-surface Aquadopp, circles are from the LTMI horizontal beams (with data shown in figure 5.11 but thought to be noise removed), and lines with squares are from the Aquadopp float. From RaDyO 2009, up-triangles are from the LTMI, and lines with left-triangles are from the Aquadopp float. The black symbols are the data of T96 ($\circ$) and D96 ($+$ and $*$); the thick black line indicates the best fit given by D96, $\epsilon H_s F = 0.3(z/H_s)^{-2}$, including their expected constant near-surface dissipation layer. 77

Figure 5.14: Sub-surface profiles measured by *Gemmrich* (2010). Grey triangles are from wave troughs, black triangles are from wave crests, and red curves are our fits to their wave crest data. These fits are used in figure 5.16 to include *Gemmrich* (2010) in the scaled plot. The reference velocity used was, $u_{ref} = 1.58u_*$ for the high-wind case (a), and $u_{ref} = 2.7u_*$ for the low-wind case (b). 78

Figure 5.15: Subsurface TKE dissipation measured during the SoCal 2010 experiment. Data have been bin-averaged in wave age (coloring) and scaled by wall layer values. Note the trend towards increased ϵ/ϵ_{wall} with increased wave age. 80

Figure 5.16: Subsurface TKE dissipation scaled by energy input, F, and significant wave height, H_s, as in T96. All data from this work used $F = F_{dsJ}$, whereas the data from T96 and D96 used $F = F_{TD}$ (see appendix D). Color corresponds to wave age and each line or symbol represents a 20-minute average. The heavy dashed lines are scaled fits to the data of *Gemmrich* (2010) as in figure 5.14. Solid lines are the surface IR measurements extended downwards using an exponential curve with an e-folding scale of $0.075H_s$. From SoCal 2010, lines with dots are from the vertical beam of the near-surface Aquadopp, circles are from the LTMI horizontal beams (with data shown in figure 5.11 but thought to be noise removed), and lines with squares are from the Aquadopp float. From RaDyO 2009, up-triangles are from the LTMI, and lines with left-triangles are from the Aquadopp float. The black symbols are the data of T96 ($\circ$) and D96 ($+$ and $*$); the thick black line indicates the best fit given by D96, $\epsilon H_s F = 0.3(z/H_s)^{-2}$, including their expected constant near-surface dissipation layer. 81

Figure 5.17: Integrated water column dissipation from SoCal 2010 compared with energy input from (a) modeled wave-field dissipation, F_{dsJ}, and (b) wind-stress scaling, $\rho_w u_{*w}^2 c_p$. Circles are total integrated dissipation, up-triangles are the integrated near-surface exponential decay, and down-triangles are the integral of the sub-surface data, assuming a layer of constant dissipation from the uppermost measurement to the surface. Coloring is by wave age. 83

Figure 5.18: Coherence of surface displacement and dissipation. Top: frequency spectra of surface displacement η [m] and dissipation ϵ [m^2/s^3]. Centre: Phase of wave-dissipation coherence. Angles are defined such that at 90°, the dissipation lags the wave peak by 90°. Bottom: Magnitude squared coherence between dissipation and displacement. The pink highlighted region is the frequency band to which the wave signal was filtered for computation of the wave-phase average dissipation shown in Figure 5.20. Data are from RaDyO 2009, and represent the 20-minute period starting 2009/09/08 04:00 [UTC]. 88

Figure 5.19: Histograms of phase (left) and ratio of dissipation at the coherence peak vs coherence trough (right) for the RaDyO 2009 experiment. 89

Figure 5.20: Wave phase averaged dissipation corresponding to waves with periods between 2 s and 4 s. The wave peak is at $\theta = 0$, and the wave is propagating to the left. Data are from RaDyO 2009, and represent the 20-minute period starting 2009/09/08 04:00 [UTC]. 89

Figure 5.21: Increased dissipation from large breaking wave. Top panels show IR images of the sea surface separated by 0.25s. Temperature anomaly scale is from -0.4°C (blue) to 0.4°C (red). Below, timeseries of dissipation (a) and surface elevation (b) as the breaker passes through the IR camera field of view. The shaded area is the duration during which the breaking front was in the field of view. The surface elevation is that of a 10 cm×10 cm patch in the center of the image. The time axis is seconds since 2010/12/06 22:00 [UTC], during the SoCal 2010 experiment. . 90

Figure D.1: Comparison of energy flux using three different energy input formulations. Fewer F_{TD} data are visible as that formulation frequently produced negative energy fluxes at low wave ages. . 109

ACKNOWLEDGEMENTS

Firstly, I would like to thank my adviser, Ken Melville, for his guidance and support. He provided the scientific insight, intellectual stimulation, and enthusiasm that helped me develop as a scientist. He also provided the truly unique field opportunities that made these experiments a success.

I would like to thank my committee, Jerry Smith, Sutanu Sarker, Dan Rudnick, and Walter Munk, for their useful advice and stimulating discussions over the years.

These measurements would not have been possible without the exceptional engineering and field support of Luc Lenain and Nick Statom, for which I am very grateful.

I owe a great debt to Tom Golfinos and the crew of *R/P FLIP*. They were always willing to do whatever they possibly could to help make the experiments a success. And they made it fun to be "out there!"

Thanks to Fabrice Veron and Zachary VanKirk for providing the final stereo matching algorithm and for many useful discussions, Leonel Romero for providing Matlab code for calculating modeled wind inputs and breaking parameters, Jessica Kleiss for providing airborne $\Lambda(c)$ measurements from GOTEX, Laurent Grare for processing the meteorological data for the HiRes 2010 experiment, and the rest of the Air-Sea Interaction lab for all the help along the way.

This research was conducted under grants to WKM from the Office of Naval Research (HiRes and RaDyO DRIs) and the National Science Foundation (Physical Oceanography).

Much of the material in chapter 4 has been published in Sutherland, P. and Melville, W. K. (2013), Field measurements and scaling of ocean surface wave-breaking statistics, *Geophysical Research Letters*, **40**, grl.50584. Supplementary material from that paper has been integrated into the text and additional figures/text have been added. The dissertation author was the primary investigator and author of that paper.

Chapter 5, in part, is currently being prepared for submission for publication. Sutherland, P. and Melville, W. K., Near surface turbulence associated with

breaking waves. The dissertation author was the primary investigator and author of this paper.

VITA

2004	B.Sc. Physics, Minor Mathematics, University of Victoria
2007	M.S. Oceanography, Scripps Institution of Oceanography, University of California, San Diego
2006–2013	Graduate Student Researcher Scripps Institution of Oceanography University of California, San Diego
2013	Ph.D. Oceanography, Scripps Institution of Oceanography, University of California, San Diego

PUBLICATIONS

Sutherland, P. and Melville, W. K. (2013), Field measurements and scaling of ocean surface wave-breaking statistics, *Geophysical Research Letters*, **40**, grl.50584

FIELDS OF STUDY

Major Field: Physical Oceanography

Studies in Applied Mathematics
Professors G. R. Ierley and W. R. Young

Studies in Fluid Dynamics and Turbulence
Professors C. D. Winant, R. Salmon, and S. Sarkar

Studies in Geophysical Fluid Dynamics
Professors P. Cessi and R. Salmon

Studies in Computer Vision
Professor S. J. Belongie

Studies in Linear and Nonlinear Waves
Professors W. K. Melville, M. C. Hendershott, and R. T. Guza

Studies in Data Analysis
Professors M. Buckingham, D. L. Rudnick, S. T. Gille, R. L. Parker, C. G. Constable, and D. C. Agnew

Studies in Physical Oceanography
Professors L. D. Talley, M. C. Hendershott, and D. Roemmich

ABSTRACT OF THE DISSERTATION

On breaking waves and turbulence at the air-sea interface

by

Peter Sutherland

Doctor of Philosophy in Oceanography

University of California, San Diego, 2013

W. Kendall Melville, Chair

Wave fields in the open ocean evolve according to the radiative transfer equation of wave energy or action, which has three source terms, wind input, nonlinear wave-wave interactions, and dissipation. Of these, dissipation is thought to be the least well understood, but is expected to be dominated by wave breaking. This dissertation is an investigation of the physical processes associated with the wave breaking and dissipation.

Data were taken during three field experiments on *R/P FLIP*. These experiments took place in September 2009 south of Hawaii (Radiance in a Dynamic Ocean experiment), off the coast of Northern California in June of 2010 (High Resolution Air-Sea Interaction experiment, HIRES), and in the Southern California

bight in December 2010 (an extension of HIRES). Between the three campaigns, winds of 0 to 18 m/s and significant wave heights of 0.5 to 5 m were experienced.

Stereo Long Wave Infra Red (LWIR) video cameras mounted on one of FLIP's booms were used to reconstruct the 3D structure of an approximately 3×4 m patch of sea surface. Using surface temperature structure as a passive tracer, pattern imaging velocimetry (PIV) was applied to consecutive video frames to extract the velocity field of this patch.

An important statistic of breakers is $\Lambda(\boldsymbol{c})$, the distribution of crest length per unit area of sea surface as a function of breaker velocity $\boldsymbol{c}$. A new technique, based on image texture, was developed to track breaking waves on the stereo IR reconstructed surface. These waves ranged from large air-entraining breakers to micro breakers that would be undetectable in visible imagery. This allowed measurements of $\Lambda(\boldsymbol{c})$ that also cover the high-wavenumber gravity wave spectrum. Stress (or wave momentum flux) and dissipation can be related to the fourth and fifth moments of $\Lambda(\boldsymbol{c})$, and comparisons of these moments with wind stress and wave field dissipation showed that micro-breaking without air entrainment is dynamically significant.

A new technique was developed, whereby irrotational surface waves can be separated from rotational turbulence using a Helmholtz decomposition. Turbulent kinetic energy (TKE) dissipation at the sea surface was then estimated using this rotational velocity field. Synchronized subsurface velocity measurements from an array of profiling pulse-coherent acoustic Doppler profilers allowed the calculation of the dissipation profile to depths $\mathcal{O}(10)$ significant wave heights. Tying surface and subsurface measurements together allows estimation of total TKE dissipation in the surface wave zone of the marine boundary layer. Turbulence measurements were supported by wind and wave data, allowing us to measure the wave coherence of TKE dissipation and relate it to wind and wave conditions, especially wave breaking.

Chapter 1

Introduction

When wind flows over the sea, it creates surface waves. Energy, momentum, and mass fluxes between the atmosphere and ocean are all modulated by the wave field (*Melville* 1996). Although some of the energy and momentum input by the wind is propagated away from the input region by swell, the majority is injected locally. This results in an energetic turbulent marine boundary layer near the ocean surface, where energy is dissipated by turbulence. This dissertation consists of a suite of experiments designed to better understand the effect of surface wave breaking on the wave field and on this wave zone in the marine boundary layer, or upper mixed layer.

Ocean wave conditions have significant impacts on human enterprise. High sea states can slow or devastate commercial vessel traffic and disrupt naval operations. Accounting for the wave climate adds expense to the designs of ships and offshore platforms. Even recreational users of the ocean are affected; with surfers constantly waiting for large swells, and small craft remaining in port when waves are high. Less obvious, but potentially more important, is the effect of waves on the earth's climate. Because of their important influence on energy, momentum, heat and mass fluxes, a good understanding of the surface wave field is important for improving numerical simulations of processes dependent on those fluxes. Indeed, the modeling of heat, gas, and momentum transfer between the atmosphere and ocean has been identified as a critical area of climate research (*IPCC* 2007).

In deep water, the 2-D directional energy spectrum, $F(\boldsymbol{k})$, of a surface wave

field evolves according to the radiative transfer equation

$$\left\{ \frac{\partial}{\partial t} + (\boldsymbol{C_g} + \boldsymbol{U_0}) \cdot \boldsymbol{\nabla_H} \right\} F(\boldsymbol{k}) = S_{in} + S_{nl} + S_{ds}, \tag{1.1}$$

where $\boldsymbol{\nabla_H}$ is the divergence in horizontal directions, $\boldsymbol{C_g}$ is the intrinsic group velocity, and $\boldsymbol{U_0}$ is the constant mean current velocity. The wave spectrum is defined such that $\langle \eta^2 \rangle = \int F(\boldsymbol{k}) d\boldsymbol{k}$, where η is the surface elevation. The source terms on the right side of Equation 1.1 are energy input from the wind S_{in}, energy transfer between wavenumbers via non-linear interactions S_{nl}, and energy dissipation S_{ds}. Of these terms, only S_{nl} is thought to be fairly well understood (*Hasselmann* 1962). The dissipation term S_{ds}, through which energy is passed from the wave field into the ocean below is thought to be the least understood term (*WISE et al.* 2007). It contains a small contribution from viscous dissipation, but is surely dominated by wave breaking.

Surface waves are non-linear phenomena which span a range of spatial scales from $\mathcal{O}$(1mm) (capillary waves) to $\mathcal{O}$(10km) (groups of swell). Unfortunately, directly solving the Navier-Stokes equations over a domain large enough to contain all important features, at sufficient resolution to capture small scale physics is far beyond current (or near future) computational capabilities. Compounding this complexity is the inherent difficulty of making measurements at the air-sea interface. Not only are the processes being measured highly intermittent and nonlinear, forces on instruments are large and potentially destructive.

Recent advances in instrumentation and more powerful computer models are allowing progress in air-sea interaction research. By nesting instruments, it is possible to cover nearly the entire range of important scales. Similarly, more powerful Large Eddy Simulations (LES) are improving our ability to model important physical processes.

During the course of this research, several field campaigns were undertaken aboard R/P FLIP over a wide range of wind and wave conditions. The primary instrumentation for the work presented in this dissertation was a stereo pair of long wave infrared (LWIR) video cameras. Using these cameras, a stereo thermal imaging pattern imaging velocimetry (stereo IR PIV) technique was developed which allowed the 3D reconstruction of the sea surface shape and velocity. An algorithm

was developed to track surface breaking waves on that reconstructed surface. An array of instruments for measuring sub-surface turbulence was deployed beneath the field of view of the cameras to allow comparison of surface breakers and sub-surface turbulence. Supporting atmospheric measurements were made with a 3D sonic anemometer eddy flux system mounted directly over the IR cameras' field of view.

In addition to being the first to measure the 3D velocity of the sea surface using stereo IR cameras, two major advances were made in this work. First, a technique was developed for measuring turbulent kinetic energy (TKE) dissipation at the sea surface in the presence of surface waves. By separating the velocity field into rotational and irrotational components, it was possible to remove the irrotational wave velocity field and study only the rotational velocities thought to be dominated by turbulence. Second, an algorithm was developed to detect micro-breakers in the IR imagery. Micro-breakers are small breaking waves that do not entrain air and are thus effectively invisible to visible video measurements. It was then possible to include dynamically important micro-breaking in measurements of breaking statistics.

This dissertation has been separated into six chapters, including this introduction. The second chapter describes the experiments, covering instrument set-up and environmental conditions. The third describes the stereo IR PIV processing technique. The fourth chapter describes measurements of breaking statistics. The importance of microscale breaking for energy and momentum budgets is highlighted, and a nondimensional form of the breaker crest length distribution is proposed. The fifth chapter is a discussion of near-surface turbulent kinetic energy (TKE) dissipation. It describes the technique for measuring dissipation at the surface using stereo IR PIV as well as the sub-surface measurements. Results are compared with the literature, and the significance of findings are discussed. Finally, the sixth chapter contains a summary of the important results.

Chapter 2

Experiments

The data described here were collected during three deployments of *R/P FLIP* in the Pacific Ocean in 2009 and 2010. *R/P FLIP* was chosen as a platform because of its stability (*Smith and Rieder* 1997) and small waterplane - which minimizes reflection and shadowing of the wave field. Further, *R/P FLIP* also has a small superstructure for minimal air flow distortion and long booms to hold instruments well away from the flow-distorted regions (*Mollo-Christensen* 1968).

2.1 Experimental setup

Each of the three experiments differed slightly in the instruments deployed and their configuration. Figure 2.1 shows a schematic of the instrument setup during the SoCal 2010 experiment. The RaDyO 2009 instrument suite was similar, but installed on the port boom (instead of the starboard shown).

The primary instrumentation was a pair of FLIR SC6000 Long-Wave infrared (8 - 9.2 μm) video cameras. The cameras were mounted 3 m apart on a horizontal spar at the end of one of *FLIP*'s booms. The cameras were angled slightly towards each other so that they shared the same field of view on the sea surface, and angled 20° from vertical away from *FLIP* in order to reduce reflections from *FLIP*'s superstructure and booms. The co-located field of view was approximately 4×3 m and the image size of 640×512 pixels resulted in a nominal resolution of approximately 6 mm (which changed depending on the instantaneous

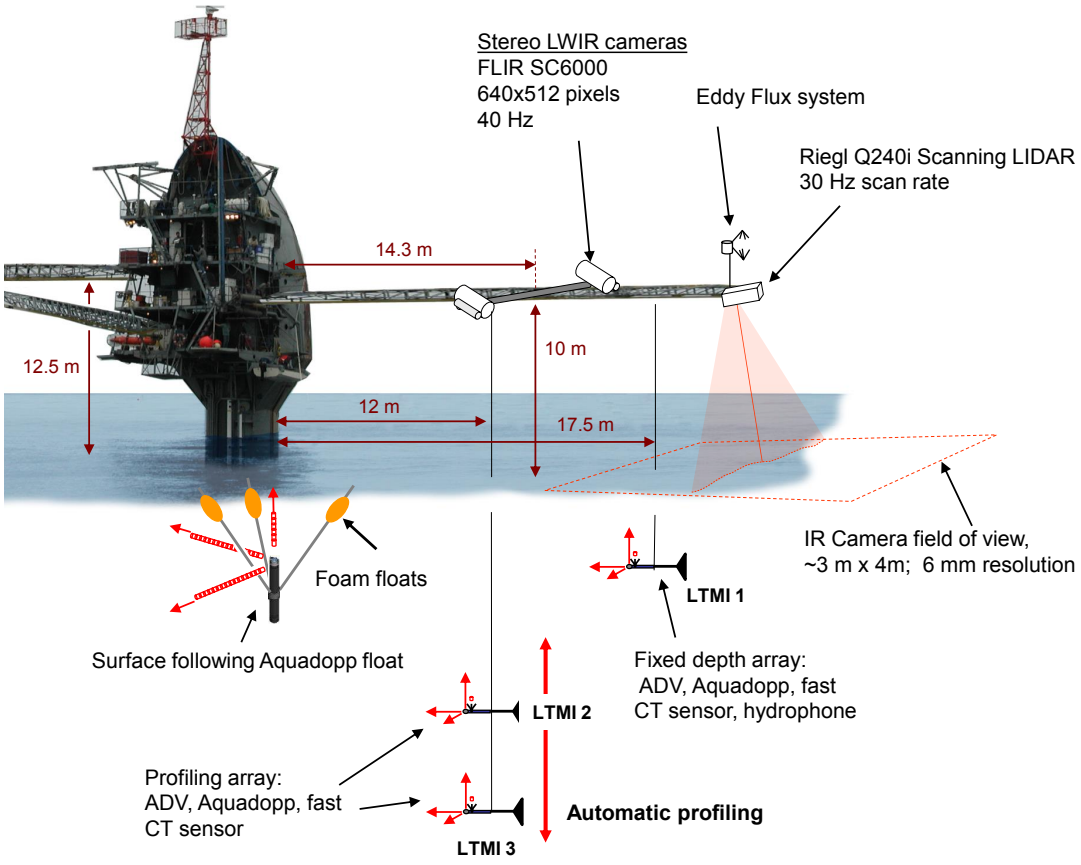

Figure 2.1: Schematic of the instrument configuration aboard R/P FLIP during the SoCal 2010 experiment. The configuration during the RaDyO 2009 experiment was similar, but instruments were mounted on the opposite (port) boom.

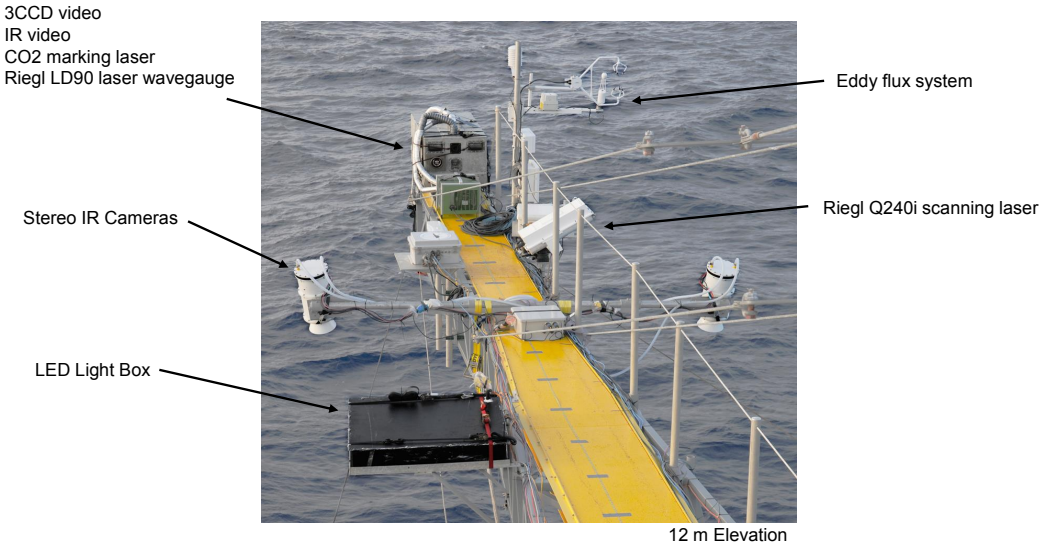

Figure 2.2: Photo looking outwards along FLIP's port boom during the RaDyO 2009 experiment.

boom and surface displacement). IR video was captured at 40 Hz (sub-sampled at 20 Hz) for the first 20 minutes of every hour.

In all three experiments, a Campbell Scientific eddy flux system (CSAT3 3-D sonic anemometer) was mounted directly over the IR cameras' field of view. These data were processed to retrieve Reynolds stresses, wind speed, and wind direction, over 30-minute average periods.

Figure 2.2 shows the mounting of the stereo IR cameras and the eddyflux system during the RaDyO 2009 experiment (on the port boom). Also shown is some additional instrumentation. The silver box at the end of the boom that contains a combination visible camera, IR camera, CO_2 marking laser, and laser wave gauge is the system described by *Veron et al.* (2008). The Riegl Q240i scanning laser wave gauge allowed computation of surface wavenumber spectra, and the LED light box was used to study the propagation of light through the wavy surface.

Subsurface turbulence was measured with an array of lowered turbulence measurements instruments (LTMIs). Each LTMI consisted of a pulse coherent acoustic doppler profiler (Nortek Aquadopp HR Profiler), an acoustic

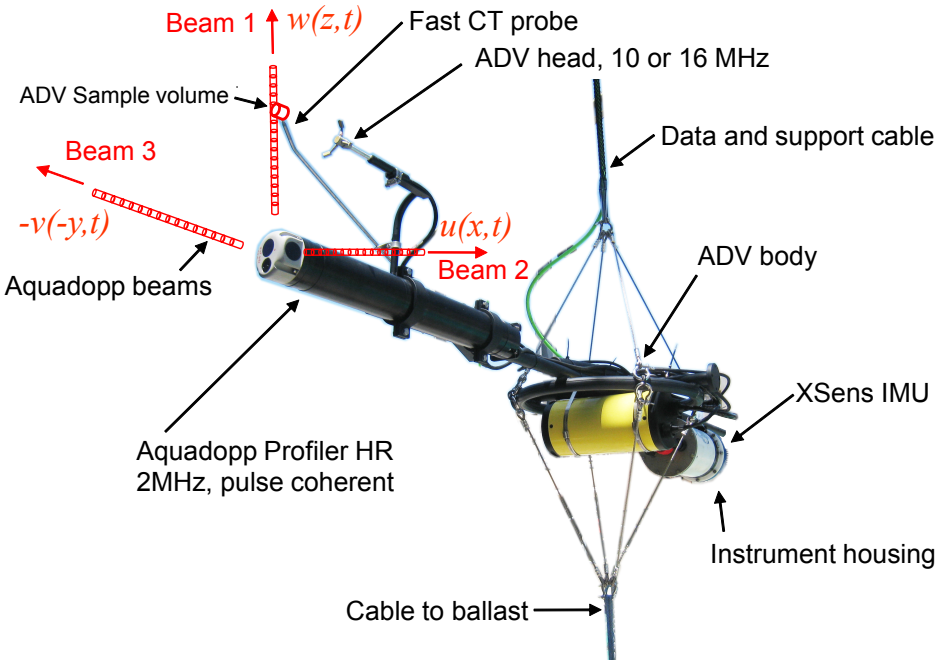

Figure 2.3: Subsurface lowered turbulence measurement device (LTMI). Not shown is a vane designed to keep the body of the Aquadopp orthogonal to the mean flow, with beam 2 pointing up-stream.

doppler velocimeter (Nortek Vectrino, Sontek MicroADV, or Nortek Vector), a fast conductivity-temperature probe (PME 9028), and inertial motion unit (XSens MTi). Figure 2.3 shows one of the profilers, demonstrating the relative configuration of the instrumentation.

Note that the sampling volume of the ADV is co-located with beam 1 of the Aquadopp. This allowed the use of the ADV for elimination of velocity ambiguities in the Aquadopp data. Up to three of these turbulence profilers were deployed, with one at a fixed depth and two profiling. An additional Aquadopp was mounted pointing upwards on a surface-following float (shown in Figure 2.1).

2.2 Field sites

Three experimental locations were chosen to provide a wide range of experimental conditions; the trade wind dominated region south of Hawaii, the strong

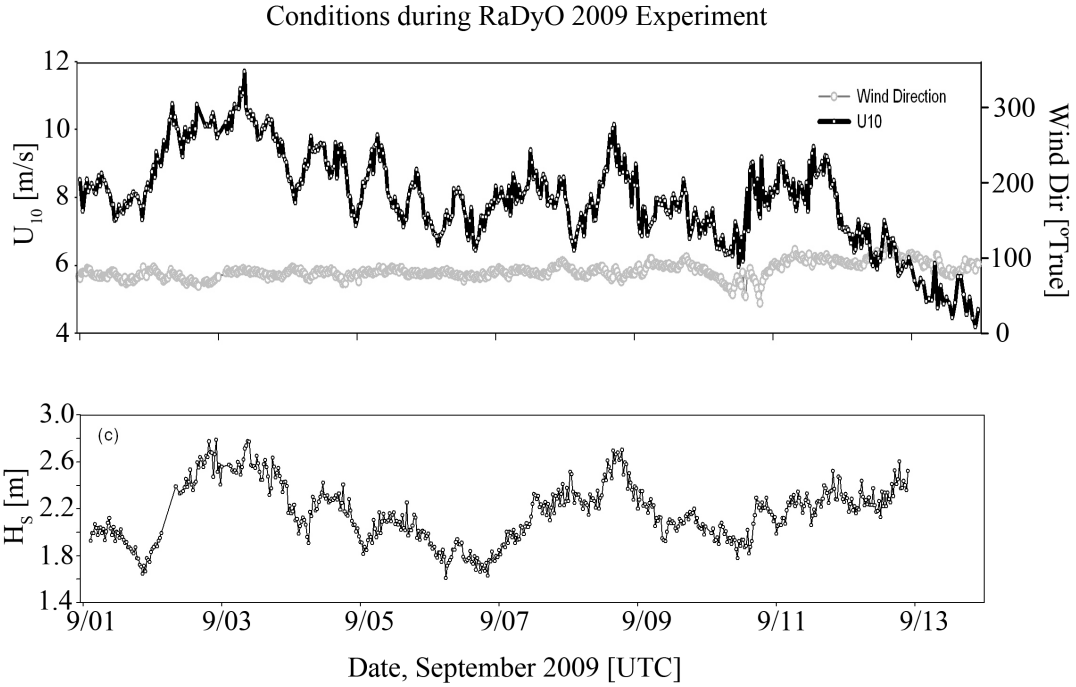

Figure 2.4: 20-minute average wind and wave conditions during RaDyO 2009 experiment. The top panel shows wind speeds, U_{10}, as black circles connected by a black line, and wind directions as gray circles. The bottom panel shows significant wave height, H_s.

alongshore winds off Northern California, and the relatively mild conditions in the Southern California Bight. A summary of conditions has been included in tables 2.1 and 2.2.

The first experiment, Radiance in a Dynamic Ocean 2009, RaDyO 2009, (*Dickey et al.* 2012), was a 12-day deployment that started 120 km south of the Island of Hawai'i with *FLIP* drifting west at approximately 35 cm/s (0.7 knots) for approximately 330 km in trade winds. Conditions were typical trades (see Figure 2.4) with 10-minute average 10 m winds, U_{10}, ranging between 4 and 12 m/s from the east and significant wave heights, H_s, between 1.5 and 2.5 m.

The ONR-sponsored HiRes DRI consisted of two experiments: HiRes 2010 was a 14 day deployment with *FLIP* moored approximately 25 km off the coast of Northern California (38°20′N, 123°26′W) in strong north westerly winds. Wind Speeds SoCal 2010 took place over two days in the Southern California Bight in

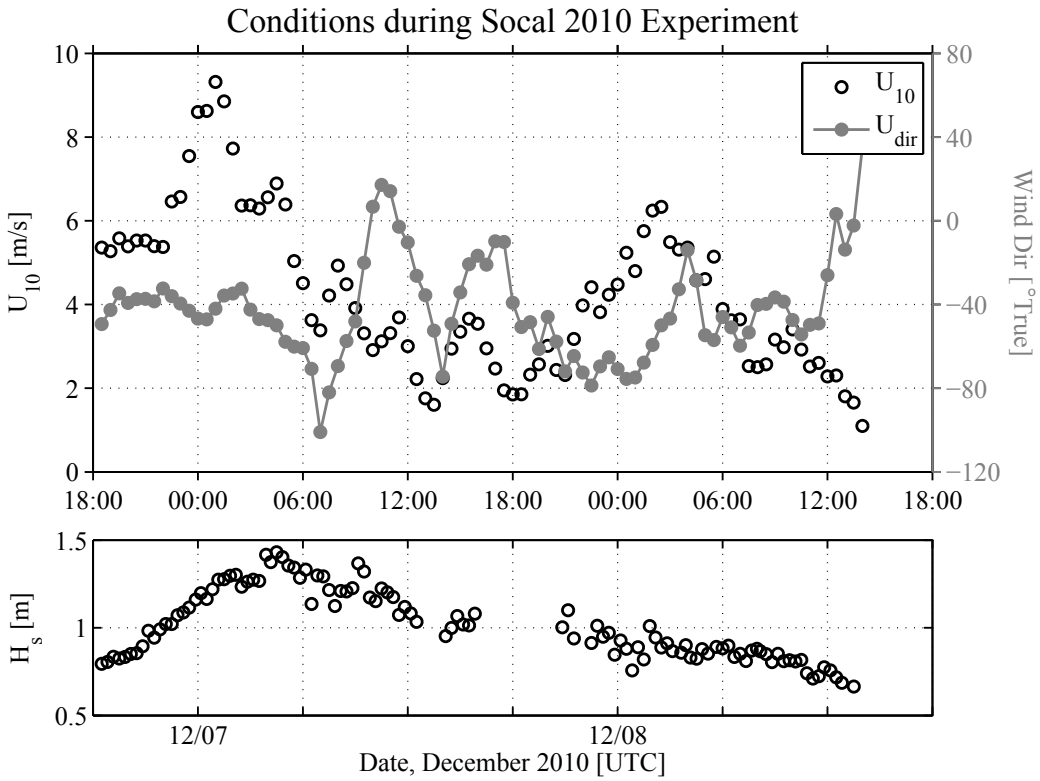

Figure 2.5: 20-minute average wind and wave conditions during Southern California 2010 experiment. The top panel shows wind speeds, U_{10}, as black circles, and wind directions as gray circles. The bottom panel shows significant wave height, H_s.

much milder conditions. Winds ranged from 1-9 m/s with significant wave heights of 0.5 to 1.5 m (see Figure 2.5).

Between the three experiments, 70 20-minute records were analyzed with U_{10} of 1.6 to 16 m/s, H_s of 0.7 to 4.7 m, and wave ages of $c_p/u_* = 16$ to 150.

Wind speed and wave age were strongly anti-correlated during these experiments, as seen in Figure 2.7. This reduces the available parameter space significantly.

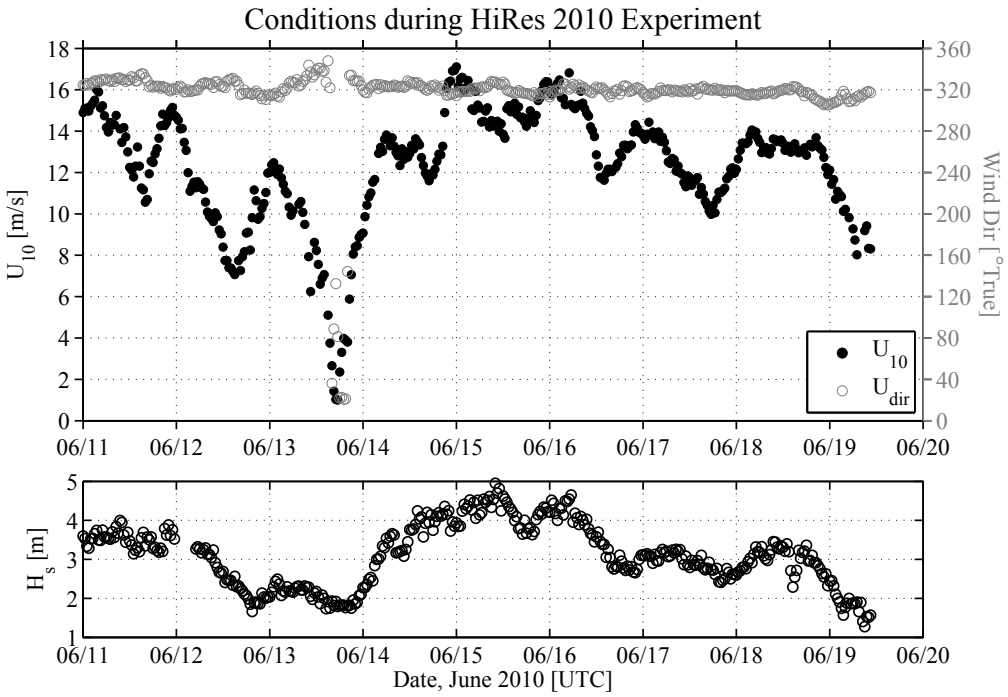

Figure 2.6: 20-minute average wind and wave conditions during the HiRes 2010 experiment. The top panel shows wind speeds, U_{10}, as black circles, and wind directions as gray circles. The bottom panel shows significant wave height, H_s.

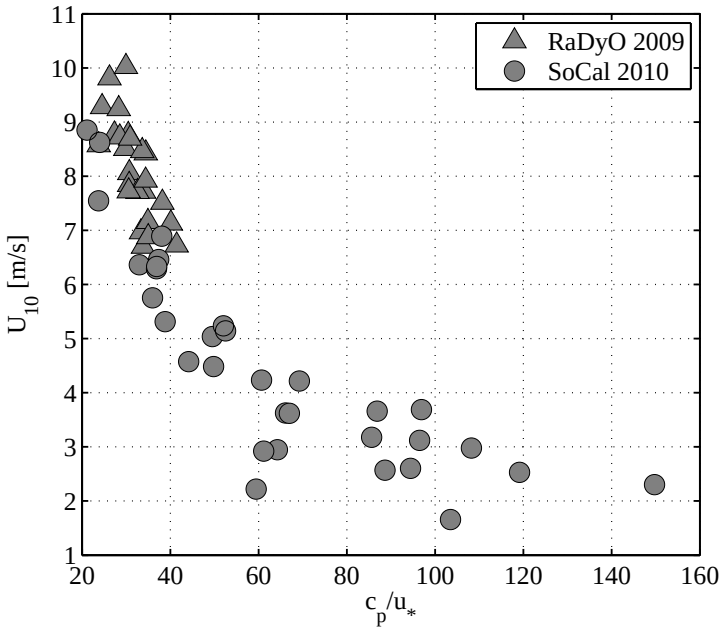

Figure 2.7: Relationship between wind speed and wave age during these experiments. Each point represents a 20-minute average. Triangles are from the RaDyO 2009 experiment, circles are from the SoCal 2010 experiment.

Table 2.1: 20-minute average conditions during RaDyO 2009 and HiRes 2010. Date format is yyyy/mm/dd HH:MM, which is the standard throughout this work.

Date/Time [UTC]	U_{10} [m/s]	Wind dir. [° true]	u_* [m/s]	H_s [m]	T_{peak} [s]	c_p/u_*	$10^4 F_{dsJ}$ [m^3/s^3]	$10^4 F_{inJ}$ [m^3/s^3]	$10^4 F_{Terray}$ [m^3/s^3]	$10^4 c_p u_{*w}^2$ [m^3/s^3]	ε_{IR} [m^2/s^3]
RaDyO 2009											
2009/09/06 05:00	6.97	77	0.266	1.68	5.63	33	2.528	0.498	-0.262	7.0402	0.0124
2009/09/07 20:00	7.72	83	0.305	2.43	6.59	34	4.945	0.810	-0.774	10.8709	0.0264
2009/09/07 21:00	8.06	83	0.316	2.31	6.15	30	5.951	1.038	-0.324	10.8272	0.0245
2009/09/07 22:00	8.51	88	0.340	2.37	6.42	29	5.348	1.194	-0.153	13.1229	0.0243
2009/09/07 23:00	8.58	89	0.415	2.42	6.26	24	7.002	2.221	-0.269	19.0642	0.0240
2009/09/08 00:00	7.84	83	0.327	2.63	6.36	30	5.678	1.002	-0.940	12.0160	0.0198
2009/09/08 01:00	7.16	80	0.280	2.52	6.21	35	6.525	0.635	-1.175	8.6005	0.0239
2009/09/08 02:00	6.70	80	0.292	2.40	6.26	33	5.529	0.770	-1.305	9.4311	0.0229
2009/09/08 03:00	6.73	74	0.246	2.40	6.45	41	4.211	0.382	-1.349	6.8522	0.0198
2009/09/08 04:00	7.13	70	0.255	2.25	6.49	40	3.699	0.449	-0.904	7.4387	0.0199
2009/09/08 05:00	7.51	76	0.280	2.41	6.79	38	5.179	0.700	-0.623	9.4146	0.0234
2009/09/08 06:00	6.88	71	0.299	2.36	6.63	35	3.894	0.726	-1.253	10.4260	0.0149
2009/09/08 07:00	7.71	69	0.307	2.29	6.34	32	4.289	0.802	-0.648	10.5634	0.0159
2009/09/08 08:00	7.72	76	0.333	2.40	6.45	30	5.046	1.112	-0.701	12.6133	0.0189
2009/09/08 11:00	7.92	79	0.299	2.36	6.52	34	4.880	0.827	-0.412	10.3015	0.0197
2009/09/08 12:00	8.43	82	0.291	2.60	6.36	34	5.484	0.684	-0.350	9.5204	0.0187
2009/09/08 13:00	8.77	76	0.334	2.64	6.45	30	6.335	1.168	-0.269	12.6707	0.0180
2009/09/08 14:00	8.78	72	0.385	2.64	6.68	27	5.608	1.633	-0.357	17.4249	0.0185
2009/09/08 15:00	9.81	72	0.412	2.76	6.86	26	6.222	2.039	0.393	20.5578	0.0284
2009/09/08 16:00	10.02	68	0.349	2.76	6.62	30	6.982	1.258	0.795	14.2086	0.0210
2009/09/08 17:00	9.28	81	0.430	2.66	6.70	24	8.242	2.573	0.023	21.8761	0.0359
2009/09/08 20:00	9.24	68	0.359	2.43	6.43	28	5.408	1.409	0.411	14.5831	0.0155
2009/09/08 21:00	8.72	74	0.340	2.43	6.15	28	6.048	1.184	-0.063	12.5245	0.0158
2009/09/08 22:00	8.47	76	0.299	2.34	6.37	33	5.619	0.851	0.215	10.0249	0.0149
2009/09/08 23:00	8.70	73	0.322	2.55	6.30	31	5.248	1.050	0.138	11.4727	0.0189
HiRes 2010											
2010/06/14 20:00	12.86	321	0.535	4.10	7.85	23	20.056	5.628	4.985	42.1571	N/A
2010/06/15 03:00	16.39	319	0.699	4.35	7.39	17	34.431	13.809	16.777	67.6022	N/A
2010/06/15 10:00	14.32	327	0.625	4.95	8.19	20	27.250	8.798	8.138	60.0510	N/A
2010/06/15 22:00	15.91	316	0.680	4.15	7.47	17	30.225	11.828	15.076	64.5931	N/A
2010/06/16 00:00	16.00	313	0.645	4.20	7.32	18	34.193	11.456	16.262	56.9860	N/A

Table 2.2: 20-minute average conditions during SoCal 2010 experiment. Date format is yyyy/mm/dd HH:MM.

Date/Time [UTC]	U_{10} [m/s]	Wind dir. [° true]	u_* [m/s]	H_s [m]	T_{peak} [s]	c_p/u_*	$10^4 F_{dsJ}$ [m^3/s^3]	$10^4 F_{inJ}$ [m^3/s^3]	$10^4 F_{Terray}$ [m^3/s^3]	$10^4 c_p u_{*w}^2$ [m^3/s^3]	ε_{IR} [m^2/s^3]
SoCal 2010											
2010/12/06 22:00	6.46	324	0.205	1.11	4.86	37	1.210	0.222	0.123	3.8114	0.0215
2010/12/06 23:00	7.54	317	0.342	1.15	5.14	23	1.470	1.068	0.265	11.1833	0.0216
2010/12/07 00:00	8.62	313	0.319	1.24	4.85	24	2.333	1.016	0.991	9.2111	0.0126
2010/12/07 01:00	8.85	324	0.382	1.35	5.12	21	3.414	1.921	1.044	13.9062	0.0309
2010/12/07 02:00	6.36	328	0.242	1.38	5.06	33	2.284	0.403	-0.195	5.5143	0.0208
2010/12/07 03:00	6.29	313	0.234	1.37	5.47	37	1.679	0.358	-0.148	5.5600	0.0162
2010/12/07 04:00	6.89	310	0.253	1.46	6.11	38	1.494	0.429	-0.105	7.2956	0.0193
2010/12/07 05:00	5.04	300	0.189	1.41	5.94	49	1.199	0.159	-0.728	3.9650	0.0110
2010/12/07 06:00	3.63	289	0.148	1.37	6.21	65	0.660	0.060	-1.052	2.5415	0.0074
2010/12/07 07:00	4.22	278	0.149	1.33	6.55	69	0.470	0.059	-0.847	2.7113	0.0081
2010/12/07 08:00	4.48	303	0.188	1.25	5.94	49	0.601	0.140	-0.700	3.9041	0.0101
2010/12/07 10:00	3.12	377	0.099	1.21	6.07	96	0.447	0.015	-0.942	1.1144	0.0050
2010/12/07 11:00	3.69	357	0.098	1.22	6.03	96	0.440	0.014	-0.804	1.0847	0.0053
2010/12/07 12:00	2.22	334	0.171	1.15	6.44	59	0.327	0.085	-0.997	3.5194	0.0065
2010/12/07 13:00	1.61	307	0.147	1.10	5.79	62	0.252	0.038	-1.047	2.3502	0.0192
2010/12/07 14:00	2.95	311	0.139	0.96	5.65	64	0.170	0.033	-0.601	2.0432	0.0177
2010/12/07 15:00	3.66	339	0.125	1.07	6.88	86	1.705	0.052	-0.583	2.0156	0.0454
2010/12/07 16:00	2.95	339	0.210	1.12	5.41	40	0.491	0.195	-0.813	4.4696	0.0188
2010/12/07 17:00	1.95	350	0.106	1.12	6.34	93	0.191	0.016	-1.012	1.3341	0.0323
2010/12/07 18:00	1.86	309	0.045	1.15	6.12	211	0.236	0.002	-1.104	0.2368	0.0236
2010/12/07 19:00	2.57	299	0.077	1.12	5.36	109	0.655	0.011	-0.903	0.5983	0.0230
2010/12/07 20:00	2.44	302	0.156	1.16	6.28	63	0.235	0.047	-0.997	2.8525	0.0126
2010/12/07 21:00	3.18	295	0.122	1.12	6.65	85	0.217	0.021	-0.831	1.8618	0.0029
2010/12/07 22:00	4.41	281	0.130	0.96	5.59	67	0.198	0.035	-0.362	1.7694	0.0097
2010/12/07 23:00	4.23	295	0.150	0.98	5.78	60	0.213	0.059	-0.440	2.4137	0.0070
2010/12/08 00:00	5.24	284	0.160	0.95	5.26	52	0.274	0.075	-0.202	2.4841	0.0120
2010/12/08 01:00	5.75	292	0.224	0.94	5.10	36	0.582	0.248	-0.134	4.7350	0.0127
2010/12/08 02:00	6.33	310	0.213	1.00	4.97	37	0.991	0.277	0.066	4.1687	0.0161
2010/12/08 03:00	5.31	327	0.187	0.93	4.61	38	0.647	0.154	-0.178	2.9941	0.0109
2010/12/08 04:00	4.58	332	0.163	0.86	4.56	44	0.596	0.087	-0.254	2.2462	0.0091
2010/12/08 05:00	5.14	303	0.144	0.90	4.78	52	0.448	0.058	-0.146	1.8256	0.0110
2010/12/08 06:00	3.62	309	0.120	0.90	5.10	66	0.314	0.029	-0.447	1.3644	0.0049
2010/12/08 07:00	2.53	307	0.067	0.85	5.04	118	0.211	0.003	-0.548	0.4169	0.0033
2010/12/08 08:00	2.57	320	0.097	0.93	5.47	88	0.182	0.011	-0.651	0.9616	0.0024
2010/12/08 09:00	2.98	321	0.078	0.89	5.38	107	0.173	0.006	-0.547	0.6143	0.0032
2010/12/08 10:00	2.92	306	0.130	0.84	5.03	61	0.158	0.030	-0.495	1.5760	0.0033
2010/12/08 11:00	2.60	311	0.079	0.74	4.76	93	0.119	0.005	-0.419	0.5581	0.0029
2010/12/08 12:00	2.30	363	0.054	0.75	5.10	148	0.242	0.004	-0.453	0.2735	0.0082
2010/12/08 13:00	1.66	358	0.081	0.68	5.32	102	0.135	0.010	-0.449	0.6527	0.0083

Chapter 3

Stereo IR PIV processing

Stereo imagery uses image pairs taken by two cameras with a known relative orientation (rotation and translation). By matching features in both images, it is then possible to triangulate their location in three dimensions (3D). Tracking features in consecutive images then allows the 3D velocity of the features to be calculated.

Over the duration of these experiments, the sea surface contained a wide variety of thermal structures. Actively breaking waves, remnants of past breakers, and the surface signatures of turbulence all produce thermal patterns on millimeter to meter and larger length scales. If the temperature differences across these features are greater than the detectable minimum of the IR camera (>25 mK), they can be imaged and used for stereo PIV.

Stereo imaging of the sea surface is not a new method (see, for example *Shemdin et al.* 1988, *Banner et al.* 1989, *Benetazzo* 2006). The use of IR imagery in the laboratory (*Hilsenstein* 2005) has shown it to be an effective way of eliminating the principal difficulties of using visible stereo on a water surface, namely water penetration and specular reflection (*Jähne et al.* 1994). The experiments described here are, to the best of our knowledge, the first use of stereo infrared imagery to reconstruct the sea surface in the field.

Stereo PIV has been used by other authors to study the velocity field at the surface boundary. For example, *Turney et al.* (2009) used two video cameras to track particles in wave tank seeded with flourescent micro spheres. In contrast, the

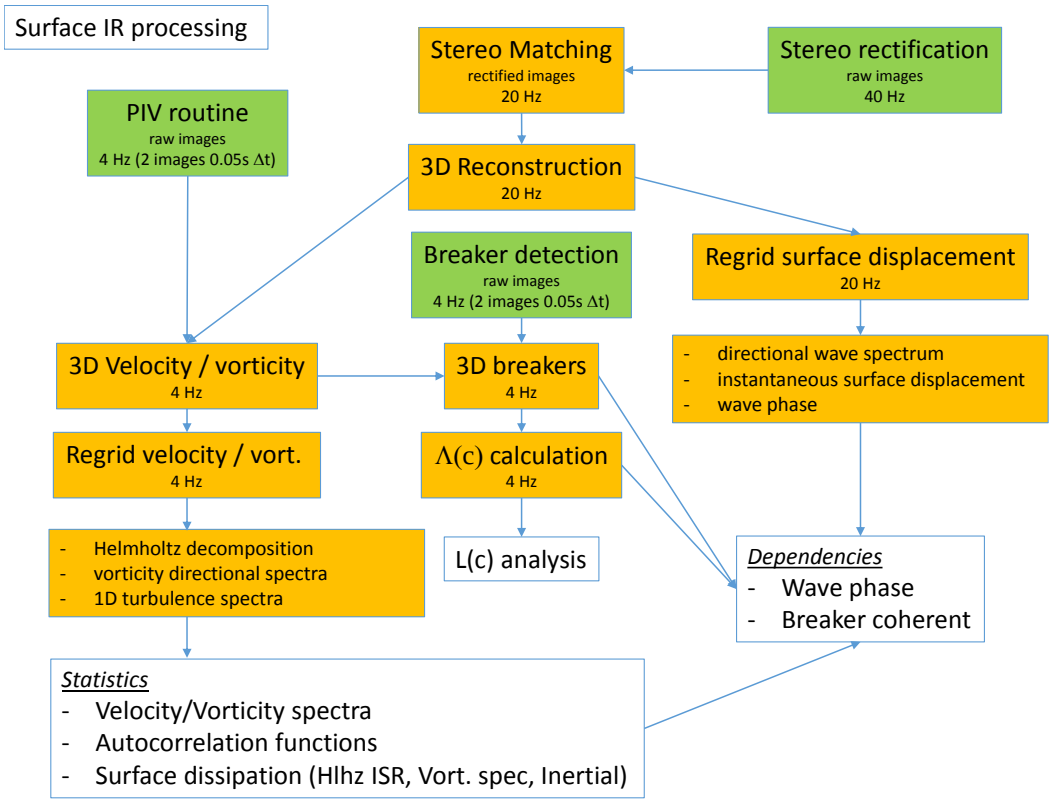

Figure 3.1: Schematic overview of stereo IR processing sequence. Green boxes indicate input of raw images (with artifacts and mean removed). Yellow boxes are processing steps. White boxes are analysis steps. Sampling rates are indicated where appropriate.

work presented here does not require seeding, instead tracking the natural thermal structures at the sea surface. Various authors, (for example, *Garbe et al.* (2003), *Veron et al.* (2008), *Rocholz et al.* (2010), and *Chickadel et al.* (2011)) have shown that by treating the surface temperature structure as a passive tracer, tracking thermal features between frames can yield a surface velocity field. These authors used a single IR camera and assumed a flat sea surface to measure velocity. To the best of our knowledge, thermal structure PIV has never been combined with stereo imaging to reconstruct the 3D velocity at the sea surface.

Figure 3.1 contains a flowchart of the data processing stages. The sequence for these data was as follows.

1. **Initial preparation.** Most images contained a data/support cable for sub-

surface instrumentation. Potential image pixels on this line were found using a Roberts edge detection algorithm. Due to the large number of non-line pixels detected, a random sample consensus (RANSAC) technique was used to fit a line to these points. A line through this fit a set width (10 pixels for RaDyO 2009 data, 20 pixels for SoCal 2010 data) was removed from the image and filled in using a linear interpolation from the surrounding pixels.

2. **Mean removal.** For each 20-minute IR video record, a mean image was calculated by averaging 500 equally spaced (in time) images, and this mean image was subtracted from each individual image to retrieve the temperature anomaly, which was used for all analysis.

3. **Calibration and image rectification.** During the RaDyO 2009 experiment, the camera setup was calibrated using a checkerboard patterned calibration card and applying *Bouguet* (2010)'s Camera Calibration Toolbox for Matlab. Due to an inability to use the checkerboard during the SoCal 2010 experiment, those images were calibrated using *Fusiello and Irsara* (2008)'s uncalibrated rectification Matlab toolbox with manually selected point matches. Epipolar rectification (*Ma et al.* 2006) was then performed on all images. This consists of a set of projective transformations that result in image pairs where epipolar lines follow horizontal scan lines. That is, any image feature will be at the same vertical pixel in the left and right image, allowing the search for stereo correspondences to be carried out in one dimension.

4. **Disparity calculation.** Stereo feature matching was applied to epipolar rectified image pairs. Disparity maps were created using a multi level normalised cross correlation matching routine developed specifically for surface wave field reconstruction by Fabrice Veron and Zachary VanKirk at the University of Delaware. Cascading windows were square with 256, 128, 64, 32, 16, and 8 pixel edges, with 50% overlap. This resulted in a final resolution of 8 pixels or approximately 5 cm. Image disparity was calculated for every second image, for a frame rate of 20 Hz.

5. **3D Triangulation.** Stereo reconstruction of the sea surface from disparity maps followed standard techniques developed for visible imagery (*Hartley*

and Zisserman 2003). 3D points were triangulated using the *Bouguet* (2010) toolbox for the RaDyO 2009 experiment and using the *Fusiello and Irsara* (2008) toolbox for the SoCal 2010 experiment. A curvature of approximately 10cm over 2m remained in the mean reconstructed surface in the SoCal 2010 experiment due to un-corrected lens distortion. To remove that curvature, a 2D parabola was fitted to each image, and those parabolas were averaged over 20 minutes of images. The 20-minute mean curvature was then removed from each image. The validity of this correction was checked by ensuring that the mean reconstructed surface was flat and that different locations on the final reconstructed water surface showed a constant variance in vertical displacement.

6. **Thermal structure PIV.** Independent of the stereo processing, pattern image velocimetry (PIV) was applied to the un-rectified images. Feature tracking was performed on images separated by 0.05 s, using a normalized cross correlation technique with cascading window sizes of 64, 32, 16, and 8 pixels. The algorithm used is a modified version of the publicly available PIV Lab software (*Thielicke and Stamhuis* 2010) and is capable of detecting sub-pixel displacements, allowing displacements for each window to be calculated theoretically to within less than 0.1 pixels (approximately 0.6 mm). The algorithm was tested on synthetic data to ensure that it could convincingly track features in the IR video data used here over a range of scales and was found to have a mean square error of approximately 1.7 pixels. This PIV processing was only applied to the camera with a higher signal to noise in each experiment. That was the left camera during RaDyO 2009 and SoCal 2010, and the right camera during Hires 2010.

7. **3D Velocity calculation.** Each 3D point computed in the stereo processing corresponds to a specific pixel location in the original image. Using the separation between points in both pixel and real coordinates, it is possible to derive a relation between pixels and metres for every pixel location in the image. That relation is then used to convert PIV measurements of pixels/s to m/s.

8. **Gridding data** Further processing required that velocity measurements be interpolated to a uniform grid. Linear interpolation (Matlab `TriScatteredInterp`) was performed using a re-gridding resolution of approximately twice the 95th percentile PIV sampling resolution of an image sequence. These resolutions were 2cm for RaDyO 2009 and 1cm for SoCal 2010, the difference being due to the lower boom elevation and consequent smaller field of view during the SoCal 2010 experiment.

Example reconstructed surfaces and velocity fields are shown in Figure 3.2

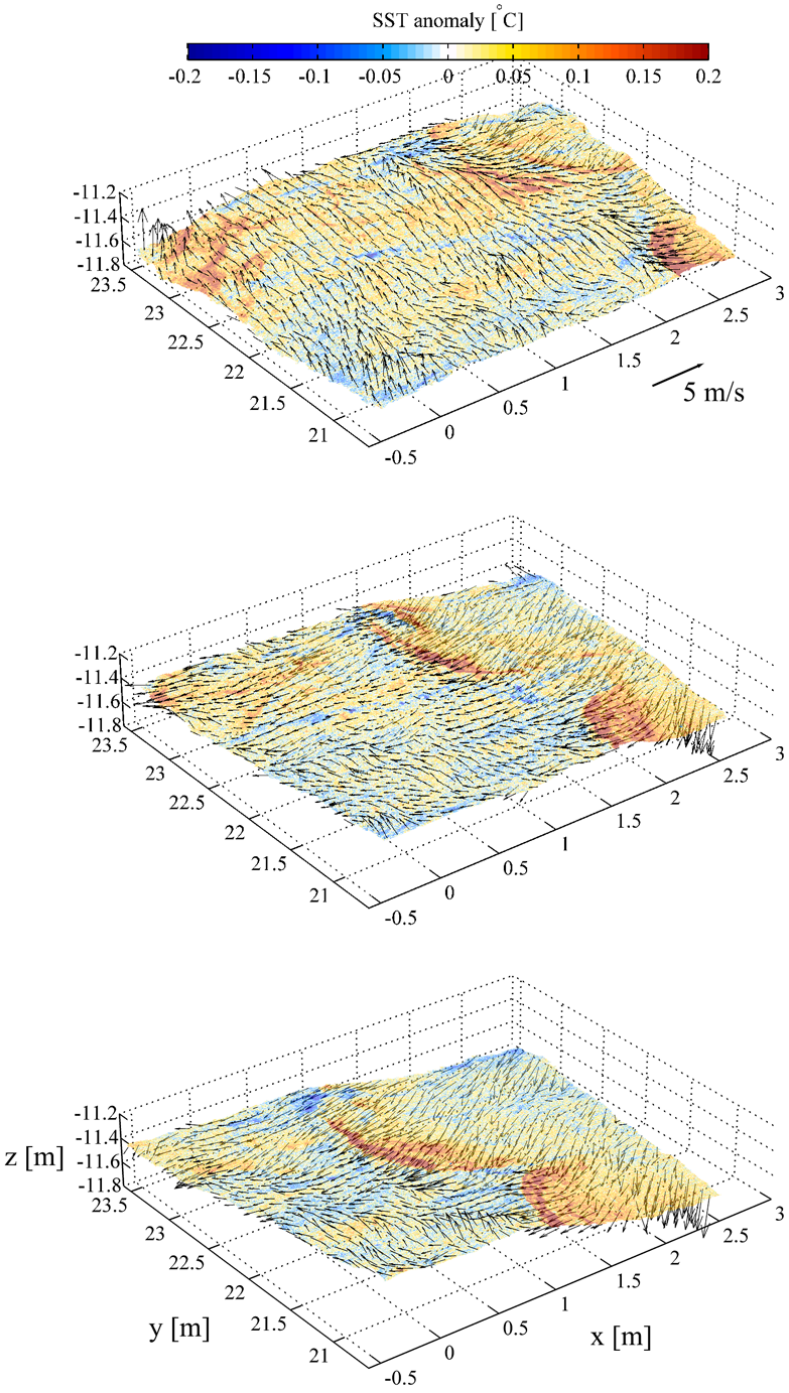

Figure 3.2: Example stereo IR reconstruction of the sea surface. Images were taken starting at 2009/09/08 11:07:29.25 [UTC] and are separated by 0.25 s. Coloring shows surface temperature anomaly and black arrows show surface velocity. Arrows have been decimated to 1/4 resolution and scaled to 10%; a 10 cm arrow indicates 1 m/s velocity. The corresponding vorticity fields are shown in figure 3.3

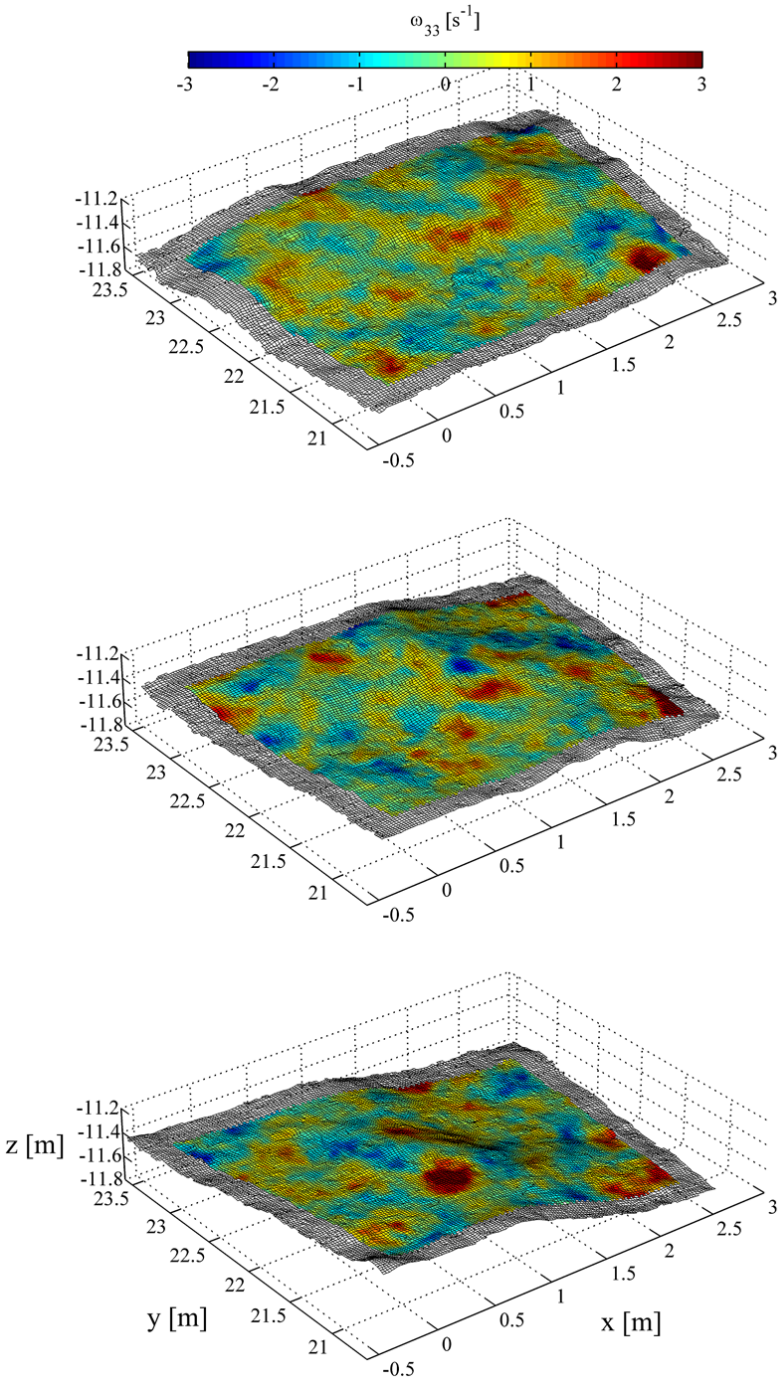

Figure 3.3: Example stereo IR reconstruction of the sea surface showing surface vertical vorticity field. The corresponding temperature and velocity fields shown in figure 3.2. Images were taken starting at 2009/09/08 11:07:29.25 [UTC] and are separated by 0.25 s. The vorticity has been filtered with a 20 cm 2D Gaussian filter in order to highlight larger scale structure around the breaker.

Chapter 4

Infrared measurements of Breaking Statistics

4.1 Introduction

The air-sea interface has a profound effect on weather and climate, with deep-water breaking waves playing an important role (*Banner and Peregrine* 1993, *Melville* 1996, *Duncan* 2001). Energy dissipation by breakers limits growth of the surface wave field and provides a mechanism for momentum transfer from waves to currents. Bubbles and aerosols produced by breaking support gas and heat transfer between the ocean and atmosphere. Breaking statistics are very difficult to simulate in the laboratory or to model numerically and so field measurements are necessary for progress.

Phillips (1985) defined a distribution of breaker front length $\Lambda(\boldsymbol{c})$ per unit area of sea surface per unit increment of breaking front velocity $\boldsymbol{c}(c, \theta)$, where c and θ are the speed and direction of breaker front propagation, respectively.

Integrating $\Lambda(\boldsymbol{c})$ azimuthally (*Kleiss and Melville* 2010) yields a distribution that is a function of only speed

$$\Lambda(c) = \int_0^{2\pi} c\Lambda(\boldsymbol{c}(c, \theta))d\theta. \tag{4.1}$$

The moments of $\Lambda(\boldsymbol{c})$ have important physical interpretations. The fraction of surface area turned over by breaking fronts per unit time, is the first moment

of $\Lambda(c)$ (*Phillips* 1985)

$$R = \int c\Lambda(c)dc, \tag{4.2}$$

which is related to heat and gas transfer between the ocean and the atmosphere (*Jessup et al.* 1997).

Phillips (1985) showed that the average rate of gravity wave energy loss per unit area by breakers with velocities between $\boldsymbol{c}$ and $\boldsymbol{c} + d\boldsymbol{c}$ can be written,

$$\epsilon(\boldsymbol{c})d\boldsymbol{c} = bg^{-1}\rho_w c^5 \Lambda(\boldsymbol{c})d\boldsymbol{c}. \tag{4.3}$$

where g is the gravitational acceleration, ρ_w is the water density, $\boldsymbol{c}$ is the breaker front velocity, and b is the dimensionless breaking parameter.

Integrating over all breaker speeds c, the 5th moment of $\Lambda(c)$ gives the total gravity wave energy dissipated by breaking waves per unit area of ocean surface,

$$F_E = \frac{\rho_w}{g} \int bc^5 \Lambda(c)dc. \tag{4.4}$$

Similarly, the 4th moment of $\Lambda(\boldsymbol{c})$ yields the momentum flux from the wave field into the upper ocean,

$$\boldsymbol{F_m} = \frac{\rho_w}{g} \int bc^3 \boldsymbol{c} \Lambda(\boldsymbol{c})d\boldsymbol{c}. \tag{4.5}$$

Phillips (1985) used a constant value for b and, by assuming an equilibrium wave spectrum, predicted that $\Lambda(c) \propto c^{-6}$ (see Appendix A). More recent laboratory work using focusing wave packets (*Melville* 1994, *Banner and Peirson* 2007, *Drazen et al.* 2008) has shown that b varies over at least 3 orders of magnitude. For plunging breakers, *Drazen et al.* (2008) predicted that b is proportional to $S^{5/2}$, where S is the linear focusing slope at breaking. *Romero et al.* (2012) showed that $b = 0.4(S - 0.08)^{5/2}$ fit all available laboratory data, from incipient to plunging breaking, and used it to create a semi-empirical spectral model of the breaking parameter in the field,

$$b(k) = A_1(B(k)^{1/2} - B_T^{1/2})^{5/2}. \tag{4.6}$$

Here $B(k)$ is the azimuth-integrated saturation spectrum, with the wavenumber k related to c using the linear dispersion relation for deep-water gravity waves. B_T and A_1 are constants that were determined by balancing wave field dissipation

(*Romero and Melville* 2010) with the dissipation from breaking calculated with Equation 4.3, using the field measurements of $\Lambda(c)$ by *Kleiss and Melville* (2010). This model for $b(k)$ was used by *Romero et al.* (2012) to predict a form of $\Lambda(c)$, at low c values, that extended roughly from the peak of the field measurements of *Kleiss and Melville* (2010) to the peak of the laboratory measurements of *Jessup and Phadnis* (2005).

Several studies have undertaken direct measurements of $\Lambda(\boldsymbol{c})$ in the field, as summarized in Figure 4.1. Though early work by *Phillips et al.* (2001) used radar backscatter, all field measurements since then have used video imagery of the sea surface. *Melville and Matusov* (2002) and *Kleiss and Melville* (2010, 2011) used airborne imagery, while *Gemmrich et al.* (2008) and *Thomson et al.* (2009) used platform-based measurements.

Detection of breakers in video imagery relies on whitecaps being much brighter than the surrounding ocean due to the scattering of light by entrained bubbles and foam. Microscale breakers do not entrain air, and so are essentially undetectable by visible imagery. They do, however, mix the cool skin layer with warmer water below so their warm actively breaking front and wake can be detected in IR imagery (*Zappa et al.* 2001). *Jessup and Phadnis* (2005) used IR video to image wind-generated microscale breakers in the laboratory. Their measured $\Lambda(c)$ showed a much higher density of breakers at lower speeds than previous visible video-based fieldwork.

The primary goal of this work is to include microscale breakers in field measurements of $\Lambda(c)$. This has been achieved by using stereo IR measurements to capture breaking waves in the open sea. To the authors' knowledge, it represents the first successful inclusion of microscale breakers in field measurements of $\Lambda(\boldsymbol{c})$.

4.2 Breaker Detection

In this work, a new technique was developed for breaker detection. Temperature structure in the actively breaking region and turbulent wake of a breaker is less uniform than that in the background surface field. One measure of non-

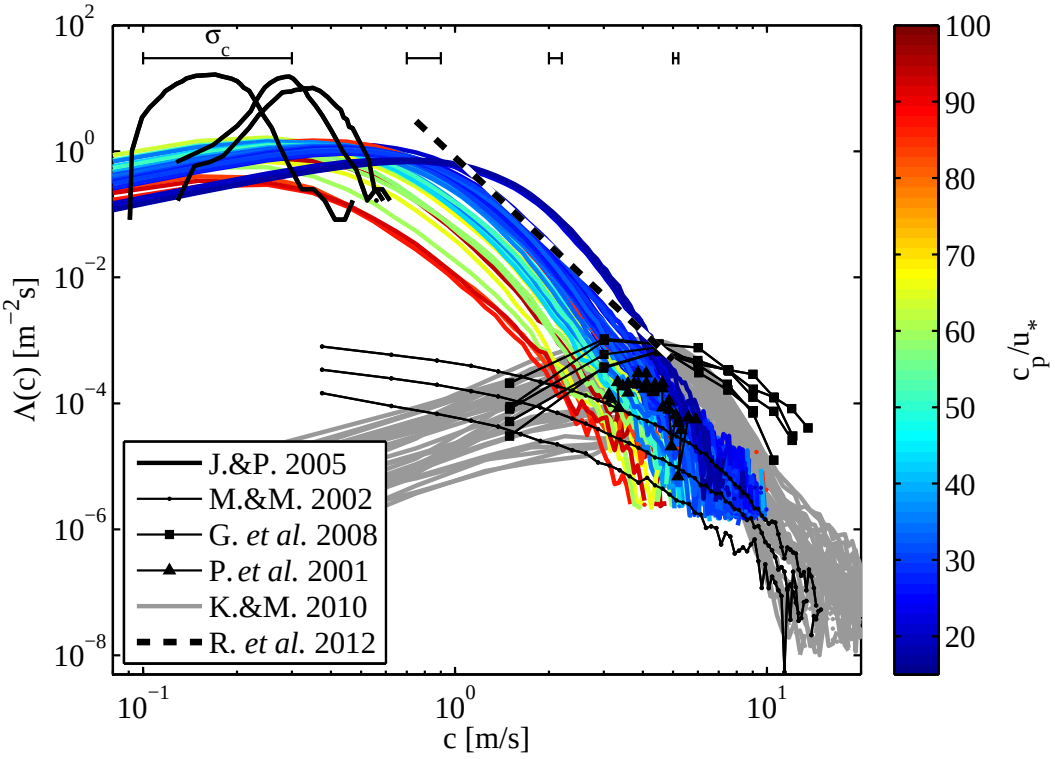

Figure 4.1: Measured $\Lambda(c)$ compared with the literature. Lines colored by wave age are from this work. Thick black lines are from the laboratory measurements of *Jessup and Phadnis* (2005). Field measurements are from: *Melville and Matusov* (2002) lines with small dots, *Gemmrich et al.* (2008) lines with squares, *Phillips et al.* (2001) lines with triangles, and *Kleiss and Melville* (2010) solid gray lines. The black and white dashed line is the modeled extrapolation by *Romero et al.* (2012) of the measurements of *Kleiss and Melville* (2010). Horizontal bars near the top indicate standard deviation of velocity error, calculated using synthetic data.

uniformity in an image is "entropy," which is frequently used in the computer vision and synthetic aperture radar communities to quantify image texture (e.g., *Gonzalez et al.* 2009, *Holmes et al.* 1984).

Local entropy was used to detect breaking waves in infrared imagery. An example of the breaker detection sequence is shown in Figure 4.2. Entropy is defined as

$$E = -\sum_i p_i \log_2(p_i), \tag{4.7}$$

where p_i is the ith component of a histogram of the intensity of the image pixels. The entropy filter used in this work calculated the value of E using 9×9 pixel windows surrounding each pixel in the image. Before processing, the 20-minute-average temperature field was removed from each image, so all temperatures were anomalies relative to that mean. The histograms were then defined such that the minimum bin corresponded to a value of zero, and thus the entropy filter only picked out regions of high entropy that also had temperatures above the mean value. This positive-only selection was made intentionally; breaking disrupts the cool surface skin layer, resulting in warm anomalies (*Zappa et al.* 2001) so only regions of high entropy that were also warm anomalies were considered to be possible breakers. This assumes that the bulk water temperature was higher than the skin temperature to at least the depth mixed by breaking. The assumption can be easily tested. If the largest breakers (as identified in visible data) appear as warm anomalies, then the skin temperature must be cooler than the bulk temperature to at least the depth of the largest breakers, and thus the depths of all smaller breakers. All data analyzed in this work passed this test. However, it is important to realize that this assumption regarding the cool skin layer may not be true globally (*Donlon and Robinson* 1997).

Distributions of entropy for each image were used to determine the entropy threshold for that image. Figure 4.3 illustrates the technique. Excluding pixel windows with negative temperature anomalies, the distributions contained a flat region starting above $E = 0$ which extended to a peak, typically between $E = 1.5$ and $E = 4$, corresponding to regions with elevated entropy associated with breaking. The entropy threshold was chosen to be the boundary between the flat

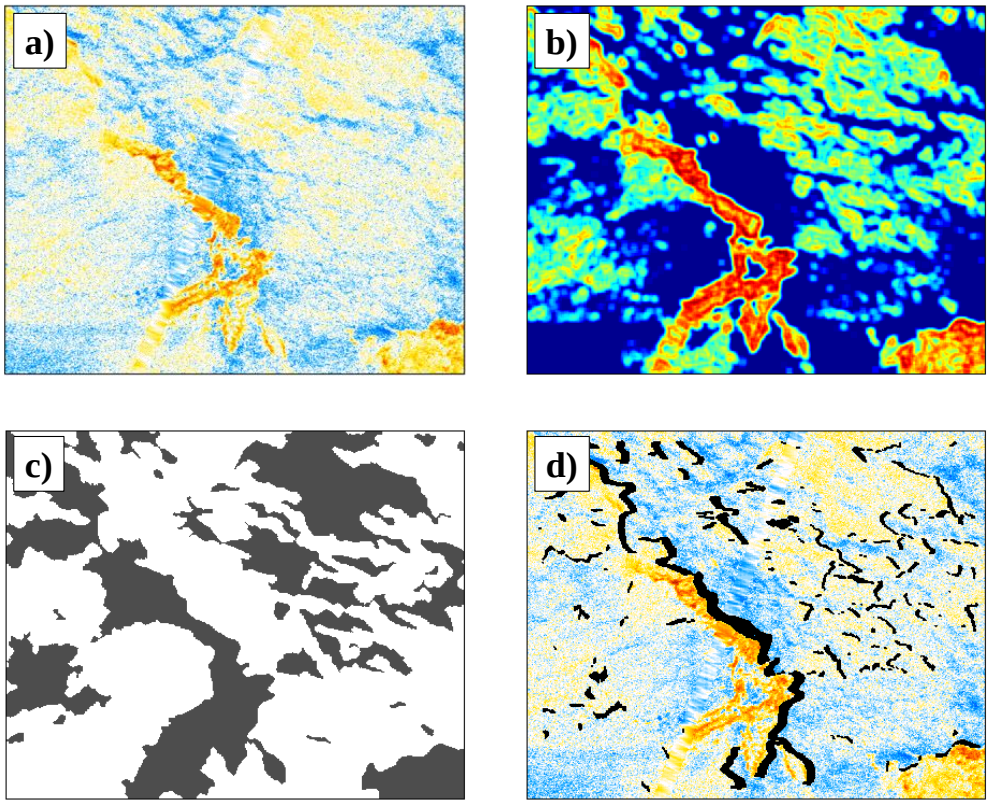

Figure 4.2: Example breaker detection sequence. a) Raw image with data cable and 20-minute mean removed. b) Image entropy (red corresponds to high entropy, blue to low). c) Regions above entropy threshold are selected (gray regions). d) Actively breaking fronts selected (black arrows). The final step is conversion from image to earth coordinates. The result is shown in Figure 4.7.

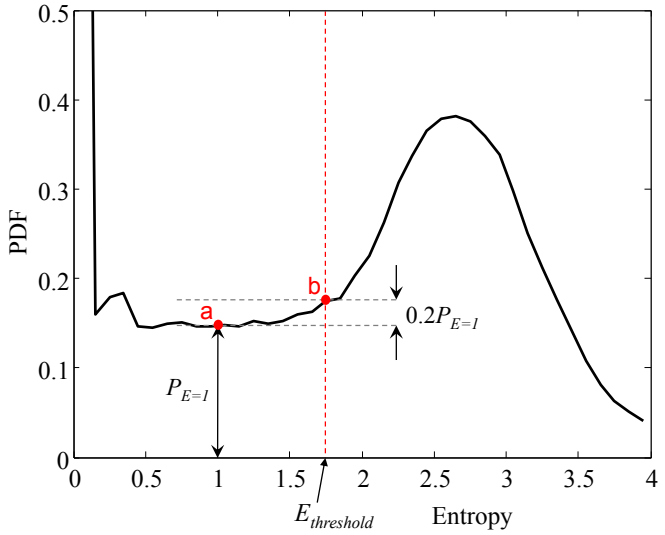

Figure 4.3: Probability density function of IR image entropy for a single example image (taken December 6, 2010 22:00 [UTC]) showing the features used for calculating the entropy threshold. $P_{E=1}$, the value of the PDF at an entropy value of $E = 1$ was found (point a). Then the lowest entropy value for which the distribution exceeded $1.2 \times P_{E=1}$ was located (point b) and set as the entropy threshold, $E_{threshold}$.

region and the slope to the peak. First, $P_{E=1}$, the value of the PDF at an entropy value of $E = 1$ was found (point a in this example). Then the lowest entropy value for which the distribution exceeded $1.2 \times P_{E=1}$ was located (point b in this example) and set as the entropy threshold, $E_{threshold}$, for that image. The value 1.2 was chosen as it gave best agreement with visible data for large air-entraining breakers; figure 4.4 shows the sensitivity of $\Lambda(c)$ to this selection. Analysis of imagery from the HiRes 2010 experiment differed slightly. In that experiment, the low air-water temperature difference and strong conditions produced IR imagery with very little contrast. This meant that the peak of the entropy distribution was not as elevated, often barely exceeding $1.2 \times P_{E=1}$. For this data, the highest value of the distribution with $E > 1$ was found, and the entropy threshold was set to 70% of the entropy value at that maximum.

All regions in each image with entropy above $E_{threshold}$ were chosen as the initial breaking patches.

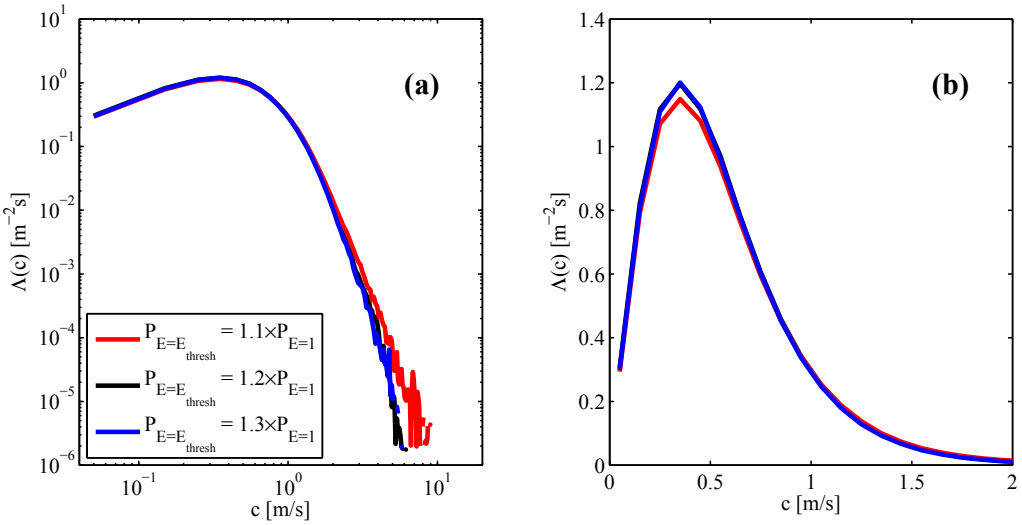

Figure 4.4: Typical sensitivity to entropy threshold used in breaker detection. 20-minute average breaker front length distribution starting December 6, 2010 22:00 [UTC]. (a) Log coordinates. (b) Linear coordinates. The black curve shows the value used in this analysis, with the entropy distribution at the threshold, $P_{E=E_{thresh}}$, equal to 1.2 times the entropy distribution value at $E = 1$, $P_{E=1}$. Choosing $P_{E=E_{thresh}} = 1.1 \times P_{E=1}$ gives the red curve, and choosing $P_{E=E_{thresh}} = 1.3 \times P_{E=1}$ gives the blue one. Clearly $\Lambda(c)$ has a dependence on the chosen threshold. However, for slow breakers, with c less than approximately 2 m/s, $\Lambda(c)$ is relatively insensitive to small changes in threshold value. For fast breakers the sensitivity is greater, but the threshold was chosen so that breakers detected in IR agreed with those detected in visible imagery at those speeds.

The edges of the initial breaking patches were smoothed by eroding and then dilating using a 3×3 pixel diamond-shaped morphological structuring element (*Gonzalez et al.* 2009). Internal holes in the patches were then filled and all patches with a total area of less than 100 pixels were discounted to remove noise.

Pixel velocities for each patch boundary were calculated using particle imaging velocimetry (PIV), and those velocities were converted to 3D georeferenced velocities using the stereo surface reconstruction. Only the horizontal component of velocity was retained for breaker front analysis. The mean velocity of the non-breaking sea surface was then removed from the breaking front velocities to remove long wave orbital velocities from breaking fronts.

Only patches with mean velocities within 90° of the 20-minute mean wind direction were retained. This assumes that all breakers propagate with a positive downwind component of velocity and was done to remove any apparent backwards propagation due to surfacing bubbles after a wave had broken. Once final patches were selected, the pixels around that patch's perimeter were deemed potential candidates for actively breaking fronts. To find the actively breaking front of each breaking patch, the velocities of perimeter pixels were inspected, and only pixels with velocities outward from the (local) interior of the patch were considered to define the breaking front. These actively breaking pixels were recorded along with their horizontal velocity $\boldsymbol{v}_p$, speed $v_p = |\boldsymbol{v}_p|$, and associated length scale dl_p. For each 20 minute period, a single $\Lambda(c)$ distribution was calculated as

$$\Lambda(c_i) = \frac{\sum\limits_{p} \left(dl_p \mid (c_i - \frac{\Delta c_i}{2}) \leq v_p < (c_i + \frac{\Delta c_i}{2}) \right)}{\Delta c_i \sum\limits_{k=1}^{N_{frames}} A_k}, \tag{4.8}$$

where c_i is the speed bin center, Δc_i is the bin size, and A_k is the horizontal area of each frame. An analogous calculation was performed to determine the directional distribution $\Lambda(\boldsymbol{c})$.

The technique used for breaker detection in this work is directly analogous to previous methods that tracked the actively breaking front (sometimes called the "toe" or "foot") of a whitecap using visible video (e.g. *Kleiss and Melville* 2011). However, instead of the actively breaking parts being "marked" by bubbles, they

are marked by increased image entropy. It is expected that the surface disruption that causes this increased entropy would occur at least as quickly as the creation of bubbles, since the creation of bubbles requires significant surface disruption. Comparison of co-located imagery of bubble-entraining breakers supports this, with the actively breaking fronts located using IR imagery (entropy) and visible imagery (brightness) occurring in the same location. An example of co-located imagery showing this coincident actively breaking front is shown in Figure 4.6.

4.2.1 Reflections in IR imagery

Reflections on the sea surface, for example, from the structure of *R/P FLIP*, could potentially contaminate the imagery used in this experiment. Thus the setup and analysis were designed with the minimisation of the effects of reflections in mind. Using the entropy filter, rather than a simple brightness threshold eliminates some of the reflections as it requires high entropy as well as above average temperature. Furthermore, the cameras, near the end of *FLIP*'s boom, were angled outwards at approximately 20° from vertical. This angle was chosen so that if the sea surface were flat, there would be no reflections from any part of *R/P FLIP*'s booms or structure visible in the field of view. Nonetheless, reflections were observed in imagery, almost exclusively in the bottom half of the imagery (closer to *FLIP*), where a lower sea surface slope was required to reflect radiation from *FLIP*'s structure back to the cameras. It is possible to check the effect of those reflections by independently calculating $\Lambda(c)$ for the top and bottom halves of the imagery. Figure 4.5 shows an example of this processing. While there are indeed differences, likely attributable to reflections, between $\Lambda(c)$ calculated using the total image vs. image top, or image bottom, those differences are less than 20% at the peak of the distribution. The differences at the high speed range, approximately $c > 3$ m/s are expected due to the statistically low number of breakers with those speeds that cross the area of observation during the sampling period and are not thought to be related to reflections.

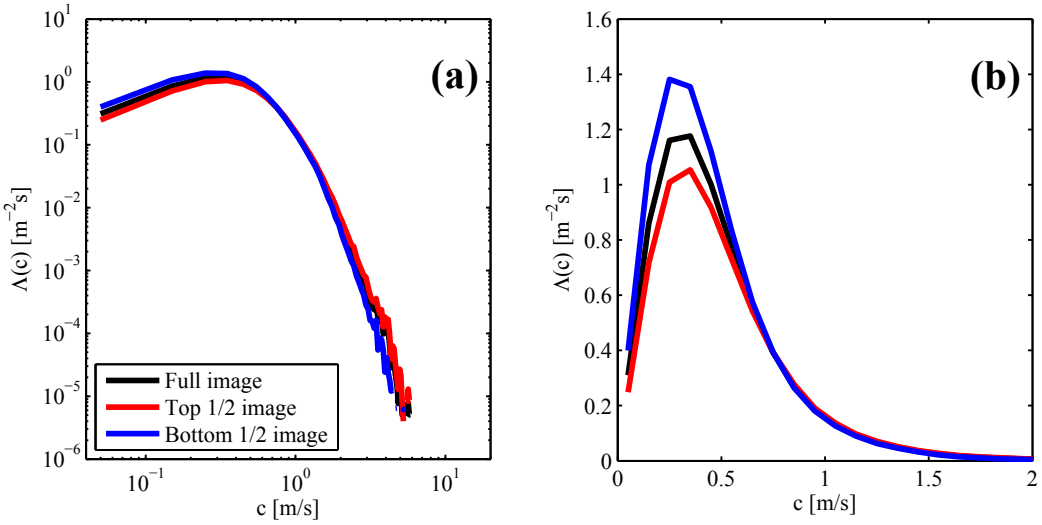

Figure 4.5: Effect of reflections from *FLIP*'s structure on 20-minute average $\Lambda(c)$, starting December 7, 2010 08:00 [UTC]. (a) Log coordinates. (b) Linear coordinates. Distributions calculated using the whole image, the bottom half (with reflections), or the top half (without reflections). This time period was chosen to be local midnight to ensure that the only reflections present would be from the vessel's booms and structure, not sunlight.

4.2.2 Visible breaker detection

Four 10-minute periods of visible video data, corresponding to the first half of their associated IR sampling periods, were analyzed for comparison with the IR data. The technique used was based on that developed by *Kleiss and Melville* (2011). Breakers were located using a "brightness" threshold based on the mean standard deviation of image pixel intensity over 10 minutes of data,

$$\sigma_{I10} = \frac{1}{N_{frames}} \sum_{i=1}^{N} \sqrt{\langle I_i^2 \rangle}. \tag{4.9}$$

Here N_{frames} is the number of images in the sequence, and $\langle I_i^2 \rangle$ is the variance of image intensity in image i. All regions where local image intensity was greater than $3 \times \sigma_{I10}$ were selected as potential breaker candidates. Of these, only patches with a maximum intensity greater than $20 \times \sigma_{I10}$ were considered to be breakers. Actively breaking front selection, 3D reprojection, and calculation of $\Lambda(c)$ then proceeded as described for stereo IR data. The only difference was that the mean background surface velocity was not removed from breaking front velocities because the visible data did not provide a surface velocity field. As discussed in *Kleiss and Melville* (2011), the effects of not removing the underlying long wave orbital motions are small for breakers fast enough to be detectable by visible video.

An example of a breaker detected in both visible and IR imagery can be seen in Figure 4.6 and expanded in Figures 4.7 and 4.8. Note that the main bubble-entraining "whitecap" is obvious in both visible and IR images, with both measurements finding the actively breaking front in the same location with very similar velocities. However, the IR image shows the main breaker extending in the y-direction well beyond the visible whitecap boundary, and also shows several other smaller breakers that are completely undetected in the visible image.

4.3 Results

The $\Lambda(c)$ measurements taken here are shown in Figure 4.1. They show, at the higher speeds, a similar functional dependence on c when compared to other examples from the literature. What sets the measurements in this work

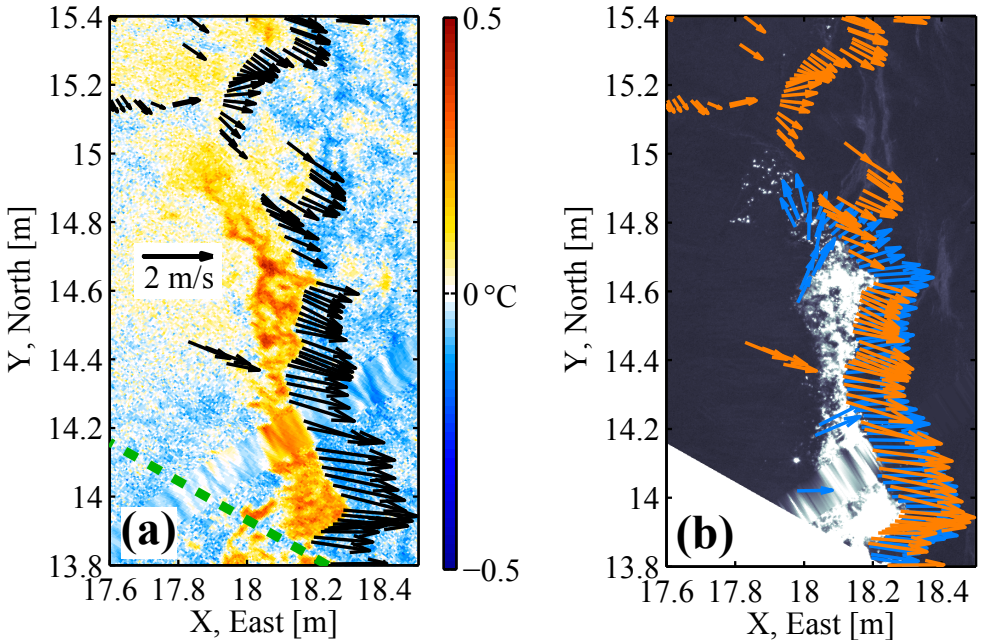

Figure 4.6: Snapshot of a breaker detected in co-located visible and IR imagery, taken during SoCal 2010 experiment, 2010/12/06 22:02:32.75 [UTC]. **(a)** IR image temperature with 20-minute mean removed. Black arrows indicate breaking front velocities [m/s] (scale given in image), Green dashed line indicates the boundary of the cutout in the visible image (white area in (b)). **(b)** Visible (black and white) image. Blue arrows indicate breaking front velocities detected in visible imagery, orange arrows indicate velocities detected in IR. The white area in the lower left was removed from analysis as it contained a subsurface instrument which was visible through the clear ocean water and thus affected breaker detection in visible imagery. Wide field of view versions of these images are shown in figure 4.7 and 4.8.

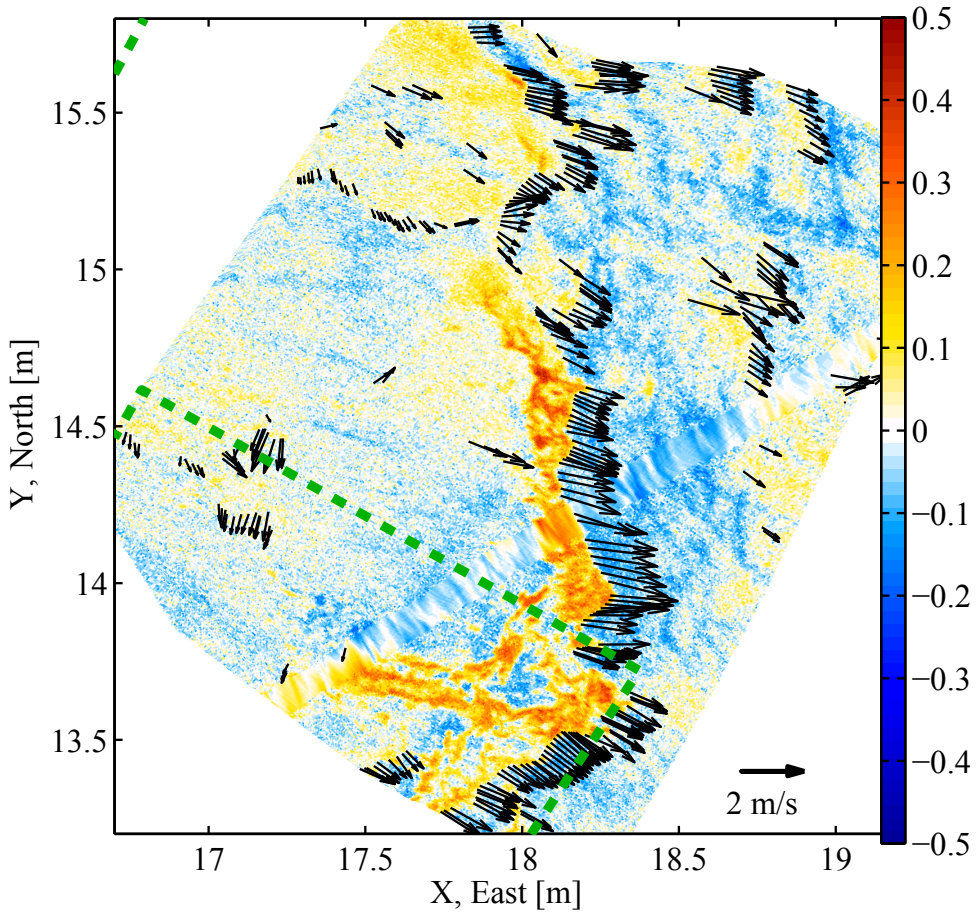

Figure 4.7: Snapshot of a breaker detected in IR imagery, taken during SoCal 2010 experiment, 2010/12/06 22:02:32.75 [UTC]. Wide field of view version of Figure 4.6 **(a)**; IR image temperature with 20-minute mean removed. Black arrows indicate breaker front velocities [m/s] (scale given in image), Green dashed line indicates the boundary of the cutout in the visible image. The blurry line, approximately 0.1 m wide, that extends from approximately (17.2,13.6) to (19.2,14.8) was the location of a cable that supported underwater instrumentation. The cable was removed from imagery and the resulting gap interpolated over.

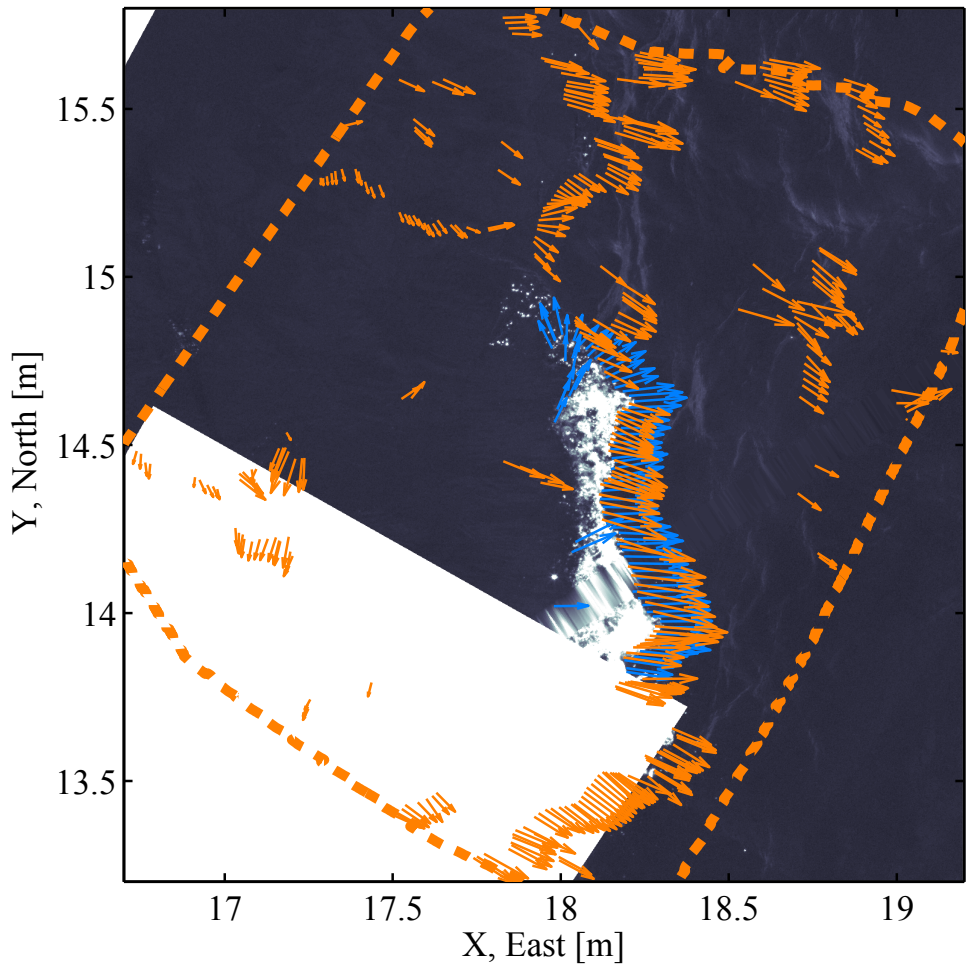

Figure 4.8: Snapshot of a breaker detected in visible imagery, taken during SoCal 2010 experiment, 2010/12/06 22:02:32.75 [UTC]. Wide field of view version of Figure 4.6 **(b)**; visible (black and white) image. Blue arrows indicate breaker front velocities detected in visible imagery, orange arrows indicate velocities detected in IR. The orange dashed line shows the boundary of the IR image. The white area in the lower left was removed from analysis as it contained a subsurface instrument which was visible through the clear ocean water and thus affected breaker detection in visible imagery.

apart is their low-speed behavior, extending the field measurements of *Melville and Matusov* (2002), *Gemmrich et al.* (2008), *Kleiss and Melville* (2010), and others. They also appear to have a similar peak speed to the laboratory measurements of *Jessup and Phadnis* (2005) though that agreement may be coincidental.

A recurring question in the literature is whether or not $\Lambda(c)$ should roll-off below some breaking speed c (*Gemmrich et al.* 2008, *Kleiss and Melville* 2011). As can be seen in Figure 4.9, including microscale breakers has a very large effect on the level of $\Lambda(c)$ at low c. Both visible and IR measurements capture breaking fronts well for breakers with speeds above 2–3 m/s. Below that speed visible measurements fail, likely due to the lack of air-entrainment. The IR measurements presented here do not display a similar roll-off until c reaches between 10 and 80 cm/s. The standard deviation of velocity error was calculated to be approximately 20 cm/s, which likely broadens the peak in the $\Lambda(c)$ distributions. Further supporting the general form of these low c results is their similarity to the modeling work of *Romero et al.* (2012). By using a theoretical extrapolated wave saturation spectrum, they predicted that $\Lambda(c)$ given by *Kleiss and Melville* (2010) should increase from the measured peak as c decreases, as shown in Figure 4.1.

4.4 Scaling $\Lambda(c)$

A dimensional analysis of the dependence of $\Lambda(c)$ on the other variables and parameters leads to an improved understanding of the breaking process. $\Lambda(c)$ can be written as $\Lambda(c; \rho_a, \rho_w, u_*, g, c_p, H_s, \Gamma, X)$, where ρ_a is the air density, u_* is the atmospheric friction velocity, c_p is the phase speed of waves at the peak of the wind-wave spectrum, H_s is the significant wave height, Γ is the surface tension, and X is the wave fetch. Dimensional analysis then yields

$$\Lambda(c) c_p^3 g^{-1} = f\left(\frac{c}{\sqrt{gH_s}}, \frac{\rho_a}{\rho_w}, \frac{c_p}{u_*}, \frac{gH_s}{c_p^2}, \frac{gX}{c_p^2}, Bo\right), \tag{4.10}$$

Here $\sqrt{gH_s}$ is the speed attained in a ballistic trajectory from a height of $H_s/2$, c_p/u_* is the wave age, gH_s/c_p^2 is the wave steepness, gX/c_p^2 is the dimensionless fetch, and Bo is the Bond number. The spectral Bond number, $Bo = (\rho_w -$

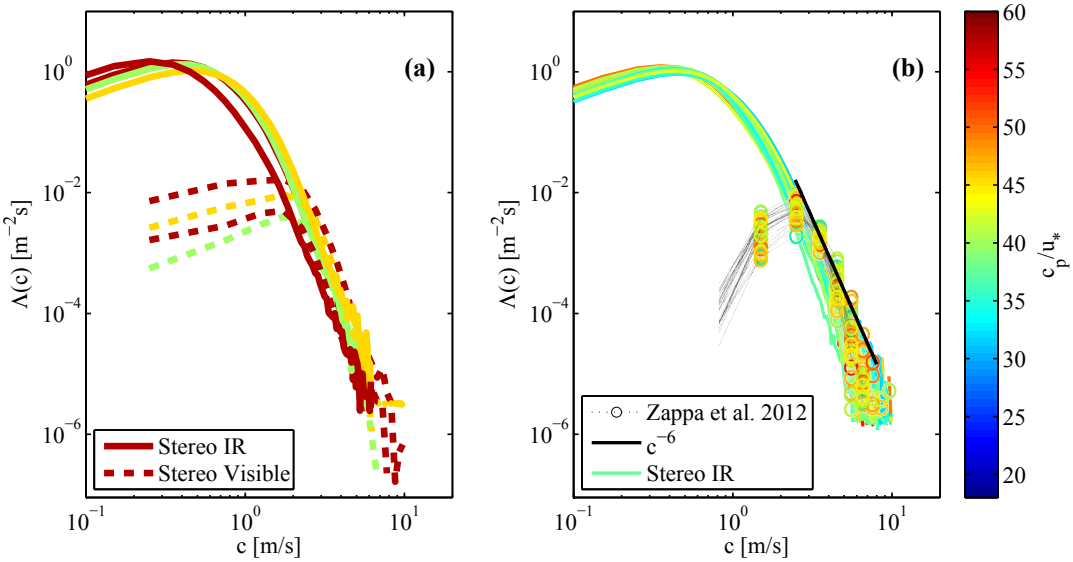

Figure 4.9: Comparison of $\Lambda(c)$ measured using visible and IR video. Color corresponds to wave age. **(a)** Shows distributions from concurrent, co-located IR video (solid lines) and visible video (dashed lines) taken during the SoCal 2010 experiment. **(b)** Shows $\Lambda(c)$ measured during the RaDyO 2009 experiment using stereo IR (colored lines) compared with $\Lambda(c)$ measured during the same experiment by *Zappa et al.* (2012) using visible imagery (colored circles). The solid black line is the c^{-6} dependence predicted by *Phillips* (1985) as shown in *Zappa et al.* (2012).

$\rho_a)c^4/g\Gamma$ is greater than 10 for $c > 29$ cm/s, implying that surface tension effects are negligible for speeds larger than this. Our rms error in c is ± 20 cm/s, so surface tension effects are negligible over most of the range of c and are neglected in this analysis. However, since the ratio $(\rho_w - \rho_a)/g\Gamma$ remained effectively constant over all experiments, these measurements had no significant Bond number dependence. Neglecting the Bond number, assuming that ρ_a/ρ_w is approximately constant, and assuming that in fetch-limited conditions X can be related to c_p, H_s, u_* and g, Equation 4.10 can be simplified to

$$\Lambda(c)c_p^3 g^{-1} = f\left(\frac{c}{\sqrt{gH_s}}; \frac{c_p}{u_*}, \frac{gH_s}{c_p^2}\right). \tag{4.11}$$

Assigning the wave age dependence to the ordinate and the steepness dependence to the abscissa, and assuming a power law dependence on both wave age and steepness, gives

$$\Lambda(c)\frac{c_p^3}{g}\left(\frac{c_p}{u_*}\right)^{\alpha} = f\left(\frac{c}{\sqrt{gH_s}}\left(\frac{gH_s}{c_p^2}\right)^{\gamma}\right). \tag{4.12}$$

Applying this scaling to all the stereo IR $\Lambda(c)$ distributions of Figure 4.1 and then varying α and γ to collapse the curves (by minimizing a squared-difference cost function) gave values of $\alpha = 0.5$ and $\gamma = 0.1$. Using those values, it is then possible to re-write Equation 4.12 as

$$\Lambda(c)\frac{c_p^3}{g}\left(\frac{c_p}{u_*}\right)^{0.5} = f\left(\frac{c}{\sqrt{gH_s}}\left(\frac{gH_s}{c_p^2}\right)^{0.1}\right) = f\left(\hat{c}\right), \tag{4.13}$$

where $\hat{c}$ is the scaled breaker front speed. This form of $\hat{c}$ suggests that the relevant velocity for scaling breaker front length distributions is $\sqrt{gH_s}$, with a weak dependence on the peak wave steepness, $H_s k_p = gH_s/c_p^2$. The ballistic velocity, $\sqrt{gH_s}$, has been used by previous authors for scaling breaking processes. *Drazen et al.* (2008) used it along with inertial scaling of dissipation to obtain the $S^{5/2}$ slope dependence of the breaking parameter that *Romero et al.* (2012) used to deduce Equation 4.6.

Figure 4.10 shows $\Lambda(c)$ measurements from stereo IR and stereo visible, as well as the airborne visible measurements of *Kleiss and Melville* (2010), scaled using Equation 4.13. For speeds higher than the distribution peak, found between

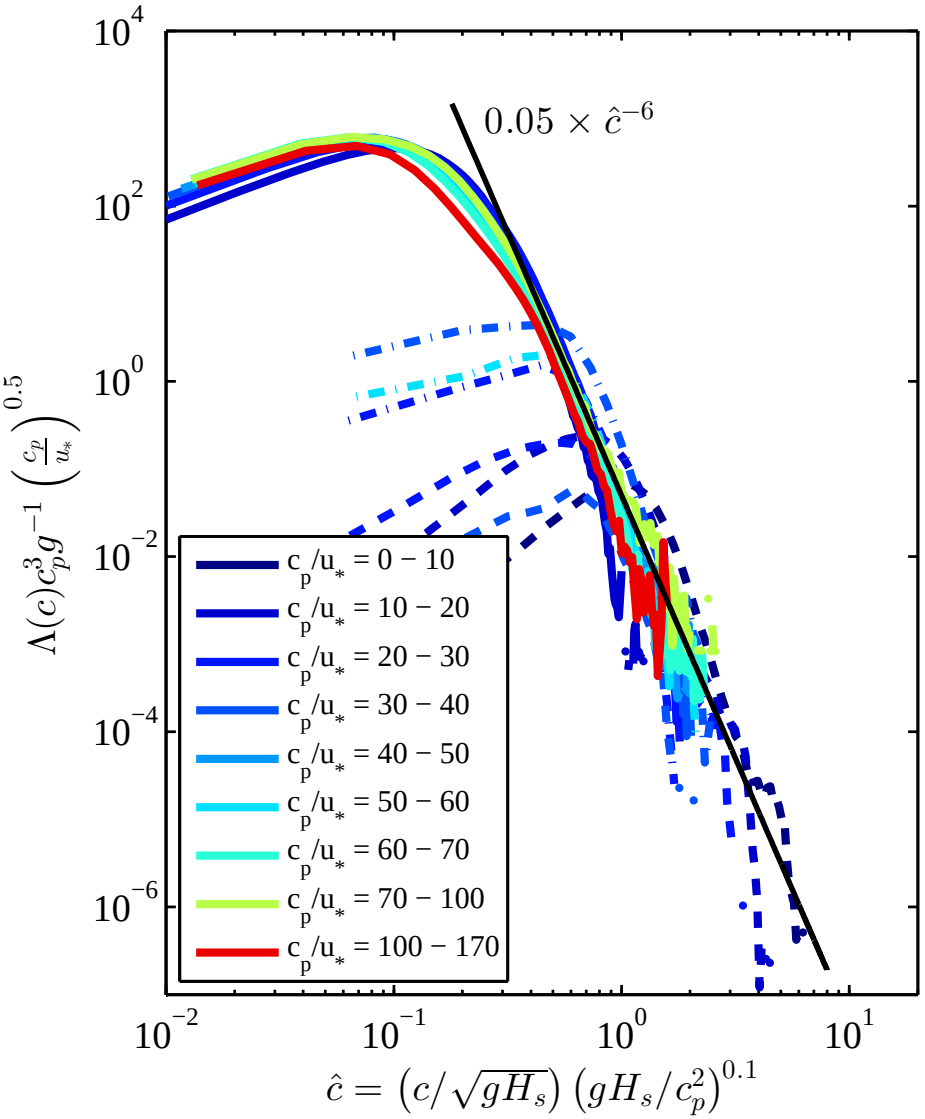

Figure 4.10: Nondimensional breaking length distribution. Distributions have been binned by wave age with corresponding colors. Solid lines are measurements taken in this work using stereo IR imagery, dash-dot lines are from visible imagery in this work, and dashed lines are from the airborne measurements of *Kleiss and Melville* (2010). Scaling uses ballistic velocity, steepness, and wave age dependence from Equation 4.13.

$\hat{c} = 0.06$ and 0.1, this scaling collapses all stereo IR measurements to a narrow curve. For larger speeds, that curve approaches $0.05 \times \hat{c}^{-6}$, exhibiting the power law dependence predicted by *Phillips* (1985). One curve, corresponding to the range $c_p/u_* = 10 - 20$ fails to collapse as well as the others. Those data were taken during the HiRes 2010 experiment during which strong conditions and low air-water temperature differences reduced contrast in the IR imagery and made detection of breakers less reliable than in the other experiments. Thus it is possible that the premature roll-off at low and high speeds of the $c_p/u_* = 10 - 20$ curve is due to measurement limitations rather than the breakers themselves.

While the $\hat{c}^{-6}$ regions of the distributions measured using visible video show reasonable agreement with the high-speed region of the stereo IR distributions, the regions at velocities below the peaks of the visible video data, at approximately $\hat{c} = 0.8$, do not. This supports the hypothesis that the peaks found in $\Lambda(c)$ distributions measured using visible video are a result of their inability to measure breakers that do not entrain air. It also suggests that $\hat{c} = 0.8$ may be an important dynamic transition for air entrainment by breaking.

The ability to nondimensionalize $\Lambda(c)$ over the wide range of wind and wave conditions in these experiments is an important step towards parameterization of wave breaking statistics. Peak wave speed, friction velocity, and significant wave height are much more commonly and easily measured than $\Lambda(c)$.

4.5 Discussion

Until now, results have been presented with no assumptions made regarding the relationship between the speed of the breaking front c, and the phase speed of the underlying wave c_w. However, *Phillips* (1985) and others have assumed that $c_w = ac$, where a is a constant of proportionality approximately equal to 1. In this discussion section, we explore the dynamics assuming $c_w = c$. Using Equation 4.4, with the breaking parameter $b(k)$ as modeled in Equation 4.6 and mapped to $b(c)$ using the linear dispersion relation for surface gravity waves, it is possible to estimate the total integrated dissipation by wave breaking. Since *Romero et al.*

(2012) developed the expression for $b(c)$ in the context of surface gravity waves, $b(c)$ can only be used for speeds where the inclusion of surface tension has little effect. For the following analysis, the restriction of $c > 0.29$ m/s was applied, corresponding to wavenumbers at which the spectral Bond number (Section 4.4) is greater than 10.

Figure 4.11 (a) shows dissipation from measured breaking plotted against a model of the integrated spectral wave dissipation. The spectral wave dissipation model, S_{ds}, is from *Romero and Melville* (2010), and based on *Alves and Banner* (2003). Wind input was calculated using the formulation of *Janssen* (1991). Visually, agreement is good. For wave ages below $c_p/u_* = 50$, the relationship between dissipation by breaking and modeled dissipation is approximately linear. For very old waves, the linear relationship breaks down, suggesting that either breaking is not the dominant mechanism for wave dissipation, or the dissipation model fails, at high wave ages. Figure 4.11 (b), shows that similarly, momentum flux from breaking approaches equivalence with wind stress at low wave ages. The scatter in both the dissipation and stress is well within the scatter of the data used by *Romero et al.* (2012) to parameterize $b(k)$ in their model.

It is illustrative to investigate the relative importance of microbreaking on the integrated moments of $\Lambda(c)$. Figure 4.12 shows $\Lambda(c)$ and its first, fourth, and fifth moments from this experiment and from the literature. Clearly the lower moments of $\Lambda(c)$ are more affected by microbreaking than are the higher ones. The transition between air-entraining breakers and microbreakers can be considered to be the peak of the $\Lambda(c)$ distribution for breakers detected using visible video. From Figures 4.1 and 4.9 that peak is found at approximately $c > 2$ m/s. Figure 4.13 shows a similar comparison to that in Figure 4.11. However, in Figure 4.13, 2 m/s has been used as the lower limit of integration for the moments of $\Lambda(c)$ plotted on the ordinates. This was to remove the effect of micro-breaking from the integrated quantities. The results are dramatic, with a reduction of dissipation by a factor of between 2 and 5. Stress at very low wave ages was unaffected, whereas at large wave ages, the stress was reduced by up to an order of magnitude. The effect of including micro breaking in the calculation of lower moments of $\Lambda(c)$ is even more

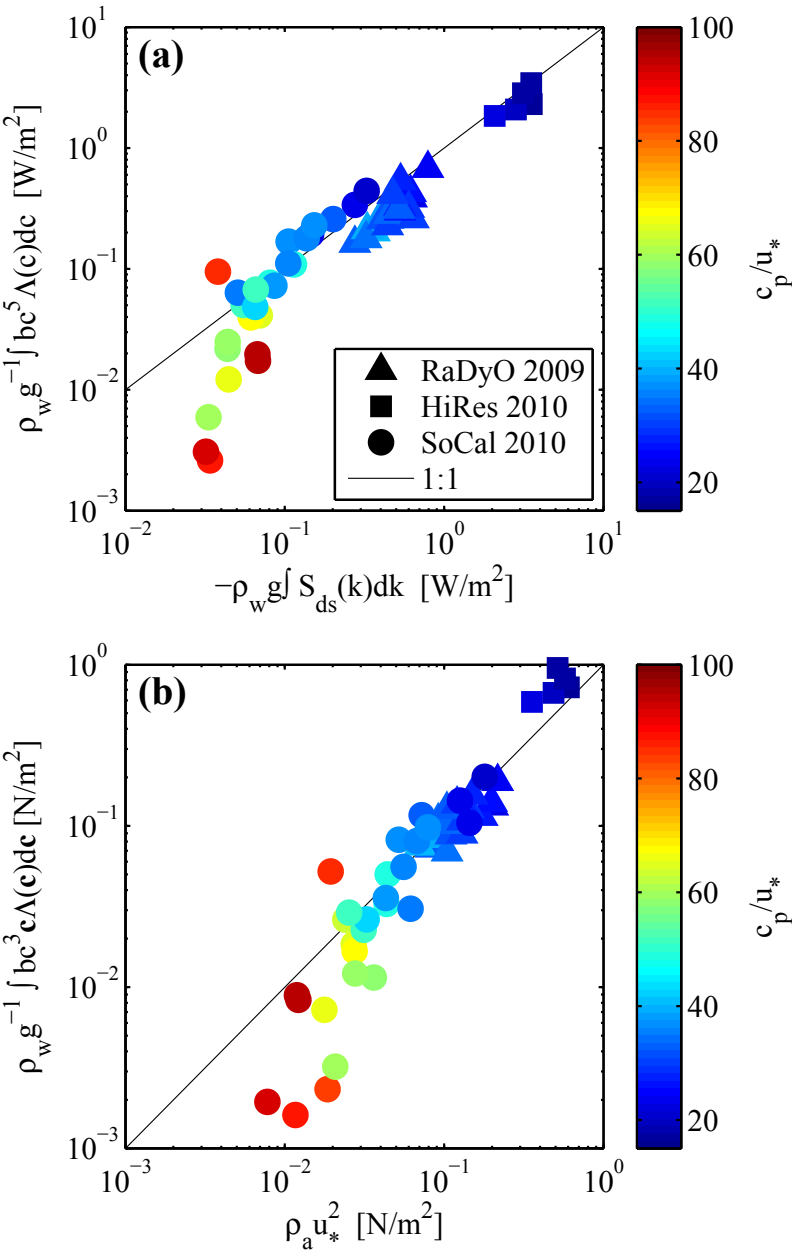

Figure 4.11: **(a)** Dissipation by breaking (ordinate) compared with modelled wave field dissipation (abscissa). **(b)** Momentum flux from waves to currents due to wave breaking (ordinate) plotted against wind stress (abscissa). Color corresponds to wave age and solid line indicates 1:1 correspondence.

dramatic. Figure 4.14 a) shows the results of calculating the integral of $\Lambda(c)$ with limits of integration $2 < c < \infty$ versus $c_{gc} < c < \infty$, where $c_{gc} = 23$ cm/s is the gravity-capillary phase speed minimum that has otherwise been the lower limit of integration. Measuring only air-entraining breakers would under-estimate both the crest length per unit area, and the number of breakers passing a given point per unit time, by 1-2 decades. The implications of this are discussed in the context of dissipation variability at the sea surface in section 5.6.2.

Much of the material in chapter 4 has been published in Sutherland, P. and Melville, W. K. (2013), Field measurements and scaling of ocean surface wave-breaking statistics, *Geophysical Research Letters*, **40**, grl.50584. Supplementary material from that paper has been integrated into the text and additional figures/text have been added. The dissertation author was the primary investigator and author of that paper.

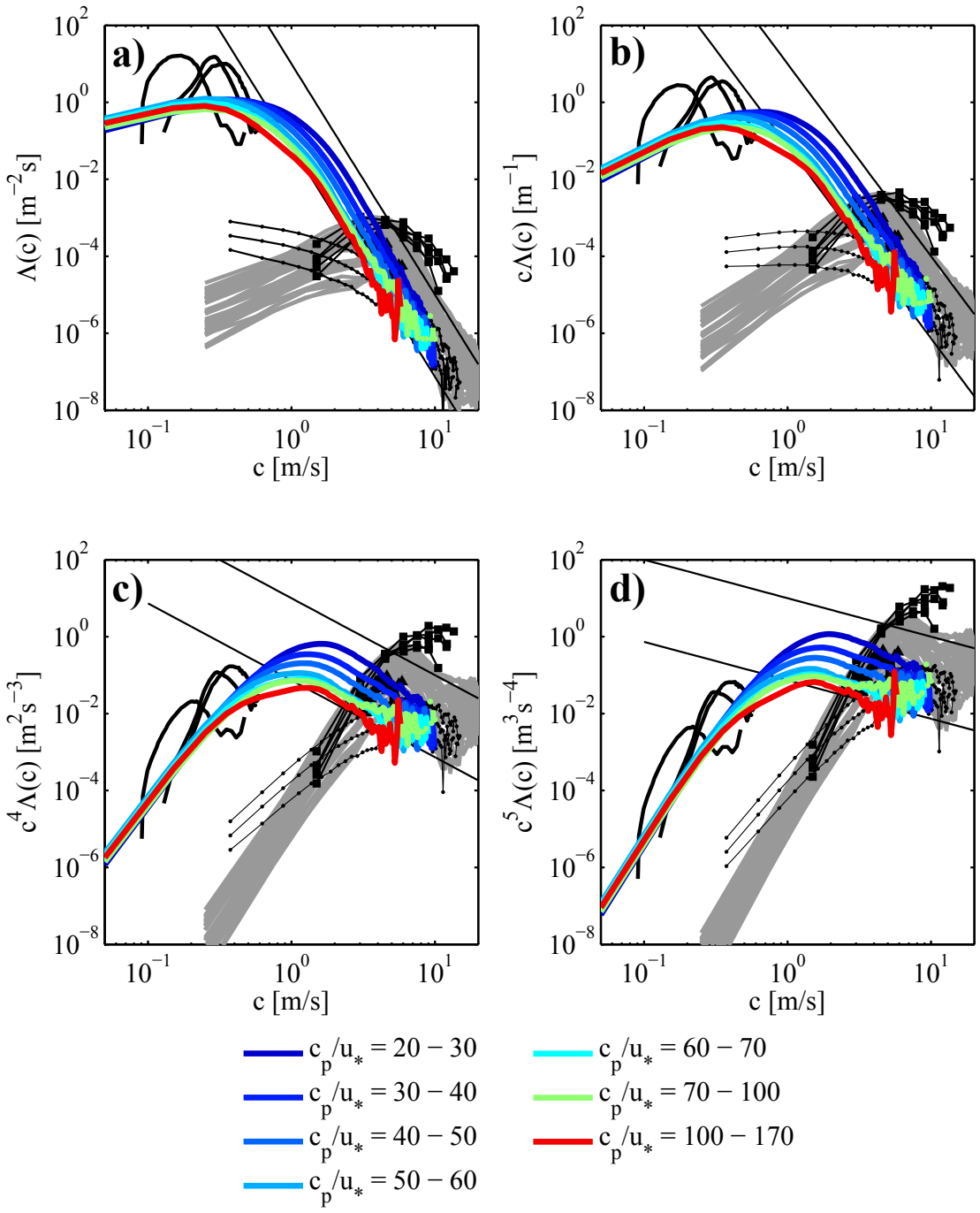

Figure 4.12: Moments of $\Lambda(c)$: a) zeroth, b) first, c) fourth, and d) fifth. Colored lines are data from this work, binned by wave age. Data from the literature is the same as in figure 4.1; thick black lines are from the laboratory measurements of *Jessup and Phadnis* (2005). Field measurements are from: *Melville and Matusov* (2002) lines with small dots, *Gemmrich et al.* (2008) lines with squares, and *Kleiss and Melville* (2010) solid gray lines. The thin black lines are c^{-6}.

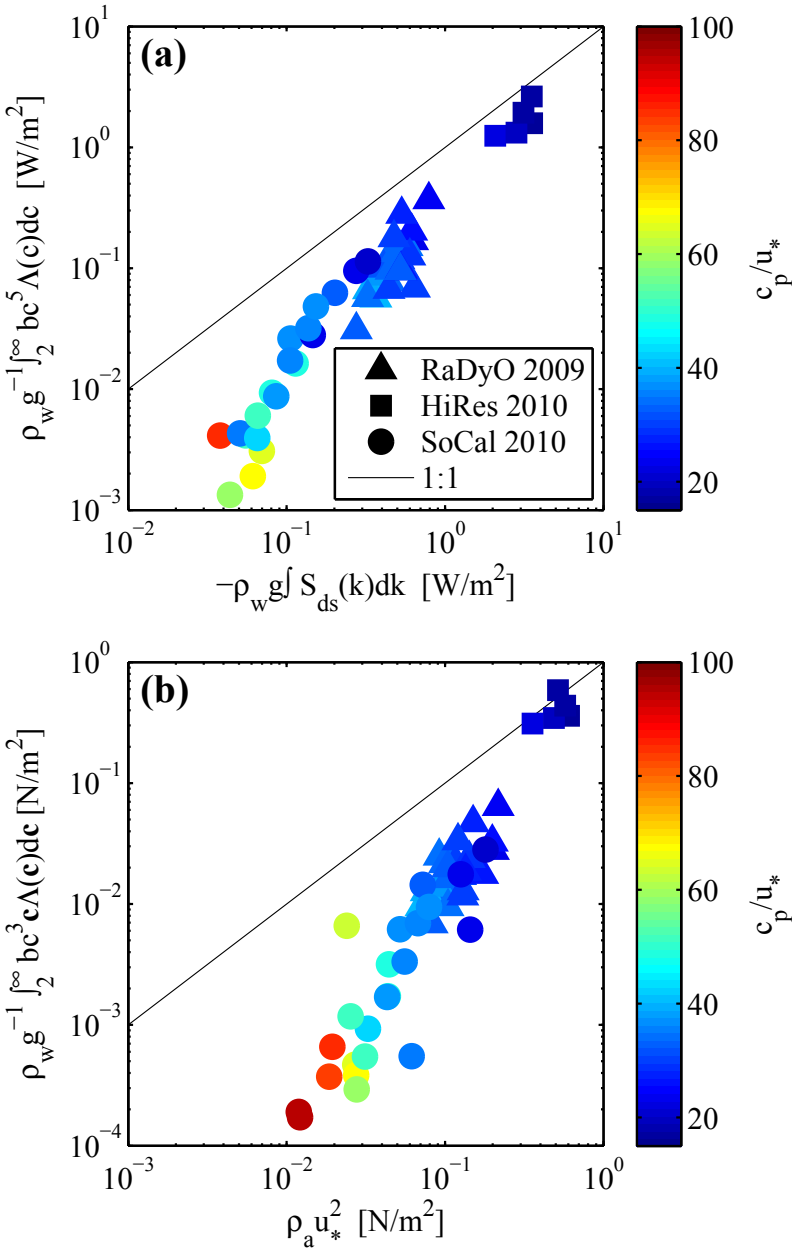

Figure 4.13: Dissipation and stress calculated using only $c > 2$ m/s for comparison with figure 4.11. This represents only air-entraining breakers and removes the effect of microbreaking. **(a)** Dissipation by breaking (ordinate) compared with modelled wave field dissipation (abscissa). **(b)** Momentum flux from waves to currents due to wave breaking (ordinate) plotted against wind stress (abscissa). Color corresponds to wave age and solid line indicates 1:1 correspondence.

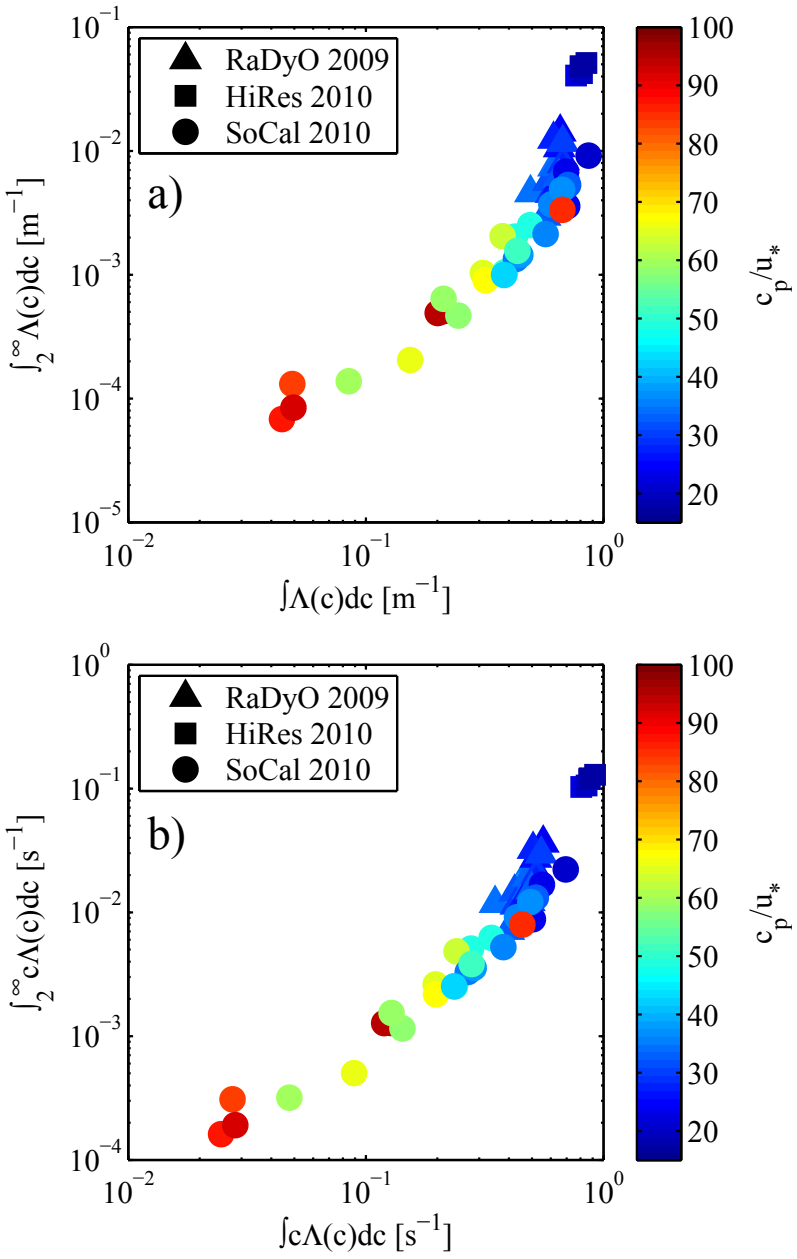

Figure 4.14: Effects of including microbreaking in the integration of a) $\Lambda(c)$, and b) the first moment of $\Lambda(c)$. The ordinate uses $c = 2$ m/s as the lower limit of integration whereas the abscissa uses the full range of c. Each point corresponds to a 20-minute average, and the coloring represents wave age.

Chapter 5

Measurements of surface and near-surface turbulence

5.1 Introduction

There is considerable evidence in the literature for increased turbulent kinetic energy (TKE) dissipation near the sea surface over that predicted by the "law of the wall" (*Kitaigorodskii et al.* 1983, *Gargett* 1989, *Agrawal et al.* 1992, *Anis and Moum* 1992, *Osborn et al.* 1992, *Terray et al.* 1996, *Drennan et al.* 1996, *Gemmrich* 2010). However, traditional measurements of dissipation, and turbulence in general, very near the surface of the ocean are notoriously difficult. Thus the structure of the turbulence very near the surface remains an outstanding question.

Early measurements were typically taken using microstructure probes. These could either be part of a free-falling profiler (*Osborn and Cox* 1972, *Dillon and Caldwell* 1980, *Moum et al.* 1995), or be mounted on ships (*Grant et al.* 1962), towed bodies (*Grant et al.* 1968a, *Nasmyth* 1970), or even submarines (*Grant et al.* 1968b, *Gargett et al.* 1984, *Osborn and Lueck* 1985). Microstructure probes are extremely sensitive shear and temperature probes that are sampled at very high temporal resolution. Thus they are useful for resolving the smallest scales of turbulence, down to and beyond the Kolmogorov scale for weak dissipation. That sensitivity and the associated tiny probe size makes them very susceptible

to contamination by small particles (i.e. plankton). The most significant problem with using microstructure probes to measure the turbulence associated with highly intermittent events like wave breaking, is their slow repeat time, resulting in significant undersampling. Microstructure probes apply Taylor's frozen turbulence hypothesis to time series of shear to calculate dissipation spectra and thus TKE dissipation. Two categories of motion make the use of Taylor's hypothesis challenging; probe motion and wave orbital motion. *Lumley and Terray* (1983) described an approximate technique to correct spectra of turbulence recorded in the presence of surface waves, but good measurements of the wave field are needed, adding another source of error. Probe motions can also be removed from the turbulence signal provided the motion and orientation of the probe is known - requiring a good motion package.

More recently acoustic doppler velocimeters (ADVs) (*Drennan et al.* 1996) (and similar optical instruments, *Agrawal and Belting* 1988) have been used to measure the velocity of small volumes of water remotely with reduced flow disturbance. This has the advantage over microstructure profilers of reducing the effect of flow distortion by the instrument. Typical sampling volumes $\mathcal{O}(1\text{cm}^3)$ are too large to allow these instruments to capture the smallest scales of turbulence, so dissipation is calculated by assuming homogeneous isotropic turbulence and fitting a $k^{-5/3}$ curve to the measured inertial subrange. ADVs also require the use of Taylor's hypothesis to convert temporal to spatial data, and so the associated problems noted above still apply. Although fixed single point measurements mounted near the surface can capture the temporal variations of turbulence associated with wave breaking, they do not capture the spatial structure.

More recently, pulse coherent acoustic doppler profilers (PCADP) have been used to investigate turbulence near the sea surface (*Lohrmann et al.* 1990, *Gargett* 1994, *Veron and Melville* 1999, *Gemmrich and Farmer* 2004, *Gemmrich* 2010). These instruments measure velocities spatially, with $\mathcal{O}(1\text{cm})$ bins along an $\mathcal{O}(1\text{m})$ beam, and therefore do not require the use of Taylor's hypothesis. As with ADVs, PCADPs do not typically have sufficient resolution to capture the smaller dissipative scales of turbulence, so dissipation must be calculated using an iner-

tial subrange fit, using either a $k^{-5/3}$ fit or related method of structure functions (*Wiles et al.* 2006). Since the measurement is spatial and can be repeated rapidly, PCADPs have two effective dimensions of sampling velocity (space and time), making them superior to single point measurements for capturing intermittency. PCADP measurements are more resistant to wave contamination than single point measurements; simple detrending filters out all motions with scales larger than the beam length. Since linear wave orbital velocities are proportional to e^{kz}, where k is the horizontal wavenumber and z is the vertical coordinate, the orbital velocities of waves short enough to contaminate the measurements decay very quickly with depth, making waves a concern only very near the surface. However, other difficulties with acoustic instruments near the surface include shadowing and scattering from bubble clouds and reflections from the sea surface.

An important consideration whenever any instrument that samples turbulence is deployed in a wavy environment is the great difficulty in ensuring that the instrument is not sampling it's own wake. The wave field in the open sea may have a broad directional distribution and so it is virtually impossible to ensure that the sampling volume is not sometimes "downstream" of the instrument itself. This interference can occur multiple times modulo a close approximation to the wave period, depending on the relative strength of the current and the Stokes drift versus the wave orbital velocity. Previous authors have typically avoided this difficulty by carefully selecting data at times when the mean velocity is sufficiently larger than the wave-orbital velocities (e.g. *Gerbi et al.* 2009). Unfortunately, this criterion is seldom met very near the sea surface.

The separation of waves and turbulence is a problem that permeates many areas of geophysical fluid dynamics, especially field measurements in physical oceanography and meteorology. Many methods depend on linear filtering techniques, but frequently, particularly at the sea surface, the scales of motion overlap to such a degree that filtering is not useful. At the sea surface, it is also common to assume all velocities that are coherent with fluctuations of the surface displacement are wave motion and the remainder is turbulence. However this eliminates the possibility of measuring wave-modulated turbulence.

In this work, a new technique for investigating turbulence at the surface of the ocean is presented. The surface velocity field, measured using stereo IR pattern imaging velocimetry reconstructions of the sea surface, was separated into irrotational and rotational components. The irrotational components were taken to be wave velocities, and the rotational velocities were taken to be turbulence. This allowed measurement of both types of motion over the same range of scales. An added advantage of this technique is that the instrumentation does not disrupt the flow field, so there are no concerns about measuring wakes.

On thing this new technique can not do is measure turbulence beneath the surface. For that we have used an array of PCADPs, which suffer from the same shortcomings described above.

5.2 Separation of waves from turbulence

Helmholtz's Theorem states that a vector field, in this case velocity $\boldsymbol{u}$, can be separated into irrotational, $\boldsymbol{u_I}$ (curl free), and rotational, $\boldsymbol{u_R}$ (divergence free), components

$$\boldsymbol{u} = \underbrace{-\nabla\phi}_{\boldsymbol{u_I}} + \underbrace{\nabla \times \boldsymbol{A}}_{\boldsymbol{u_R}}. \tag{5.1}$$

Noting that surface waves are generally assumed to be irrotational to first order, and that turbulence is by definition highly rotational, the rotational component of velocity is assumed to be representative of only turbulence, and not rotational surface waves. Statistics of rotational velocities, and thus turbulence, can be extracted either directly by performing a Helmholtz decomposition and studying $\boldsymbol{u_R}$, or indirectly by calculating the vorticity field, $\boldsymbol{\omega} = \nabla \times \boldsymbol{u}$, and studying its statistics. Both techniques will now be discussed.

5.2.1 Helmholtz decomposition

Separation of a bounded 2D velocity field into its irrotational and rotational components as in Equation 5.1 is dependent on boundary conditions. For this work, it is assumed that both vorticity and divergence of the surface velocity field

vanish at infinity. It is then possible, following *Corpetti et al.* (2003), to compute irrotational and rotational components of the velocity as

$$\boldsymbol{u_I} = \mathcal{F}^{-1}\left[\boldsymbol{k}\cdot\hat{\boldsymbol{u}}(\boldsymbol{k})\frac{\boldsymbol{k}}{\parallel \boldsymbol{k} \parallel^2}\right] \tag{5.2}$$

and

$$\boldsymbol{u_R} = \mathcal{F}^{-1}\left[\boldsymbol{k}^{\perp}\cdot\hat{\boldsymbol{u}}(\boldsymbol{k})\frac{\boldsymbol{k}^{\perp}}{\parallel \boldsymbol{k}^{\perp} \parallel^2}\right] \tag{5.3}$$

respectively. Here $\hat{\boldsymbol{u}}(\boldsymbol{k}) = \mathcal{F}[\boldsymbol{u}(\boldsymbol{x})]$ is the Fourier transform of $\boldsymbol{u}(\boldsymbol{x})$, $\mathcal{F}^{-1}$ indicates the inverse Fourier transform, $\boldsymbol{k} = (k_1, k_2)$ is the wavenumber, and $\boldsymbol{k}^{\perp} \equiv (-k_2, k_1)$. An alternative, mathematically equivalent, formulation is given in *Smith* (2008).

This decomposition was applied to the regridded surface horizontal velocity fields measured using the stereo IR PIV system. It was found that rotational velocity fields, $\boldsymbol{u_R}$, separated in this manner captured an average of 97% of the vorticity variance of the original velocity field; that is,

$$0.97 \sim \left\langle (\nabla \times \boldsymbol{u_R})^2 \right\rangle / \left\langle (\nabla \times \boldsymbol{u})^2 \right\rangle, \tag{5.4}$$

suggesting that the underlying assumptions were valid. The separated rotational velocity field, $\boldsymbol{u_R}$, was then assumed to be representative of turbulence for further analysis.

5.2.2 Surface vorticity

Since random vorticity is a fundamental measure of turbulence, it is also useful to study the vorticity field directly, without resorting to the Helmholtz decomposition. As outlined above, the end result of the stereo PIV processing is an irregularly spaced grid of points in 3D space with a 3 component velocity vector assigned to each point. Surface-normal and vertical vorticity were calculated and their results were compared.

Vertical vorticity (method of *Meyer et al.* 2001)

Vertical vorticity was calculated using the method given by *Meyer et al.* (2001), which allows calculation of gradients of unevenly spaced fields. They define

the function of interest, $S(\boldsymbol{p})$, at a point $\boldsymbol{p}$ surrounded by other points $\boldsymbol{p}_i$, where $i = 1..n$. Then the difference in S between points $\boldsymbol{p}_i$ and $\boldsymbol{p}$ is

$$\Delta S_i = S(\boldsymbol{p_i}) - S(\boldsymbol{p}) \tag{5.5}$$

and the vector difference between the points themselves is

$$\boldsymbol{r}_i = \boldsymbol{p}_j - \boldsymbol{p} = \hat{\boldsymbol{i}}\Delta x + \hat{\boldsymbol{j}}\Delta y, \tag{5.6}$$

where $\hat{\boldsymbol{i}}$ and $\hat{\boldsymbol{j}}$ are unit vectors in the x and y directions respectively. The unit vector in the direction of $\boldsymbol{r}_i$ is then

$$\hat{\boldsymbol{r}}_i = \frac{\boldsymbol{r}_i}{|\boldsymbol{r}_i|} = \hat{\boldsymbol{i}}\hat{r}_{x,i} + \hat{\boldsymbol{j}}\hat{r}_{y,i}, \tag{5.7}$$

and $r_i = |\boldsymbol{r_i}|$ is the scalar distance between $\boldsymbol{p}_i$ and $\boldsymbol{p}$. The gradients of S at point $\boldsymbol{p}$, $\partial S/\partial x$ and $\partial S/\partial y$, are then found via the system of linear equations

$$\begin{bmatrix} \Delta S_1/r_1 \\ \Delta S_2/r_2 \\ \vdots \\ \Delta S_n/r_n \end{bmatrix} = \begin{bmatrix} \hat{r}_{x,1} & \hat{r}_{y,1} \\ \hat{r}_{x,2} & \hat{r}_{y,2} \\ \vdots & \vdots \\ \hat{r}_{x,n} & \hat{r}_{y,n} \end{bmatrix} \cdot \begin{bmatrix} \partial S/\partial x \\ \partial S/\partial y \end{bmatrix} \tag{5.8}$$

$$\sigma \quad = \quad \mathbf{R} \quad \cdot \quad \boldsymbol{g}$$

which can be solved for $\boldsymbol{g}$ to get

$$\begin{bmatrix} \partial S/\partial x \\ \partial S/\partial y \end{bmatrix} = \boldsymbol{g} = (\mathbf{R}^\top\mathbf{R})^{-1}\mathbf{R}^\top\sigma. \tag{5.9}$$

In this analysis, only the 8 points on the pseudo grid directly surrounding each $\boldsymbol{p}$ were used in calculating gradients. Gradients of velocity, $u(\boldsymbol{p})$ and $v(\boldsymbol{p})$, were calculated at every point $\boldsymbol{p}$ on the reconstructed surface (by substituting velocity fields in the place of $S(\boldsymbol{p})$ in the above). Vertical vorticity was then defined as

$$\omega_3(\boldsymbol{p}) = \left.\frac{\partial v}{\partial x}\right|_{\boldsymbol{p}} - \left.\frac{\partial u}{\partial y}\right|_{\boldsymbol{p}}. \tag{5.10}$$

Figure 3.2 shows examples of surface reconstructions with their corresponding velocity fields. Figure 3.3 shows the corresponding vorticity fields. Velocity resolution

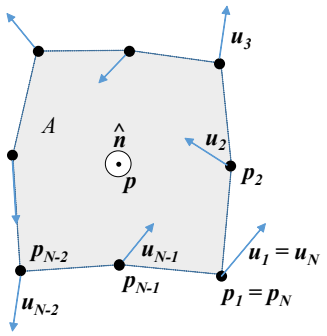

Figure 5.1: Schematic of uneven points used in vorticity calculation.

is 1/8 the image resolution (based on the cross correlation window size described in chapter 3, and the resolution of gradients and vorticity is 1/3 of the velocity resolution.

Surface-normal vorticity (circulation method)

The vorticity directed in the local normal direction was calculated by measuring the circulation around a point and then using Stokes' theorem to relate that to vorticity. For a closed loop, the vorticity flux through that loop is equal to the circulation around that loop. For a discrete set of N points on a closed loop, defined such that $\boldsymbol{p_1} = \boldsymbol{p_N}$, with associated velocities $\boldsymbol{u_i}$, and (shown schematically in figure 5.1), the circulation can be approximated as

$$\Gamma = \sum_{i=1}^{N-1} \left(\frac{\boldsymbol{u_i} + \boldsymbol{u_{i+1}}}{2} \right) \cdot (\boldsymbol{p_{i+1}} - \boldsymbol{p_i}) \,. \tag{5.11}$$

A plane with normal vector $\hat{\boldsymbol{n}}$ was then fit to those points. The surface area, A, contained by the projection of those points onto that plane, was then used to calculate vorticity

$$\boldsymbol{\omega}(\boldsymbol{p}) = \frac{\Gamma}{A} \hat{\boldsymbol{n}} \tag{5.12}$$

This vorticity calculation was performed for every point on each reconstructed velocity field. As with the vertical vorticity calculation, the surface-normal vorticity has a resolution of 1/3 of the velocity resolution.

Vorticity spectra

Vorticity fields were regridded using the same 2 cm grid used for velocity, as described in chapter 3. Directional wavenumber spectra of vertical vorticity were then calculated. Figure 5.2 shows 3 examples of such spectra. Particularly notable is the "lobed" structure, orthogonal to the direction of wave propagation in panel (a) and nearly aligned with wind/wave propagation in (b). When orthogonal to the wind/wave direction, this structure was found by *Veron et al.* (2009) to be consistent with the presence of wind rows, small features similar to Langmuir circulations. Spectra indicating such streaks were not, however, universally found; any small-scale streaking in example spectrum (b) would be nearly cross-wind.

The directionality in the spectra is defined as

$$\gamma_D = \frac{\phi_{\omega_3}(k_{max}, \theta_{max})}{\frac{1}{2\pi k_{max}} \int_0^{2\pi} \phi_{\omega_3}(k_{max}, \theta) d\theta} - 1, \tag{5.13}$$

where k_{max} and θ_{max} are the wavenumber and azimuth of the spectral peak found in the 2D vorticity spectra, $\phi_{\omega_3}(k, \theta)$. In these experiments, γ_D was low, with an average value during RaDyO 2009 of $\gamma_D = 0.08$ and during SoCal 2010 of $\gamma_D = 0.23$.

A comparison of the two methods (the *Meyer et al.* (2001) method vs. the circulation method) for calculating vorticity is shown in figure 5.3. The difference between surface-normal vorticity and the vertical component of surface-normal vorticity for these measurements is minimal. The spectra for both types of vorticity exhibit the same basic slightly lobed structure, with the vorticity variance approximately 2.3% lower for the vertical vorticity than the surface normal vorticity. More significant is the difference between vorticity calculated using the method of *Meyer et al.* (2001) versus the circulation method. While retaining the same spectral form, *Meyer et al.* (2001) vorticity has approximately 22% higher variance than the circulation vorticity. The effects of these differences on the calculation of TKE dissipaiton are discussed in section 5.4.

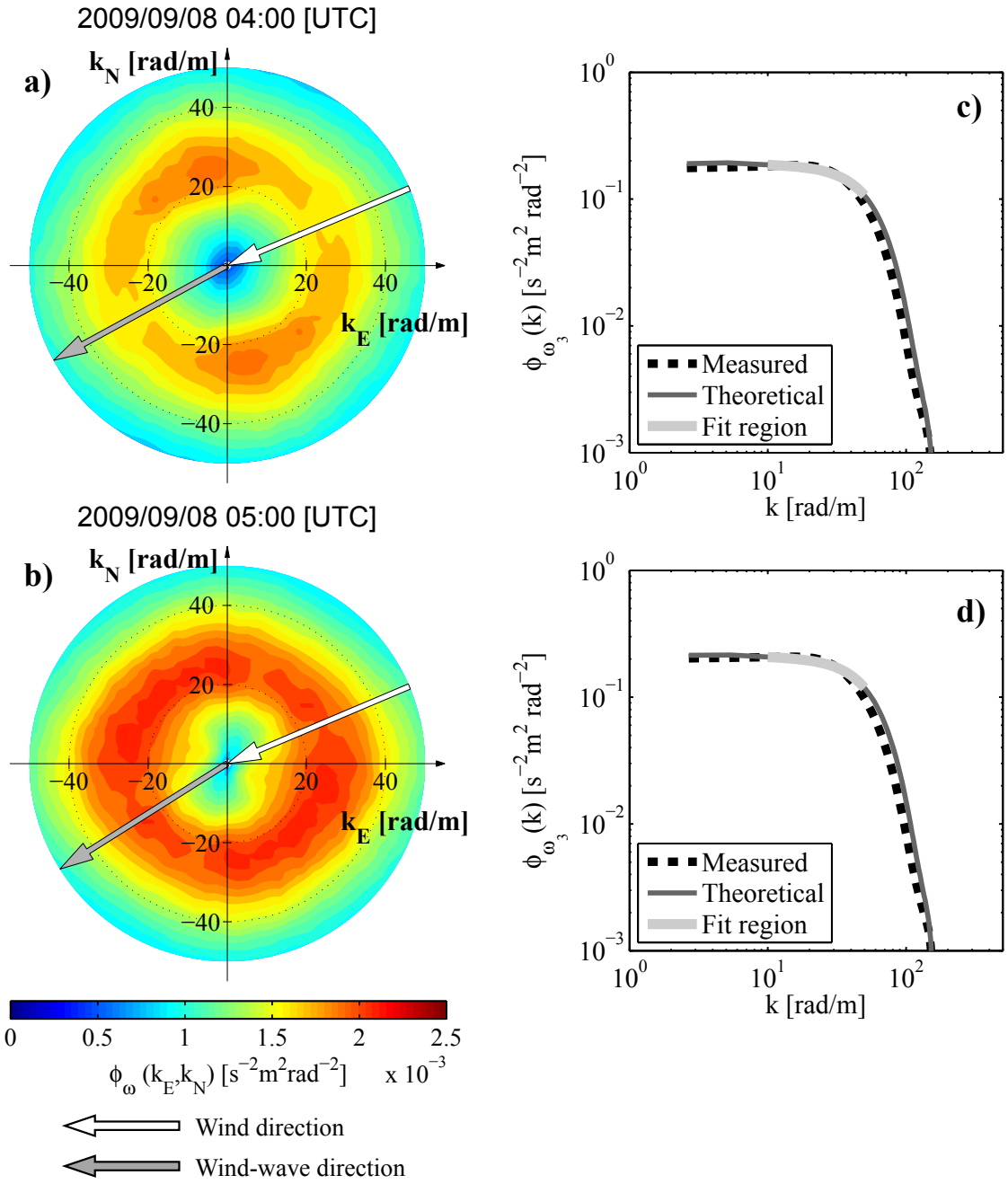

Figure 5.2: 20-minute average spectra of vertical vorticity taken during RaDyO 2009. *Left:* Directional wavenumber spectra, $S_{\omega_3\omega_3}(k_x, k_y)$. White arrows indicate mean wind direction and gray arrows indicate direction of wind-wave spectral peak. *Right:* Average measured 1D directional spectra (dashed black lines), theoretical spectra including resolution roll-off, $S_{MOD}(\epsilon; k_1)$ (solid dark gray lines), and $S_{MOD}(\epsilon; k_1)$ in fitted range (solid light gray lines).

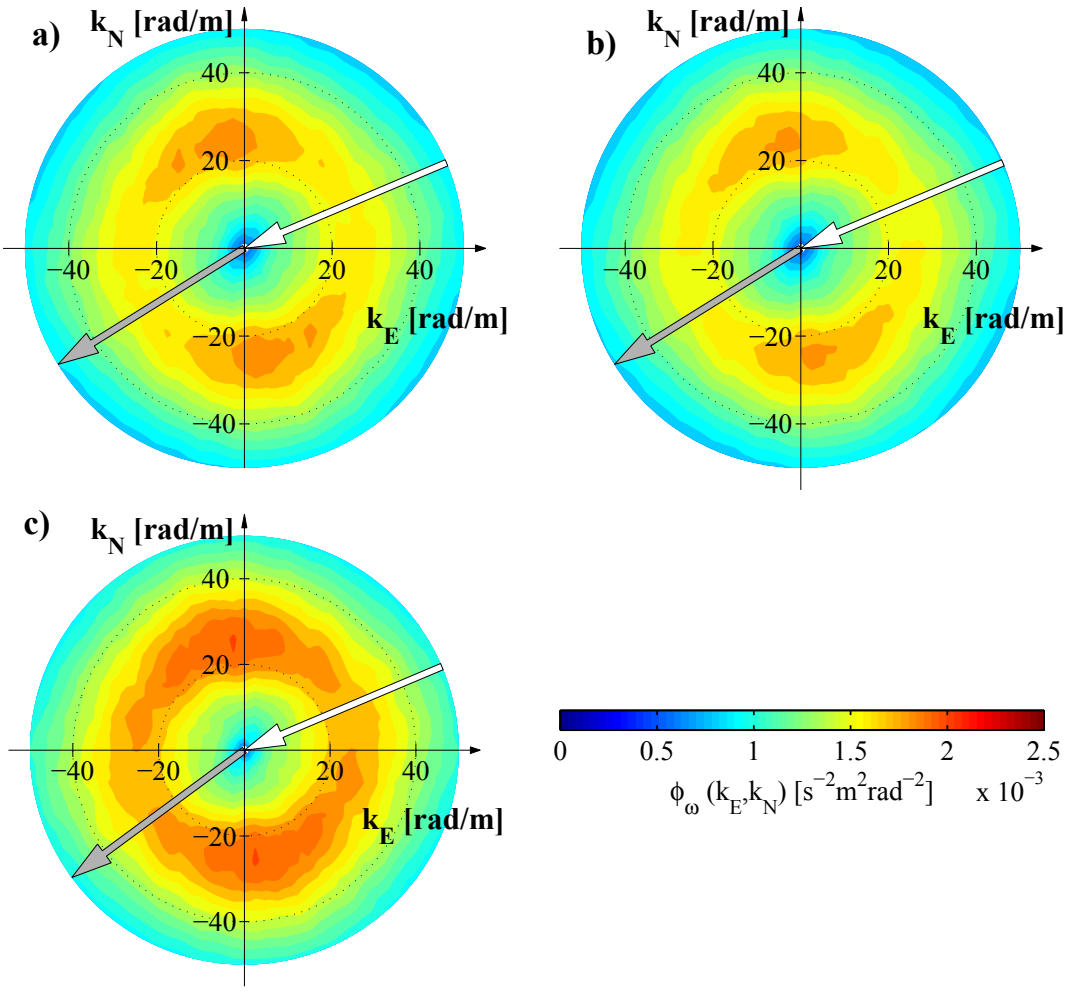

Figure 5.3: Comparison of vorticity spectra using different methods for calculating vorticity. Spectra are 20-minute averages and are of a) surface-normal vorticity from the circulation technique b) vertical component of surface-normal vorticity c) the technique of *Meyer et al.* (2001). The corresponding 1D vorticity spectra are shown in figure 5.4. The sampling period started at 2009/09/08 03:00 [UTC].

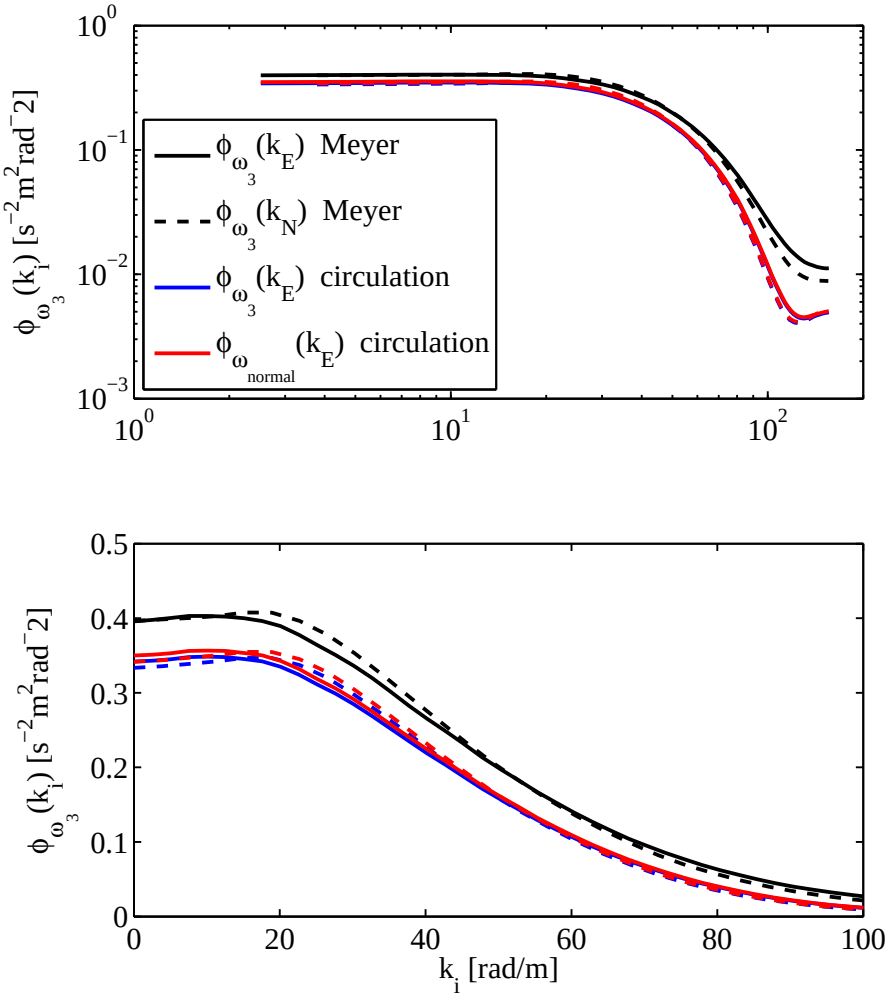

Figure 5.4: Comparison of 1D vorticity spectra using different methods for calculating vorticity in logarithmic (top) and linear (bottom) coordinates. Spectra are 20-minute averages for the period starting at 2009/09/08 03:00 [UTC]. Black curves are from the technique of *Meyer et al.* (2001), red curves are surface-normal vorticity from the circulation technique, blue curves are the vertical component of surface-normal vorticity. Solid lines are spectra in the east direction and dashed are north. The corresponding 2D spectra are shown in figure 5.3.

5.3 Surface TKE Dissipation

A major motivation for this work has been to measure TKE dissipation at the sea surface. TKE dissipation is defined by $\epsilon \equiv 2\nu \langle s_{ij} s_{ij} \rangle$ (where $s_{ij} \equiv 1/2\,(\partial u_i/\partial x_j + \partial u_j/\partial x_i)$ is the rate of strain tensor), which at high Reynolds numbers can be approximated as $\epsilon \cong \nu \langle \omega_i \omega_i \rangle$ (*Tennekes and Lumley* 1972). This provides a means of accessing dissipation directly from the vorticity or velocity fields, but requires the resolution of the Kolmogorov microscale, which is smaller than the PIV resolution available in these field measurements.

5.3.1 Inertial subrange fit

The classic technique for calculating dissipation when the smallest scales are not resolved is to fit data to the Kolmogorov inertial subrange (ISR). Assuming homogeneous, isotropic turbulence, and that the scales observed are larger than the scale of dissipation (Kolmogorov scale) but smaller than the scale of energy input (outer scale), one-dimensional energy spectra have the form

$$E_{11}(k_1) = \frac{18}{55} C \epsilon^{2/3} k_1^{-5/3}, \tag{5.14}$$

and similarly

$$E_{22}(k_1) = \frac{24}{55} C \epsilon^{2/3} k_1^{-5/3}. \tag{5.15}$$

The level of these spectra only depends on the TKE dissipation rate, ϵ, and a universal constant, C, which has been experimentally determined to be $C = 1.5$ (*Grant et al.* 1962, *Pope* 2000, §6.5). A detailed treatment of the spectra of turbulence is included in appendix B.

In order to exclude irrotational wave energy, the rotational components, $\boldsymbol{u_R}$, of gridded surface velocity were used. Surface velocity was separated into east (x) and north (y) components, u and v respectively. For each frozen image of surface velocity, along and cross-velocity spectra were taken for both east and north components of velocity. These spectra were then inserted into Equations 5.14 and 5.15, and the equations were solved for the dissipation, ϵ. This spectral fitting occurred over a wavenumber range $10 \leq k \leq 60$ rad/m. In isotropic turbulence, the

direction chosen for k_1 does not matter, and, indeed, 20-minute average dissipation values calculated using either Equation 5.14 or 5.15 and with k_1 oriented either in the east or north direction were all typically within 10%.

5.3.2 Vorticity spectrum fit

In this work, a second technique for measuring surface dissipation based on the vorticity field has been developed. This technique removes the effects of irrotational velocities but does not require a Helmholtz decomposition of the surface velocity or resolution of the Kolmogorov microscale. The data processing scheme is discussed in detail below, but in summary it consists of calculating the vorticity spectrum of the data, calculating a theoretical vorticity spectrum based on dissipation ϵ, subjecting that to gridding effects, and then varying ϵ to minimize the difference between the theoretical spectrum and the measured spectrum.

In a process somewhat analogous to $k^{-5/3}$ slope fitting described above, it is possible to use the universal form of the vorticity spectrum to estimate dissipation. *Antonia et al.* (1988) showed that, in homogeneous isotropic turbulence, the two-dimensional horizontal wavenumber spectrum of vertical vorticity can be written

$$\phi_{\omega_3}(k_1, k_2) = \int_{-\infty}^{\infty} \frac{E(k)}{4\pi} \left(1 - \frac{k_3^2}{k^2}\right) dk_3, \tag{5.16}$$

and the one-dimensional spectrum of vertical vorticity in the horizontal direction can be written as,

$$\phi_{\omega_3}(k_1) = \iint_{-\infty}^{\infty} \frac{E(k)}{4\pi} \left(1 - \frac{k_3^2}{k^2}\right) dk_2 dk_3, \tag{5.17}$$

(c.f. equations B.29 and B.32, respectively). Here k_1 and k_2 are the wavenumbers in orthogonal horizontal directions, $k = |\boldsymbol{k}|$ where $\boldsymbol{k}$ is the three-dimensional wavenumber, and $E(k)$ is the energy spectrum function. A classical form for the energy spectrum function is given in *Pope* (2000) pp. 232.,

$$E(k) = C\epsilon^{2/3} k^{-5/3} f_L(kL) f_\eta(k\eta), \tag{5.18}$$

where the roll-off at the Kolmogorov scale follows the form

$$f_\eta(k\eta) = \exp\left[-\beta\left(((k\eta)^4 + c_\eta^4)^{1/4} - c_\eta\right)\right]. \tag{5.19}$$

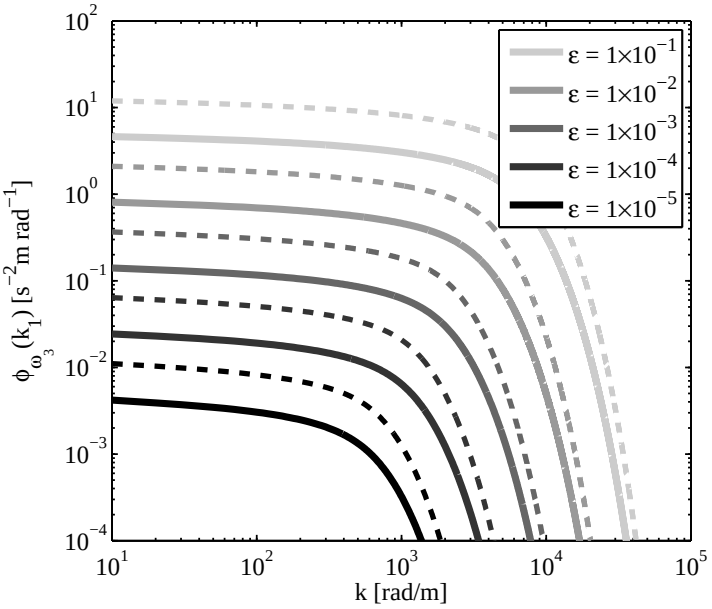

Figure 5.5: Theoretical vorticity spectra for 3D (—) and 2D (− −) isotropic turbulence with an energy spectrum of the form given in Equation 5.18. Shading indicates dissipation in units of $[m^2s^{-3}]$.

In this work, it was assumed that the outer scale of turbulence, L, was much larger than the camera field of view, $kL >> 1$, so $f_L(kL)$ was set equal to unity. The value for the constant $\beta = 5.2$ is taken from the literature, for example *Saddoughi and Veeravalli* (1994), and the constant $c_\eta \approx 0.4$ is determined by requiring $\epsilon = \int_0^\infty 2\nu k^2 E(k) dk$.

Numerical solutions for the form of vertical vorticity spectra given in Equation 5.17, using the energy spectrum from Equation 5.18, are plotted in Figure 5.5 for various dissipation levels. These theoretical spectra depend on the behavior of the energy spectrum at wavenumbers higher than this experiment was able to resolve. The resolution-limited spectra shown in Figure 5.2 show a roll-off at approximately 30 rad/m, well before the Kolmogorov scale.

The effects of gridding the data have been simulated by applying random white noise to the raw 3D velocity locations that resulted from the stereo PIV analysis. This white noise was assumed to represent a random velocity field and was then re-gridded and used to calculate vorticity following the same technique as

for the actual measured velocity field. The 2D spectrum of this regridded random vorticity field, $S_{WHT}(k_1, k_2)$, was then scaled so that it reached a maximum value of unity, and was then taken to represent the spectral roll-off due to regridding

$$S_{roll}(k_1, k_2) = \frac{S_{WHT}(k_1, k_2)}{\max\left(S_{WHT}(k_1, k_2)\right)}. \tag{5.20}$$

Multiplying the theoretical spectrum, $\phi_{\omega_3}(k_1, k_2)$, from equation 5.16, subject to equation 5.18, by the scaled 2D spectrum of white noise gave the final modeled vorticity spectrum for any given dissipation value,

$$S_{MOD}(\epsilon; k_1, k_2) = S_{roll}(k_1, k_2) \int_{-\infty}^{\infty} \frac{C\epsilon^{2/3} k^{-5/3} f_\eta(k\eta)}{4\pi} \left(1 - \frac{k_3^2}{k^2}\right) dk_3. \tag{5.21}$$

Dissipation was then varied to minimize the difference (via a least squares cost function) between $S_{MOD}(\epsilon; k_1, k_2)$ and the measured spectrum. Examples of one-dimensional measured vorticity spectra are shown as black dashed lines in figure 5.2, panels d), e), and f). The corresponding 1D fit spectra,

$$S_{MOD}(\epsilon; k_1) = \int_{-\infty}^{\infty} S_{MOD}(\epsilon; k_1, k_2) dk_2, \tag{5.22}$$

are shown as the solid gray curves, and the wavenumber range of that fitting, $10 < k < 50$, is highlighted in light gray. The fitting range was designed to capture the peaks of the vorticity spectra without extending to scales larger than were reliably captured in the re-gridded vorticity data or extending to scales smaller than the velocity resolution.

5.3.3 Inertial scaling

Given the uncertainty of the existence of isotropic fields at the surface, it is useful to have an independent check on the such methods for calculating ϵ. The inertial, or large eddy, technique does not require an assumption of isotropy. *Taylor* (1935) noted that, at sufficiently high Reynolds numbers, ϵ is independent of viscosity and must be proportional to

$$\epsilon \sim \frac{U'^3}{L}, \tag{5.23}$$

where L is the characteristic length scale and U' is the characteristic velocity scale (see also *Tennekes and Lumley* 1972, §1.5). *Gargett* (1999) found the constant of proportionality to be approximately equal to unity, within a factor of 2, when comparing large eddy estimates with direct measurements of dissipation. This inertial scaling has also been used with some success to scale surface wave energy dissipation (*Drazen et al.* 2008, *Romero et al.* 2012). In this work, the root mean squared rotational velocity, $\sqrt{\langle u_R'^2 \rangle}$, was used to define U', and the integral length scale of autocorrelation function of rotational velocity was used to define L; both being measured at the surface.

5.3.4 Comparison of methods

The three techniques described above for measuring surface dissipation were found to be consistent. Figure 5.6 shows a comparison of the 20-minute average dissipation calculated using the three methods. Dissipation calculated using the inertial subrange fit is an average of 12% lower than that calculated using the vorticity spectrum technique. The large-eddy technique produces dissipation values an average of 6% lower than the vorticity spectrum technique, but with considerable scatter. However, it should be noted that the large-eddy technique is biased high, relative to the vorticity spectrum fit technique, for data taken during the SoCal 2010 experiment and biased low for the RaDyO 2009 experiment. One potential explanation for this bias is that the field of view was larger for the RaDyO experiment than it was during the SoCal 2010 experiment, allowing the RaDyO experiment to find larger L values.

Each of the three methods uses a different set of assumptions. Both the inertial subrange fit and the vorticity spectral fit technique assume the presence of homogeneous isotropic turbulence. However, application of the inertial subrange fit method also relies on the Helmholtz decomposition described in section 5.2.1, which assumes that vorticity and divergence of the velocity field vanish at infinity. The inertial scaling technique does not require isotropy, but does assume that the length scale L is far larger than the dissipative scales. The relative agreement between the three methods, over more than an order of magnitude of dissipation

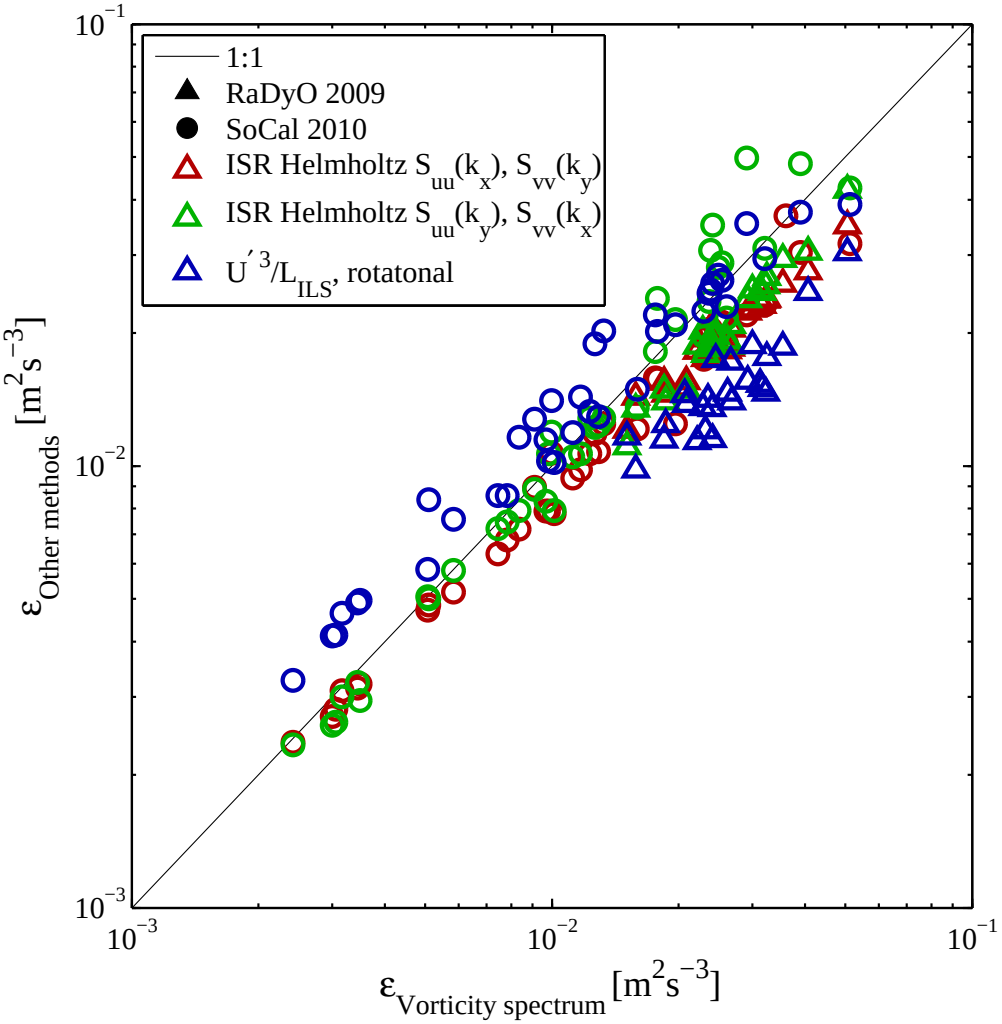

Figure 5.6: Comparison of techniques for calculating dissipation, ϵ, at the surface. Each symbol corresponds to a 20-minute average. The abscissa is dissipation calculated using the vorticity spectral fit method. Red and green symbols are for the values on the ordinate calculated using Equations 5.14 and 5.15 respectively (using the rotational velocity component). Blue symbols are for the values calculated using the inertial (large eddy) method. Triangles are data collected during RaDyO 2009, and circles are data from the SoCal 2010 experiment.

range, lends credibility to the calculations.

5.4 Sources of error

The assumption of isotropy is a questionable one in the case of near-surface turbulence. Numerical work has shown a suppression of vertical turbulent velocity variance near a free surface (for example, *Shen and Yue* (2001)). A similar behavior has been observed in highly stratified atmospheric flows (*Lindborg* 2007). The limiting case of suppression of vertical velocities is two dimensionality. Appendix B.4.2 includes the derivation of an equation analogous to Equation 5.17 for the case of 2D turbulence,

$$\phi_{\omega_3}(k_1) = \frac{2}{\pi}\int_0^\infty kE(k)dk_2 = \frac{2}{\pi}\int_{k_1}^\infty \frac{k^2E(k)}{(k^2-k_1^2)^{1/2}}dk. \tag{5.24}$$

Figure 5.5 also includes solutions of Equation 5.24, showing considerable similarity between the vorticity spectra for 2D and 3D turbulence. Assuming 3-D isotropic turbulence and using the vorticity spectrum technique for estimating dissipation will over-estimate, by approximately a factor of 2, the TKE dissipation rate if the turbulence is two dimensional. Thus the measurements as presented here could be considered to be an upper limit on the TKE dissipation at the sea surface.

As seen in figure 5.3, the method used for the vorticity calculation has a significant effect on the spectral level (though not, apparently, the qualitative shape). The (*Meyer et al.* 2001) technique produced a vorticity field with 22% more variance than the circulation technique. This corresponded to a 24% increase in measured TKE dissipation. The $\epsilon_{\text{vorticity spectrum}}$ plotted in figure 5.6 was based on the (*Meyer et al.* 2001) technique. Depending on which method is a superior approximation, this could imply that that surface dissipation has been over estimated by 24%. The dissipation calculated using the inertial subrange (fit to the energy spectrum of rotational velocities) was between these two estimates, on average 12% lower than that based on the (*Meyer et al.* 2001) technique. Unless otherwise specified, all following analysis uses surface dissipation calculated using the inertial subrange method.

Another concern is the observation that 2D wavenumber spectra of vorticity show a "lobed" structure, indicating a departure from horizontal isotropy assumed in Equation 5.18. This departure from isotropy in the spectra was typically $\gamma_D < 0.25$, and has been neglected.

Finally, it should be noted that due to the kinematic boundary condition at the surface, the velocity of air at the surface matches that of the water.

5.5 Subsurface turbulence

These experiments included instrumentation for measuring sub-surface turbulence. Although, as described in the introduction, there are significant challenges associated with measuring turbulence directly beneath a wavy surface, an attempt was made.

As described in Section 2, the topmost instrument was an pulse-coherent acoustic doppler profiler (Nortek 2MHz Aquadopp HR profiler) mounted on a surface-following float pointing upwards. Although not directly co-located with the field of view of the stereo IR cameras (it typically drifted ∼10m down wind), by assuming statistical homogeneity over the separation scale, comparisons can be still made. Instrumentation also included up to 3 lowered turbulence measurement instruments (LTMI). The uppermost LTMI was held at a fixed depth and located at the end of one of FLIP's booms (approximately 16m from FLIP's hull), directly beneath the IR cameras' fields of view. The lower two LTMIs were mounted inboard along the same boom at approximately 10.5 m from FLIP's hull and their depth was changed every 10 or 20 minutes.

Subsurface dissipation was calculated using the method of structure functions proposed by (*Wiles et al.* 2006) as implemented by *Gemmrich* (2010). A "centered" structure function can be defined

$$D(x,r) = \left\langle (u'(x+r/2) - u'(x-r/2))^2 \right\rangle, \tag{5.25}$$

where $u'(x)$ is the fluctuating velocity in the positive x direction and r is the separation of measurements. *Kolmogorov* (1941) showed that, at scales much larger

than the scale of dissipation, the structure function can be written in terms of dissipation

$$D(z,r) = C_v^2 \epsilon^{2/3} r^{2/3}. \tag{5.26}$$

Here $C_v^2 = 2.1$ is a universal constant. Equation 5.26 is the direct spatial analog of the better-known $k^{-5/3}$ inertial subrange wavenumber spectrum (Equation B.16). *Wiles et al.* (2006) fit to the measured structure function, a curve of the form

$$D(z,r) = N + Ar^{2/3}, \tag{5.27}$$

where $A = C_v^2 \epsilon^{2/3}$, $N = 2\sigma_N^2$, and σ_N is the standard deviation of the noise in the system.

Assuming that $N \ll Ar^{2/3}$ as in (*Gemmrich* 2010), then gives the relation

$$\epsilon \approx \left(\frac{A}{C_v^2} \right)^{3/2}, \tag{5.28}$$

which can be considered to be an upper bound on dissipation.

In these experiments, dissipation was calculated by the method of structure functions using along-beam velocities for each of the three Aquadopp beams. Processing steps were as follows:

1. The velocity ambiguity of an Aquadopp, v_a, is relatively low due to the physical constrains of pulse-coherent processing (*Lacy and Sherwood* 2004). Depending on the exact instrument configuration used, for these experiments it ranged between $v_a = \pm 0.13$ m/s to $v_a \pm 0.20$ m/s. Thus phase-wrapping of velocities were not uncommon, particularly in the energetic near-surface region. For each acoustic ping, the velocity difference between bins i and $i+1$, δu_i, was calculated. Whenever $\delta u_i > v_a$ ($\delta u_i < v_a$), the velocities at bins $i+1$ to N were reduced (increased) by $2v_a$.

2. A minimum pulse-coherent correlation threshold was used to remove spurious velocities. That threshold was

$$C_{thresh} = 100 \times \left(0.3 + 0.4\sqrt{s_f / s_{max}} \right), \tag{5.29}$$

as proposed by *Elgar et al.* (2005), where s_f is the sampling frequency and $s_{max} = 8$ is the maximum sampling frequency of the instrument. Each velocity bin with a corresponding correlation lower than C_{thresh} was discarded.

3. For the vertical beams, velocity bin locations were transformed into surface-relative coordinates prior to structure function calculation. The surface elevation, $\eta(t)$, was taken from the stereo IR surface reconstruction at a location directly above the near-surface (fixed depth) LTMI. The surface-relative location of a sampling-volume with a depth relative to the mean-surface of $z_{sv}(t)$ was then taken to be $\zeta_{sv}(t) = z_{sv}(t) - \eta(t)$. For the fixed-depth LTMI, this was checked by tracking the strong surface reflection seen in the Aquadopp's backscatter amplitude data (c.f. *Gemmrich* 2010).

4. Structure functions were calculated at each velocity bin. The range of scales over which the structure functions were calculated was $2\delta x \leq r \leq r_{max}$, where δx is the velocity bin size, and $r_{max} = 0.24$m. This value for r_{max} is consistent with *Gemmrich* (2010), and is a scale typically smaller than the surface velocity integral length scale, L (Section 5.35.3.3). Locations where the full structure function could not be calculated, for example within a distance r_{max} of the surface in vertical beams (or within a distance r_{max} of a beam end in the horizontal beams), were discarded.

5. At each depth bin, structure functions were averaged over 5 consecutive pings (2.5 s). These averaged structure functions were then applied to Equations 5.27 and 5.28 to calculated dissipation at each bin.

The final results of this processing are records of dissipation with a spatial resolution of $r_{max} = 0.24$ m, and a temporal resolution of 2.5 s. Figure 5.7 shows example timeseries of dissipation calculated using the uppermost Aquadopp. An example dissipation profile from the LTMI array, using the same near-surface data as in figure 5.7, is shown in Figure 5.8. In this case the average dissipation values are roughly monotonic with depth, but the spread of data exceeds two orders of magnitude.

As noted in the introduction to this chapter, accidental capture of turbulent wakes is always a concern when making measurements of this kind. Several steps were taken to minimize wake effects.

First, in order to avoid sampling the wake of FLIP's hull, mean currents were checked for each sampling period. Figure 5.9 shows the mean orientation

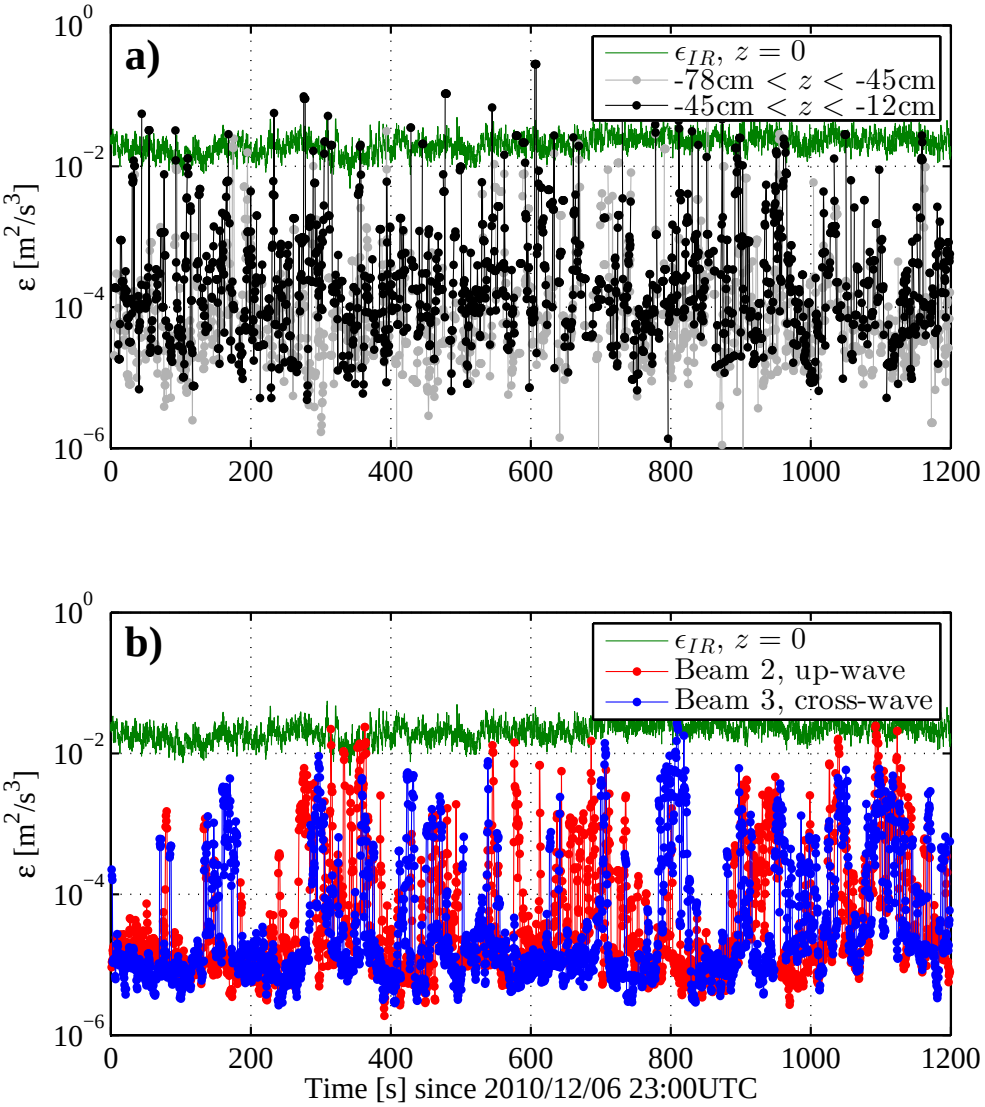

Figure 5.7: Near-surface TKE dissipation. Data in green are from the stereo IR PIV measurements. a) shows dissipation measured using the vertical beam of the near-surface Aquadopp, averaged between 12 and 45 cm from the instantaneous surface (black) and between 45 and 72 cm from the surface (gray). b) shows dissipation measured using the horizontal beams in the up-wave (red) and across-wave (blue) directions. The mean depth of the horizontal beams was 1.05 m and the section of each horizontal beam used for dissipation calculation was a distance of 0.5 m to 1.2 m from the instrument head.

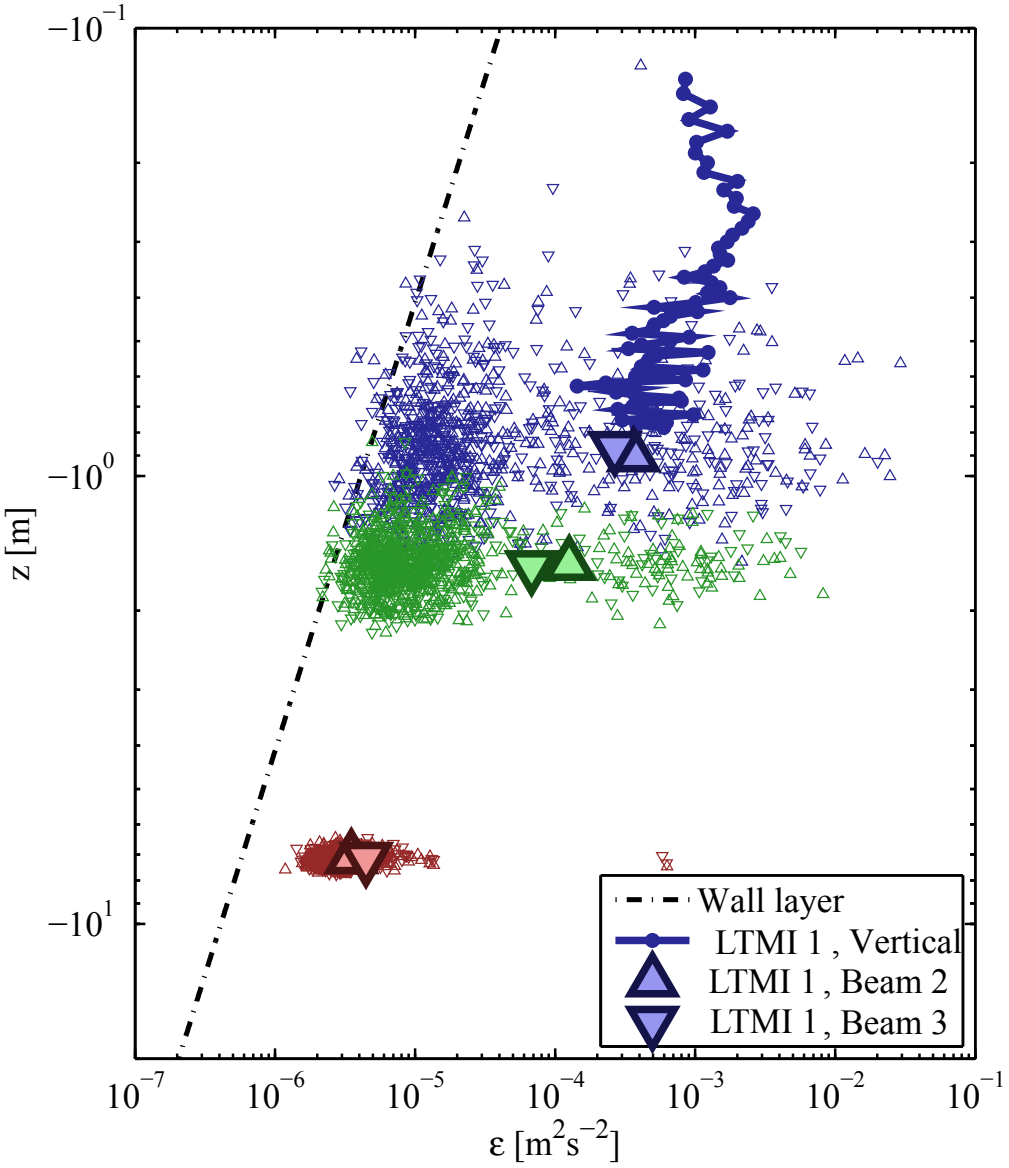

Figure 5.8: Subsurface dissipation measured by LTMI array over 20-minutes starting 2010/12/06 23:00 [UTC], compared against a wall layer (dash-dot line). Triangles are measurements from the horizontal beams of the LTMIs; upward triangles are from the up-current beam (beam 2), downward triangles are from the cross-current beam (beam 3). Colors correspond to LTMI number; 1, blue; 2, green; 3 red. Small triangles correspond to (overlapping) 2.5 s averages. All depths are relative to the instantaneous surface.

of FLIP and the LTMIs during an example 20-minute period. The dashed lines outline wedges potentially in the wake of FLIP at each depth level. The center axis of each wedge is aligned with the mean current at that depth. The angle of the wedge is set to $\theta_{wedge} = \theta_{min} + \theta_{rr}$, where θ_{rr} is the maximum range through which FLIP's heading rotated during the 20-minutes of sampling, and $\theta_{min} = 20°$. Any time the location of one of the profilers fell within the wake wedge, it was removed from processing. The same "wedge check" was performed for the wakes emanating from the LTMIs themselves (i.e. to check when LTMI2 was in the wake of LTMI1). During the SoCal 2010 experiment, this resulted in the removal of 8 out of 39 records for LTMI1, 15 out of 39 for LTMI2, and 18 out of 39 for LTMI3. Due to more steady conditions, no record removal was required during RaDyO 2009.

The ellipses in figure 5.9 show that the standard deviations of velocities were much higher than the mean velocities, particularly for the near-surface LTMI1. This was typical during the SoCal 2010 experiment, and means that instrument wake can be expected to be re-advected through at least part of the sample volume (see appendix C). Since the Aquadopp has an approximately 1m beam length, and only 24cm were needed to to compute dissipation, it was possible to utilize only the outer portion of the beam for computing dissipation.

Figure 5.11 shows all 20-minute average sub-surface dissipation measurements taken during the SoCal 2010 experiment.

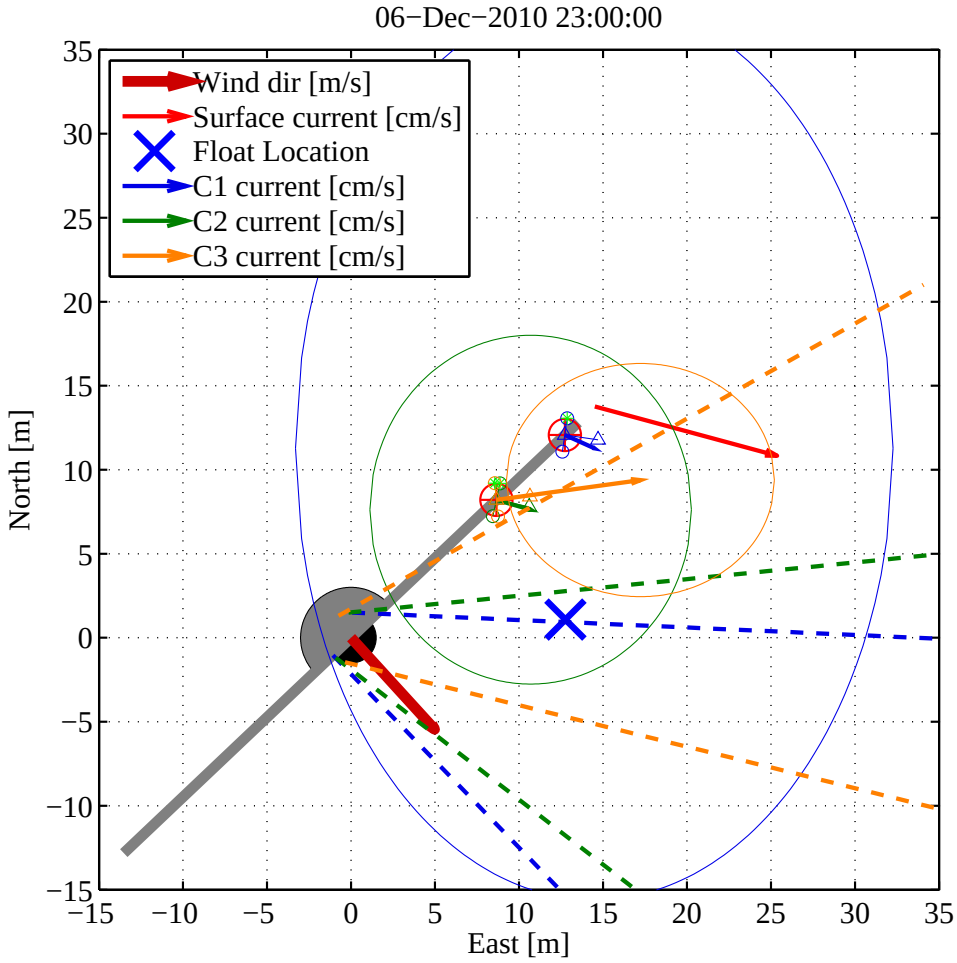

Figure 5.9: Plan view of FLIP and subsurface profilers for the 20-minute period starting 2010/12/06 23:00 [UTC]. Scale is meters for spatial measurements, m/s for wind velocity, and cm/s for current velocities. The gray region is the superstructure and booms, the black circle (half obscured) is the sub-surface hull of FLIP. The thick red arrow is the wind direction, thin arrows are current directions. Ellipses, centered at those arrow tips, indicate the standard deviation of velocity at profiler (again, in cm/s). Color corresponds to LTMI, blue is the near-surface fixed depth LTMI, green is the upper of the two profiling LTMIs, and orange is the lower profiling LTMI. The dashed lines outline wedges of potential wake from FLIP's hull.

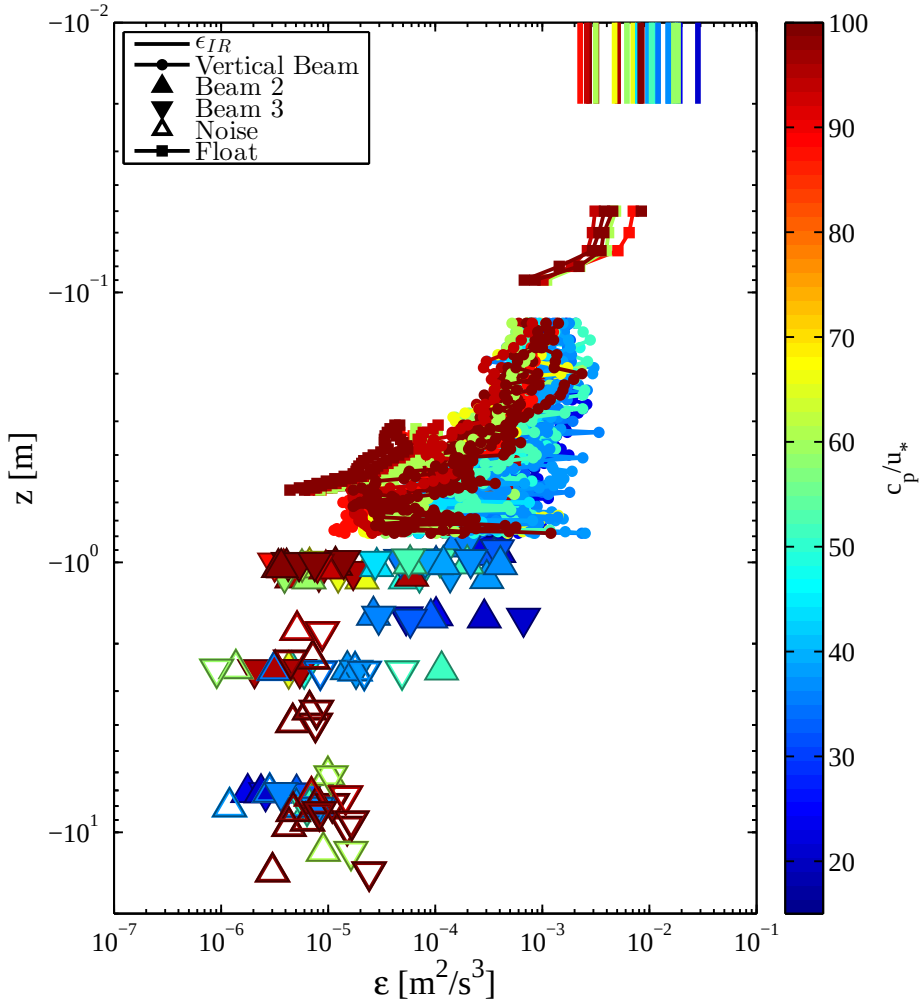

Figure 5.10: Measured subsurface dissipation profiles during SoCal 2010. Each triangle represents a 20-minute average in dissipation and depth. The line with dots are from the upward-looking beam of the near-surface LTMI and are relative to the instantaneous surface. The solid lines at the top of the plot are the simultaneous surface dissipation values measured using the stereo IR PIV system. Hollow triangles are data periods thought to be affected by the noise floor of the instrument. Color corresponds to wave age.

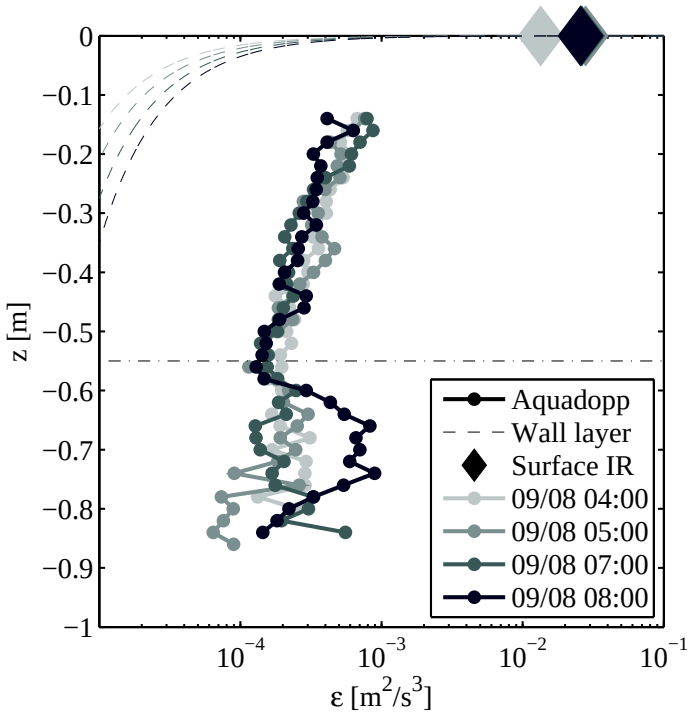

Figure 5.11: Measured subsurface dissipation profiles from the Aquadopp float during RaDyO 2009. Lines with dots are from the upward-looking beam and are relative to the instantaneous surface. Dashed lines are the wall layer, $\epsilon_{wl} = u_{*w}^3/\kappa z$. Diamonds are measured surface dissipation from the stereo IR. The dissipation values below the dash-dot line at $z = -0.55$ m are thought to be elevated due to the wake of the instrument.

5.6 Discussion

To the best knowledge of the author, there are no other direct measurements of turbulence at the ocean surface on the scales resolved here. Nonetheless, some comparisons can be made.

A first check for near-surface measurements is whether similar levels have been found by other authors. Measurements by *Gemmrich* (2010) used an upward upward-looking pulse-coherent acoustic Doppler profiler (Dopbeam, Sontek) to study near-surface dissipation the fetch-limited ($<$ 7km), low wave ($H_s < 0.5$m), low wave age conditions of Lake Washington. Figure 5.12 shows dissipation from the top 10 cm of the water column plotted as a function of mean wave saturation. The black and gray shapes are from (*Gemmrich* 2010), and the colored shapes are from this work. The band-averaged saturation was defined as

$$B_b = \int_{\sigma_p}^{\sigma_m} \sigma^{-1} B(\sigma) d\sigma, \tag{5.30}$$

where σ is the radian frequency σ_p is the spectral peak, σ_m is the upper limit of integration, and the saturation spectrum $B(\sigma) = \sigma^5 S_{\eta\eta}(\sigma)/2g^2$ is defined in terms of the frequency spectrum, $S_{\eta\eta}(\sigma)$ (*Banner et al.* 2002). *Gemmrich* (2010) chose $\sigma_m = 4\sigma_p$ which he suggested would include all scales of breaking. For this work, in open-ocean conditions, the range of breaking was much larger. The upper integration limit, σ_m, was chosen based on the peak of the nondimensionalized $\Lambda(c)$ given in chapter 4, figure 4.10. That peak is located at approximately $\hat{c} = 0.1$, where

$$\hat{c} = (c/\sqrt{gH_s})(gH_s/c_p^2)^{0.1}. \tag{5.31}$$

Solving for c, and then mapping to radian frequency using the deep water dispersion relation gives

$$\sigma_m = \frac{g}{0.1\sqrt{gH_s}} \left(\frac{gH_s}{c_p^2} \right)^{0.1}. \tag{5.32}$$

Note that there are significant contributions of breakers at $\hat{c} < 0.1$ that are not included in this definition. Considering that the stereo IR PIV data have not been separated into crest and trough components, agreement with (*Gemmrich* 2010) is good, with our measurements falling roughly between the crest and trough values.

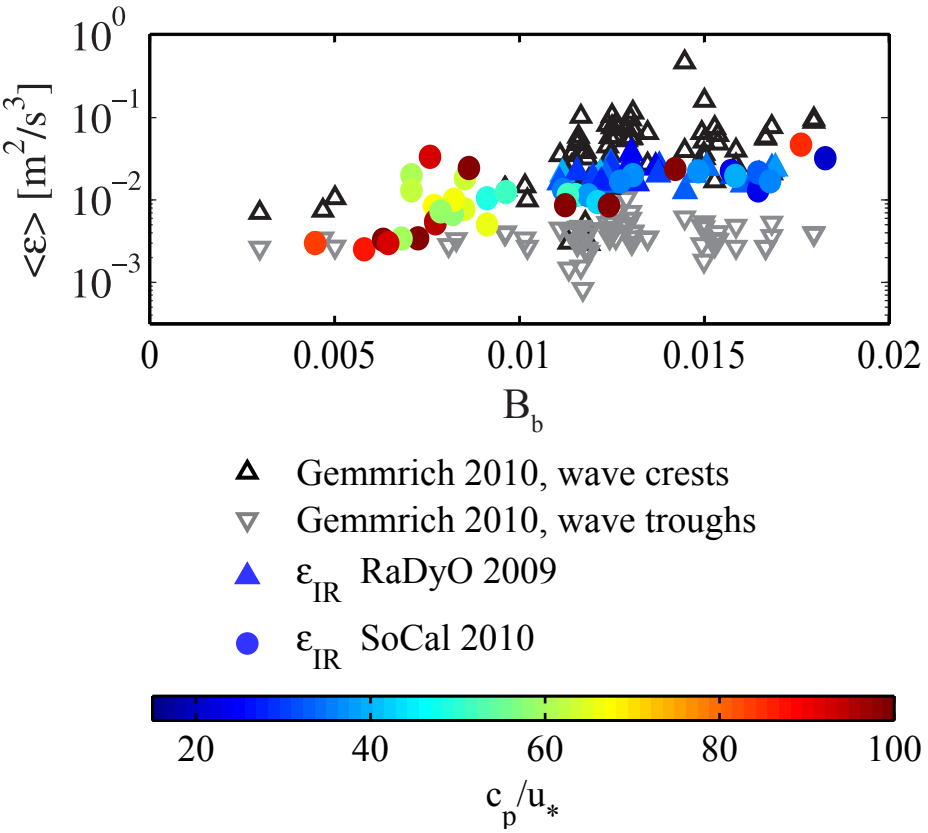

Figure 5.12: Dependence of surface dissipation on band averaged dissipation, B_b. Data from *Gemmrich* (2010) are 40-minute averages of dissipation within 10 cm of the free surface. They are separated into measurements taken beneath wave crests (black up triangles) and wave troughs (gray down triangles). Stereo IR PIV measurements are 20-minute averages, colored by wave age. Triangles are from RaDyO 2009 and circles are from SoCal 2010.

Also encouraging is that the both sets of measurements appear to have a similar threshold value of $B_b \approx 0.01$ above which dissipation increases, presumably due to the onset of breaking.

In the context of sub-surface turbulence, one of the most cited studies of elevated TKE dissipation near the surface is the work of *Terray et al.* (1996) (T96) and *Drennan et al.* (1996) (D96). They found dissipation levels exceeded those predicted by a wall layer at depths shallower than approximately 10 significant

wave heights, H_s. More specifically, D96 fit to their data a curve of the form

$$\frac{\epsilon H_s}{F_{TD}} = 0.3 \left(\frac{z}{H_s} \right)^{-2}, \tag{5.33}$$

where F_{TD} was the wind input (defined in appendix D) and z was relative to the mean surface. At greater depths, they hypothesized a return to a wall layer decay. Near to the surface, above $0.6H_s$, they expected a layer of constant dissipation. That depth was set so that the integrated water column dissipation would equal the wind input.

In this work, elevated turbulence near the surface was also found. Figure 5.13, shows the subsurface data taken here scaled by energy input as in T96. Instead of using the wind input function used by T96 and D96, dissipation was scaled by wave dissipation, F_{dsJ}. The decision to use F_{dsJ} rather than F_{TD} was made because F_{dsJ} is expected to be a more accurate measure of available energy at the relatively high wave ages of these experiments. At lower wave ages, in the $c_p/u_* = 13 - 29$ range used by *Drennan et al.* (1996), F_{TD} approaches F_{dsJ}. This can be seen in figure D.1 where the high flux values correspond to low wave ages. Another important note when comparing these data with those of D96 in figure 5.13 is that here, measurements have been made in coordinates relative to the instantaneous surface, whereas D96's were relative to the mean surface.

The measured dissipation profiles in figure 5.13 follow the same general shape, equation 5.33, as found by T96 and D96 at depths below $\mathcal{O}(H_s)$. However, above $0.6H_s$, where T96 and D96 expected a layer of constant dissipation, these results show a continued increase. Furthermore, at those shallower depths, the scaling does not appear to collapse the data. This does not directly contradict the measurements of T96 and D96, as their measurements did not extend above the troughs of the waves, and therefore could not sample this region.

More recent studies have not found the layer of constant dissipation expected by T96 and D96. Work by *Gemmrich* (2010) observed a dissipation profile that followed a z^{-1} curve from the limit of their depth measurements, approximately $2H_s$, until approximately $0.3H_s$, where dissipation was enhanced further (see figure 5.14). However, the dissipation in the z^{-1} region was not the classic

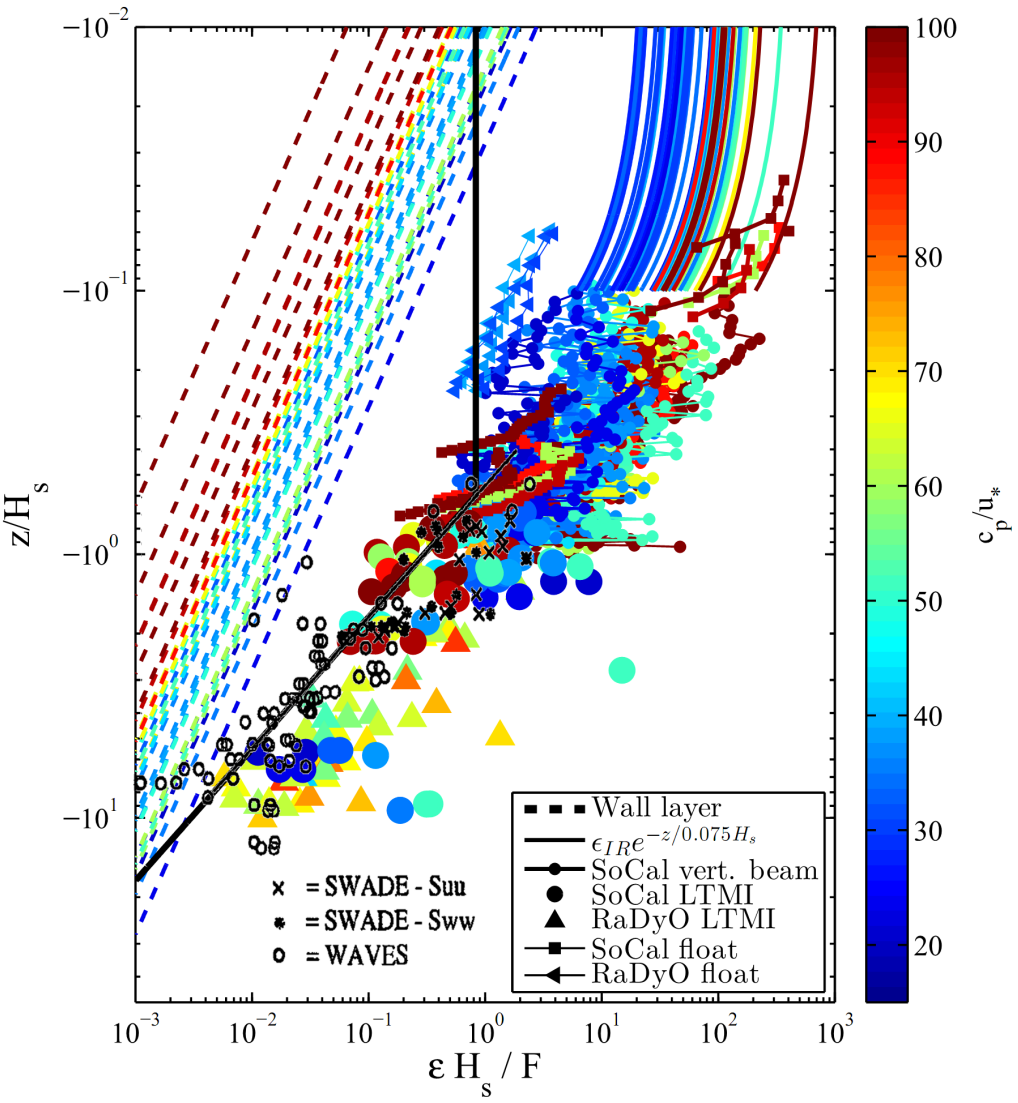

Figure 5.13: Subsurface TKE dissipation scaled by energy input, F, and significant wave height, H_s, as in T96. All data from this work used $F = F_{dsJ}$, whereas the data from T96 and D96 used $F = F_{TD}$ (see appendix D). Color corresponds to wave age and each line or symbol represents a 20-minute average. The dashed lines are the wall layer scaling, $\epsilon_{wl} = u_{*w}^3/\kappa z$. Solid lines are the surface IR measurements extended downwards using an exponential curve with an e-folding scale of $0.075H_s$. From SoCal 2010, lines with dots are from the vertical beam of the near-surface Aquadopp, circles are from the LTMI horizontal beams (with data shown in figure 5.11 but thought to be noise removed), and lines with squares are from the Aquadopp float. From RaDyO 2009, up-triangles are from the LTMI, and lines with left-triangles are from the Aquadopp float. The black symbols are the data of T96 ($\circ$) and D96 ($+$ and $*$); the thick black line indicates the best fit given by D96, $\epsilon H_s F = 0.3(z/H_s)^{-2}$, including their expected constant near-surface dissipation layer.

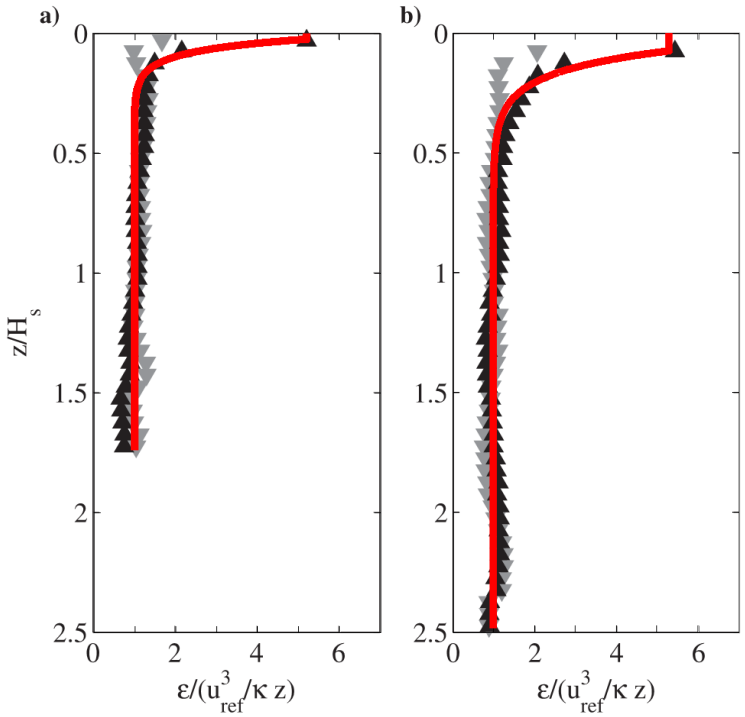

Figure 5.14: Sub-surface profiles measured by *Gemmrich* (2010). Grey triangles are from wave troughs, black triangles are from wave crests, and red curves are our fits to their wave crest data. These fits are used in figure 5.16 to include *Gemmrich* (2010) in the scaled plot. The reference velocity used was, $u_{ref} = 1.58u_*$ for the high-wind case (a), and $u_{ref} = 2.7u_*$ for the low-wind case (b).

wall layer,

$$\epsilon_{wl} = \frac{u_{*w}^3}{\kappa z}, \tag{5.34}$$

where u_{*w} is friction velocity in the water, and $\kappa = 0.4$ is the von Karman constant. Instead, an enhancement of dissipation over the wall layer, ϵ/ϵ_{wl}, by a factor of between 5 and 20, was observed. He found that ϵ/ϵ_{wl} was greatest for lower wind speeds and least for higher wind speeds. In these experiments, an enhancement over wall layer values was also observed. A trend of increased enhancement over the wall layer with increased wave age was found. Figure 5.15 shows the observed sub-surface data binned by wave age, and scaled by ϵ_{wl}. This shows that in the near-surface region, dissipation levels exceeded wall layer levels by two decades in low wave age conditions and nearly four decades in high wave ages. It also shows a decrease in scaled dissipation with increasing depth, as the dissipation profile presumably tends towards the true wall layer. Although *Gemmrich* (2010) does not note the wave ages in his experiment, it seems likely, based on the available fetch, that they were far lower than ours. This would then place his data in figure 5.15 in a manner consistent with that shown.

Figure 5.16 is similar to figure 5.13, but instead of including the wall layer, it includes a representation of the profiles found by *Gemmrich* (2010). In order to include that data, a fit has been manually taken to the data shown in figure 5.14 (b); that fit is highlighted in red in the figure. That fit produces a curve of the form

$$\frac{\epsilon}{u_{ref}^3/\kappa z} = 1 + 10e^{\frac{-|z/H_s|}{0.09}}, \tag{5.35}$$

where $u_{ref} = 2.7u_*$. A curve of this form was calculated for each sampling period, and the results are plotted in figure 5.16 as heavy dashed lines. The dashed lines are scaled fits to the data of *Gemmrich* (2010) as in figure 5.14.

The reality regarding near-surface measurements of dissipation is that, while the *Terray et al.* (1996) scaling appears to work fairly well up to within approximately H_s of the sea surface, there is little consensus on what the profile looks like above that.

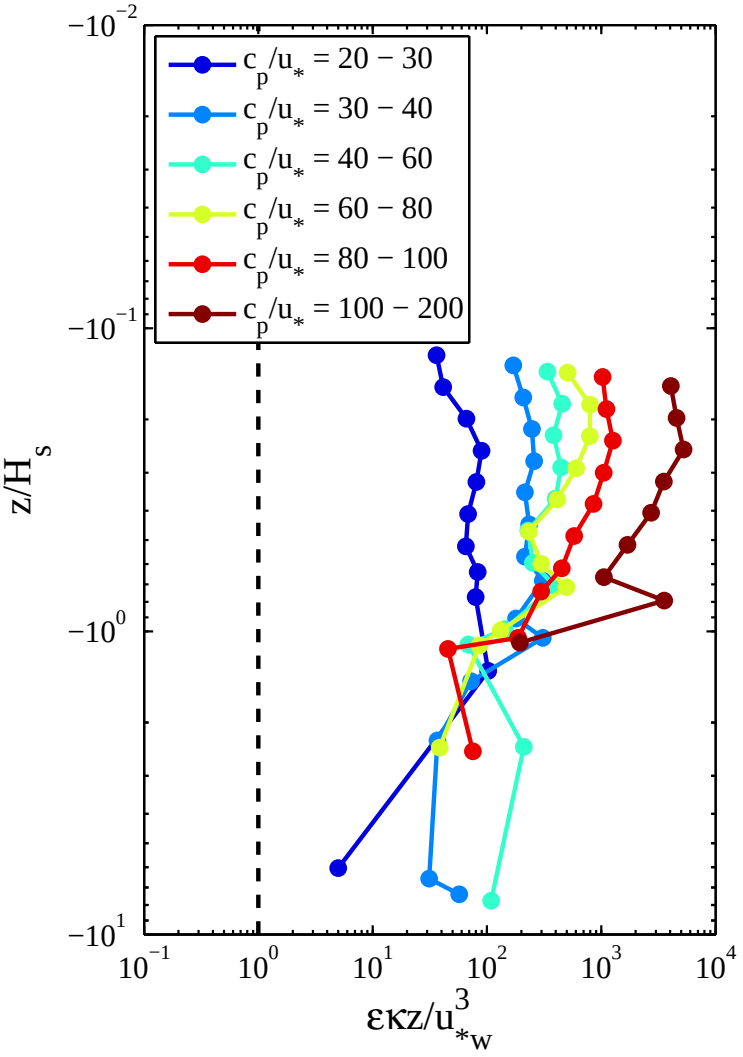

Figure 5.15: Subsurface TKE dissipation measured during the SoCal 2010 experiment. Data have been bin-averaged in wave age (coloring) and scaled by wall layer values. Note the trend towards increased ϵ/ϵ_{wall} with increased wave age.

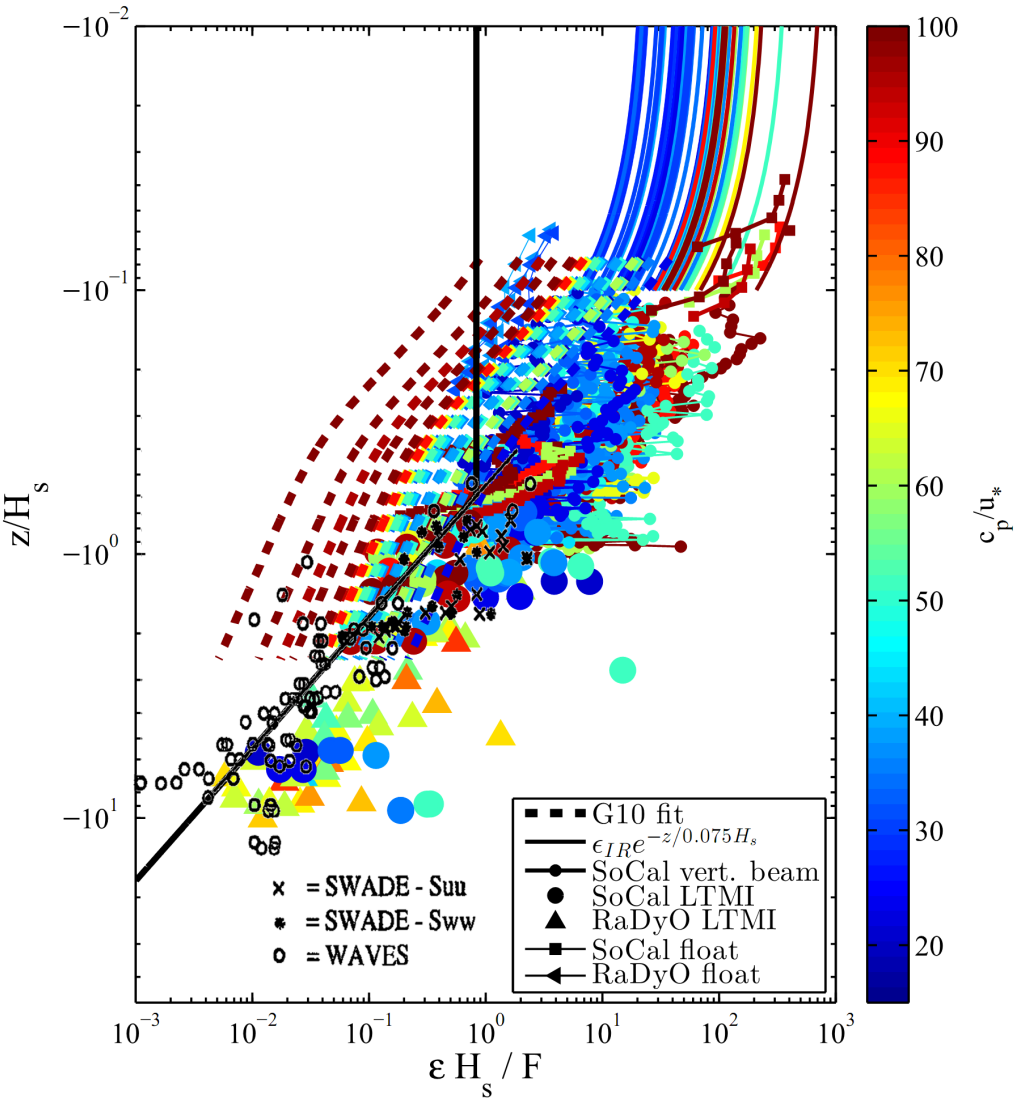

Figure 5.16: Subsurface TKE dissipation scaled by energy input, F, and significant wave height, H_s, as in T96. All data from this work used $F = F_{dsJ}$, whereas the data from T96 and D96 used $F = F_{TD}$ (see appendix D). Color corresponds to wave age and each line or symbol represents a 20-minute average. The heavy dashed lines are scaled fits to the data of *Gemmrich* (2010) as in figure 5.14. Solid lines are the surface IR measurements extended downwards using an exponential curve with an e-folding scale of $0.075H_s$. From SoCal 2010, lines with dots are from the vertical beam of the near-surface Aquadopp, circles are from the LTMI horizontal beams (with data shown in figure 5.11 but thought to be noise removed), and lines with squares are from the Aquadopp float. From RaDyO 2009, up-triangles are from the LTMI, and lines with left-triangles are from the Aquadopp float. The black symbols are the data of T96 ($\circ$) and D96 ($+$ and $*$); the thick black line indicates the best fit given by D96, $\epsilon H_s F = 0.3(z/H_s)^{-2}$, including their expected constant near-surface dissipation layer.

5.6.1 Integrated dissipation

The goal with these combined surface and sub-surface measurements is to be able to constrain the energy budget in the near-surface boundary layer.

To integrate the total sub-surface TKE dissipation, stereo IR and LTMI measurements were combined. Starting at the top, an exponential profile was assumed to connect the surface IR measurements with the top bin of vertical beam on LTMI1. Then linear interpolation was used between all LTMI depth levels. Below the bottom LTMI, a z^{-2} profile which intersected that bottom LTMI dissipation value, was assumed. The dissipation profile was integrated from the surface to the depth at which the bottom z^{-2} curve converged with the wall layer. The length scale, L_{IR-ss}, of the exponential decay used for connecting surface to sub-surface measurements was found to be closely related to H_s, with a mean value of $L_{IR-ss} = (0.075 \pm 0.04)H_S$. Figures 5.13 and 5.16 have used this length scale to extrapolate surface measurements into their log-log coordinate system.

Integrated dissipation is compared with two different energy inputs in figure 5.17. Panel (a) shows that approximately one order of magnitude more dissipation is measured than is predicted to be lost from the wave field by F_{dsJ}. Agreement is better in panel (b), where integrated dissipation is compared against $\rho_w u_{*w}^2 c_p$. However, actual estimates of wind input typically find that $F_{in} = \rho_w u_{*w}^2(\alpha c_p)$, where α ranges from 0.1 for high wave age conditions to 0.5 for low wave ages.

A large uncertainty in these measurements is the shape of the profile connecting the surface IR measurements to the sub-surface measurements. The down-triangles in figure 5.17 correspond to integrations of the sub-surface profile, neglecting the surface measurements and instead extending the uppermost sub-surface value to the surface. This results in a reduction of the total integrated dissipation by approximately a factor of two. However, that reduction still leaves measured dissipation much higher than energy input.

The large difference between wave field dissipation or wind input and integrated sub-surface dissipation, over a wide range of conditions, suggests three possibilities; the model may be underestimating dissipation, there may be errors in the measurements, or not all relevant physical processes are being considered or

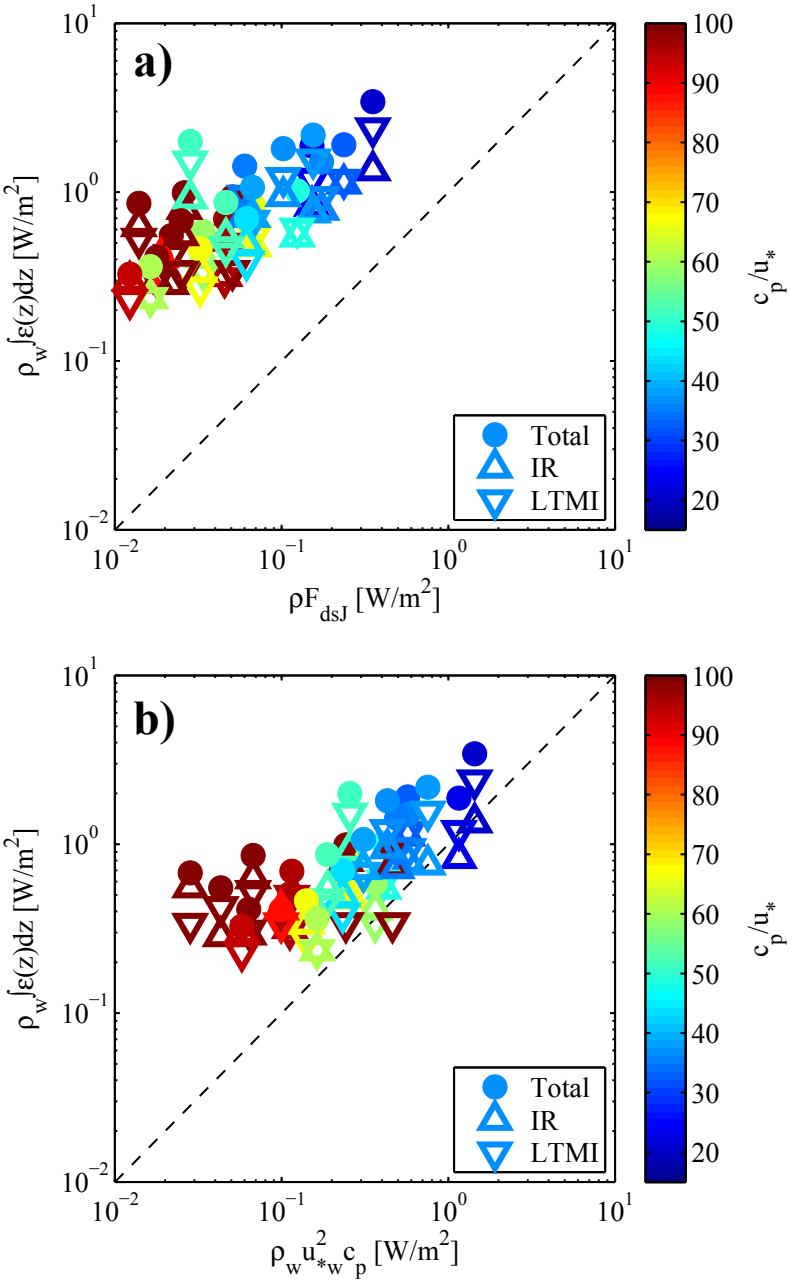

Figure 5.17: Integrated water column dissipation from SoCal 2010 compared with energy input from (a) modeled wave-field dissipation, F_{dsJ}, and (b) wind-stress scaling, $\rho_w u_{*w}^2 c_p$. Circles are total integrated dissipation, up-triangles are the integrated near-surface exponential decay, and down-triangles are the integral of the sub-surface data, assuming a layer of constant dissipation from the uppermost measurement to the surface. Coloring is by wave age.

considered correctly.

The dissipation term, F_{dsJ} (defined in equation D.2), is a modeled parameter that depends on accurate measurements of the wave field, and is a potential source of error. However, it was successfully used in chapter 4 to to balance dissipation calculated from the 5th moment of $\Lambda(c)$ at low wave ages. The $\Lambda(c)$ measurements and their associated breaking parameter are thought to be robust because their vector integrated 4th moment successfully balanced high-quality independent measurements of wind stress.

The fact that the sub-surface measurements appear to agree well with the literature (T96 and D96) at the deeper ranges is encouraging. Those deeper measurements are much easier to make than are the near-surface ones. Bubbles and surface-reflections are not present, nor are the large orbital motions that advect the wakes of instruments back into their sample volumes. Unfortunately, measurement of that near-surface region is important, as a minimum of 50% of the total dissipation in the wave-affected surface layer occurs within approximately $0.6H_s$ of the surface.

Pulse-coherent acoustic doppler profilers have been used for measurement of near-surface TKE dissipation for nearly 15 years (*Veron and Melville* 1999, *Gemmrich and Farmer* 2004, *Gemmrich* 2010, *Thomson* 2012), and have gained acceptance in the literature. However, as with any instrument attempting to measure turbulence while being advected by the wave-field, the probability of measuring it's wake at least some of the time is high. Wake effects can be reduced by clever instrument design and selective data processing, but are typically given little consideration in the literature. The LTMIs used in this work were carefully designed, through an iterative process, to vane into the mean flow, have a small instrument body for minimal flow distortion, and to maximize the distance from the sampling volumes to the instrument body. Nonetheless, measurement of wake is a possibility, and as seen in the example in appendix C, can be a significant contributor to measured dissipation.

The stereo IR PIV dissipation measurements used here were calculated using the vorticity spectral fit technique. They suffer do not suffer from either

wake effects or contamination by irrotational wave velocities, but they do make the assumption that the surface turbulence is 3D, homogeneous, and isotropic. A limiting case of anisotropy is if all the vertical motions at the surface are suppressed. The result is 2D turbulence, and as noted in section 5.4, would mean that the stereo IR PIV measurements are over-estimating dissipation by a factor of two. However, the relative agreement with the inertial scaling results (figure 5.6) suggests that anisotropy is not a significant problem in these measurements.

The remaining possibility for the mismatch between integrated dissipation and predicted energy loss from the wave field is that there are other physical processes that remain unaccounted for. Since both the measurements and the model both appear to be solidly founded, this third possibility seems likely.

5.6.2 Sampling an intermittent process

Figure 5.7 shows time series of dissipation at and near the surface. Immediately obvious is the relatively constant value of surface dissipation compared to the subsurface. A combination of factors contribute to this. Firstly, the surface measurement is taken over an approximately 2×3 m patch of the ocean, whereas the sub-surface measurements only sample a single point with their vertical beam, or a short line for the horizontal beams. This spatially averages horizontal variability in the turbulence field over those scales.

Secondly, as seen in chapter 4, more than 50% of dissipation is supported by small breaking waves. The integrated first moment of $\Lambda(c)$ gives the fraction of surface area overturned by those waves per unit time. It can be seen in figure 4.14 that the fractional overturn is 1-2 orders of magnitude larger for microbreakers than for larger air-entraining breakers. In the case of the timeseries in question, this means that any given point would see an average of one micro-breaker pass every 1.4 seconds, whereas it would only see an average of one large air-entraining breaker pass every 80 s. Breakers inject turbulence to depths comparable to their height, so the deeper the instrument, the more intermittent its breaker-driven turbulence will become.

The explanation for the behavior of the dissipation timeseries in figure 5.7

is then clear. The IR cameras spatially average extremely frequent micro-breakers, whereas the deep horizontal Aquadopp beams only sample the much more intermittent large breakers.

Those intermittent effects are very important for the average dissipation. In the case of beams 2 and 3 in figure 5.7, individual events are up to three orders of magnitude larger than the mean background dissipation level. Thus, in a 1200 s record sampled at 2 Hz, only 3 high-dissipation events are needed to account for more total energy dissipation than the entire record at the background level.

5.6.3 Wave coherence

To study the coherence of the dissipation at the surface with the surface wave field, frequency spectra and co-spectra of surface displacement and dissipation were calculated. An example of these spectra as well as phase and squared coherence (SC) of the cospectra are shown in Figure 5.18 for a 20 minute period starting 2009/09/08 04:00 [UTC]. Two regions of elevated squared coherence and associated phase can be seen: a low frequency range with wave periods between 15 s and 5 s and a high frequency range with periods between approximately 4 s and 2 s. The phase of the higher frequency coherence peak suggests that the dissipation peaks approximately 90° after the wave peaks. For frequencies near the wind wave peak, the dissipation leads the waves by approximately 135 - 180°.

Dissipation as a function of wave phase is shown in Figure 5.20 for the high frequency range. For this figure, the surface displacement $\eta(t)$ was first filtered with an order 48 FIR bandpass filter covering the frequency range specified. The Hilbert transform H of the filtered time series was computed and the wave phase was taken to be the arctangent of the imaginary over the real component of H, that is, $\theta = \tan^{-1}(\Im(H)/\Re(H))$. Dissipation was then averaged over 45° bins of θ. As expected, figure 5.20 shows that dissipation reaches a minimum 90° before the wave crest and a maximum 90° after. However, the phase dependent signal is small compared to both the mean dissipation and spread of data. These values were typical, as can be seen in the distributions in figure 5.19.

Both the phase dependence and the strength of the phase-coherent signal

observed here are in contrast with the observations by *Gemmrich* (2010) of significant dissipation enhancement at the wave crests. However, his wave conditions were strongly fetch-limited with very low peak wave length and significant wave height compared to the wave conditions of these experiments.

The 90° phase lag at the wind-wave peak is not surprising. Figure 5.21 shows an example timeseries of dissipation during the passage of a large breaking wave. The dissipation immediately increases as the breaker passes and then slowly decays - in this case with a time constant of approximately 1 wave period. A dissipation timeseries starting with a step function at the wave peak, followed by an exponential decay, will result in a phase-lag of between 0° and 90° depending on the ratio of dissipation time constant to wave period, T_{decay}/T_{wave}. It can be shown that when $T_{decay}/T_{wave} << 1$, the phase lag approaches 0, and when $T_{decay}/T_{wave} \geq 1$, the phase lag will be 90°. Another effect of having a large T_{decay}/T_{wave} is that the difference between dissipation values at the wave peak vs the wave trough are reduced.

Chapter 5, in part, is currently being prepared for submission for publication. Sutherland, P. and Melville, W. K., Near surface turbulence associated with breaking waves. The dissertation author was the primary investigator and author of this paper.

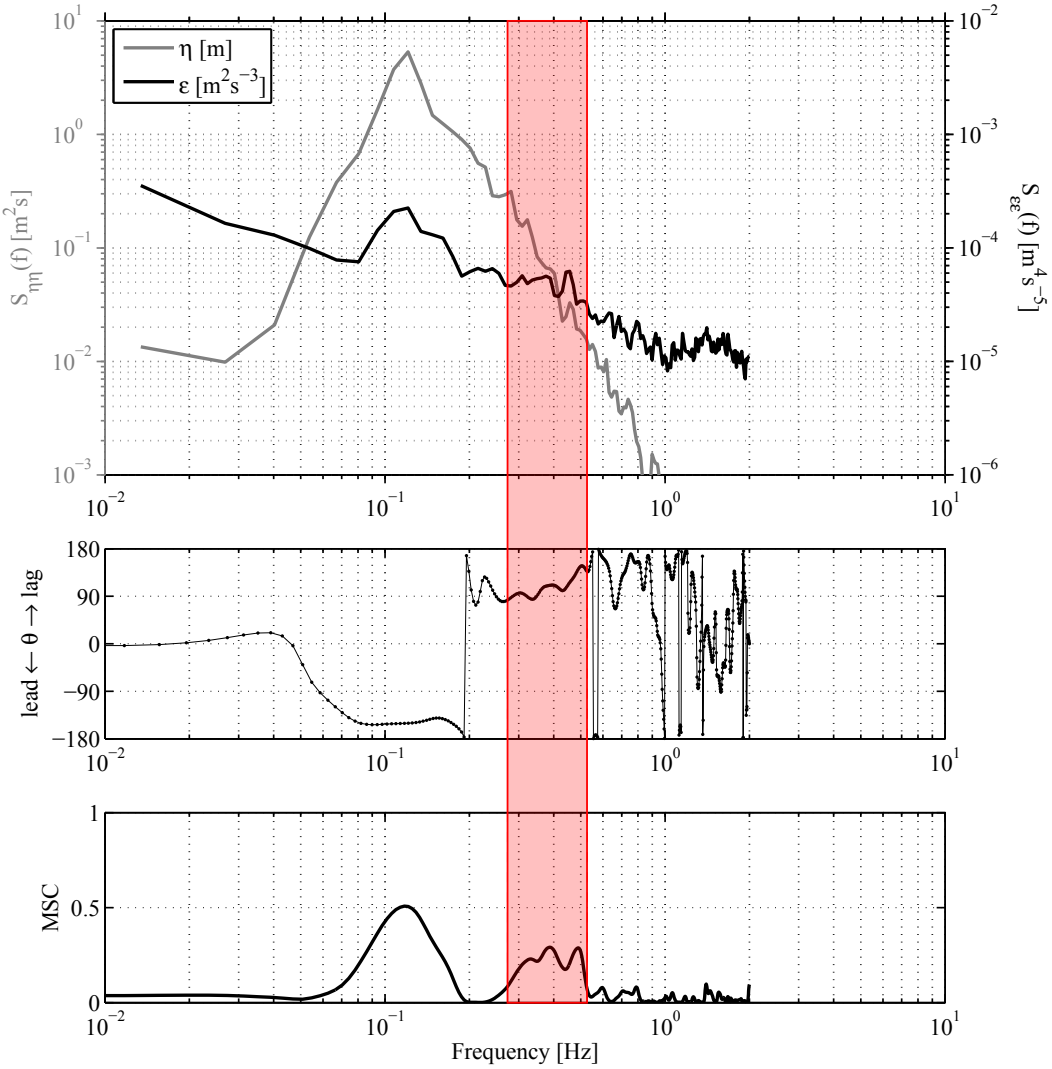

Figure 5.18: Coherence of surface displacement and dissipation. Top: frequency spectra of surface displacement η [m] and dissipation ϵ [m^2/s^3]. Centre: Phase of wave-dissipation coherence. Angles are defined such that at 90°, the dissipation lags the wave peak by 90°. Bottom: Magnitude squared coherence between dissipation and displacement. The pink highlighted region is the frequency band to which the wave signal was filtered for computation of the wave-phase average dissipation shown in Figure 5.20. Data are from RaDyO 2009, and represent the 20-minute period starting 2009/09/08 04:00 [UTC].

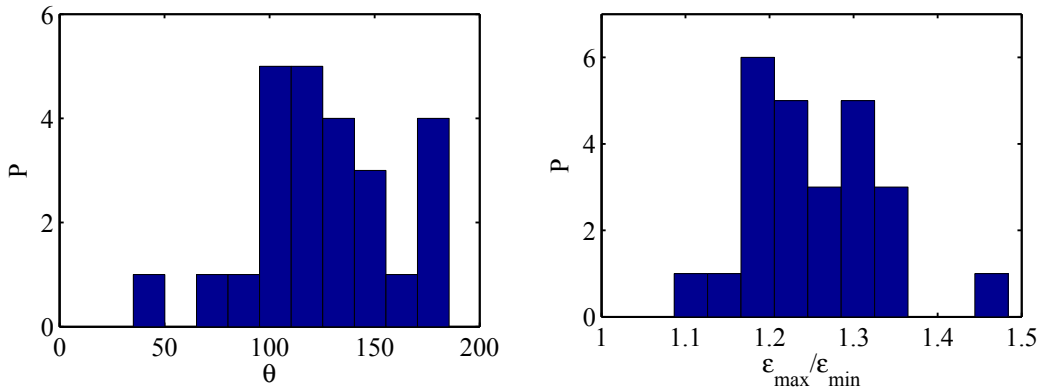

Figure 5.19: Histograms of phase (left) and ratio of dissipation at the coherence peak vs coherence trough (right) for the RaDyO 2009 experiment.

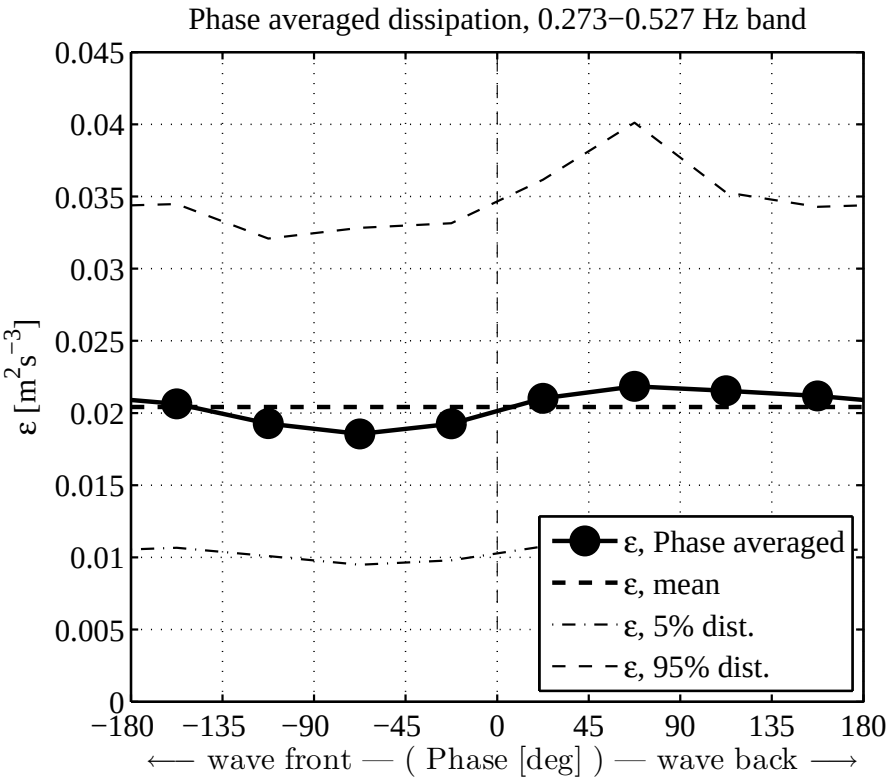

Figure 5.20: Wave phase averaged dissipation corresponding to waves with periods between 2 s and 4 s. The wave peak is at $\theta = 0$, and the wave is propagating to the left. Data are from RaDyO 2009, and represent the 20-minute period starting 2009/09/08 04:00 [UTC].

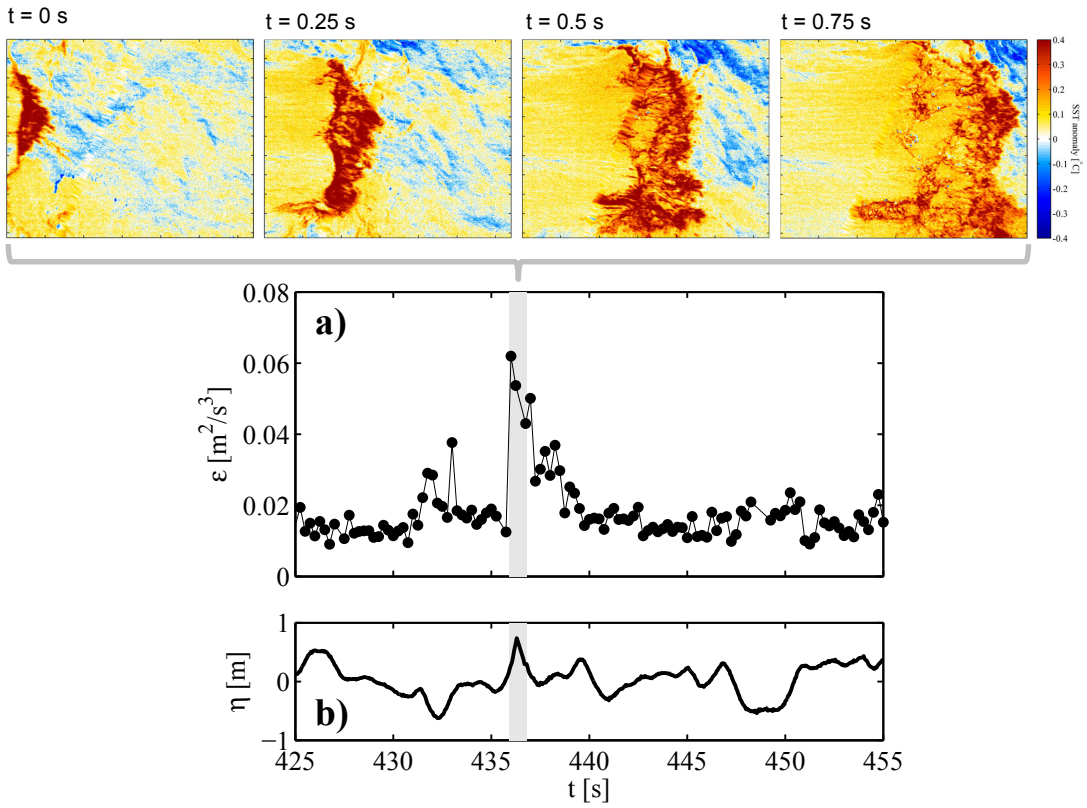

Figure 5.21: Increased dissipation from large breaking wave. Top panels show IR images of the sea surface separated by 0.25s. Temperature anomaly scale is from -0.4°C (blue) to 0.4°C (red). Below, timeseries of dissipation (a) and surface elevation (b) as the breaker passes through the IR camera field of view. The shaded area is the duration during which the breaking front was in the field of view. The surface elevation is that of a 10 cm×10 cm patch in the center of the image. The time axis is seconds since 2010/12/06 22:00 [UTC], during the SoCal 2010 experiment.

Chapter 6

Conclusions

This work presents a new technique for making measurements at the air-sea interface. Using stereo IR thermal structure PIV, the 3D sea surface velocity was measured over an area of approximately 3 m×2 m.

The first part of this dissertation, focused on chapter 4, describes measurements of breaker crest length distributions, $\Lambda(c)$, over a range of speeds extending into the high-wavenumber gravity-wave spectrum. These measurements were found to agree well with visible video measurements at high breaking crest speeds. However, at low speeds, the IR measurements continued to extend upwards with decreasing speed beyond where the visible measurements roll off due to the the lack of air-entrainment in slower micro-breakers. Since there were no previous field measurements of $\Lambda(c)$ at these scales, several new results were found.

By capturing more of the range of $\Lambda(c)$, to speeds within error of the 23 cm/s gravity-capillary transition, it was possible to derive a nondimensional scaling of $\Lambda(c)$ in terms of wave age, c_p/u_*, ballistic velocity, $\sqrt{gH_s}$, and wave peak steepness, gH_s/c_p^2. It was observed that, while at high speeds, previous visible-video measurements of $\Lambda(c)$ fell on this curve, their low-speed roll off did not occur uniformly - highlighting the difficulty of nondimensionalizing $\Lambda(c)$ without measurements that cover enough range in c.

The fourth and fifth moments of $\Lambda(c)$, in concert with the modeled breaking parameter, b, from *Romero et al.* (2012) were found to balance measured wind stress and modeled wave field dissipation at wave ages $c_p/u_* < 50$. The effect that

these low-speed breakers had on the integrated moments was significant. More than 50% of surface dissipation, and at high wave ages an even higher fraction of stress, was found to be due to waves with breaking speeds below 2 m/s or wavelengths $\lambda < 2.5$ m (the approximate lower limit of air-entraining breakers). Naturally, the lower moments of $\Lambda(c)$ were even more strongly affected by the low speed breakers, with 1-2 orders of magnitude more breakers passing a given point per unit time with speeds below 2 m/s than with speeds above 2 m/s. This is an equivalently elevated fractional overturning of the sea surface per unit time, which is an important parameter for heat and gas exchange between the atmosphere and ocean.

Since the dynamical significance of non air entraining micro-breakers has now been highlighted, it will be important for future experiments to include their effects.

The second part of this dissertation, focused on chapter 5, was the direct measurement of TKE dissipation at the surface and in the wave-affected boundary layer beneath. Using measured velocity fields from the same stereo IR PIV system, a new technique was developed to measure dissipation at the sea surface. By separating the rotational turbulence velocities from the irrotational wave velocities, it was possible to study turbulent fluctuations uncontaminated by irrotational wave motions. This removed the principle difficulties of sampling turbulence near the air-sea boundary - namely contamination of the velocity field. A technique was developed for extracting TKE dissipation from the rotational velocity field. Testing the method over a broad range of environmental conditions showed good self-consistency (see figure 5.6) and agreement with previous near-surface measurements (figure 5.12).

Simultaneous sub-surface measurements of TKE dissipation were made with an array of pulse-coherent acoustic Doppler profilers. By connecting the sub-surface values with surface values, it was possible to estimate total integrated dissipation in the wave-affected surface boundary layer. These measurements have considerable uncertainty, but can be considered to be an upper bound on near-surface TKE dissipation.

Moving forwards, the question of where and how wave energy is dissipated remains open. Although we have developed a technique for measuring turbulence at the surface, and measurements agree well with the literature in the region below approximately $0.6H_s$ from the surface, the question of how much energy is dissipated in that top layer remains. This is an important question. It may account for 50% or more of the dissipation in the wave-affected boundary layer. In order to resolve this, new techniques will likely have to be developed. Techniques that don't include an instrument swimming in its own wake or measuring some inseparable combination of waves and turbulence in the water column.

Appendix A

Expected form of $\Lambda(\boldsymbol{c})$

Phillips (1985) notes that in a wave field in equilibrium, the left side of Equation 1.1 is zero, leaving a balance between the wave energy source terms for wind input, non-linear transfers between wavenumbers, and dissipation,

$$0 = S_{in} + S_{nl} + S_{ds}. \tag{A.1}$$

He uses this to derive the rate of energy loss from the wavenumber spectrum as

$$\begin{aligned} \epsilon(\boldsymbol{k})d\boldsymbol{k} &= \omega\rho_w D(\boldsymbol{k})d\boldsymbol{k} && \text{(A.2)} \\ &= \omega\gamma\rho_w g k^{-4} B^3(\boldsymbol{k})d\boldsymbol{k}, && \text{(A.3)} \end{aligned}$$

where $D(\boldsymbol{k}) = \gamma g k^{-4} B^3(\boldsymbol{k})$ is the spectral rate of wave action dissipation, γ is a numerical constant, and

$$B(\boldsymbol{k}) \equiv k^4 F(\boldsymbol{k}) \tag{A.4}$$

is the dimensionless wave field saturation spectrum.

The corresponding function of velocity $\boldsymbol{c}$, was defined

$$\epsilon(\boldsymbol{c})d\boldsymbol{c} = 2\epsilon(\boldsymbol{k})d\boldsymbol{k} \tag{A.5}$$

Noting that $k = g/c^2$ and that $d\boldsymbol{k} = -2g^2 c^{-6} d\boldsymbol{c}$, A.3 can be written

$$\epsilon(\boldsymbol{c})d\boldsymbol{c} = 4\gamma\rho_w B^3(\boldsymbol{k})c d\boldsymbol{c}. \tag{A.6}$$

Equating Equations A.6 and 4.3 gives an expected form for $\Lambda(\boldsymbol{c})$ of

$$\Lambda(\boldsymbol{c}) = \frac{4g\gamma}{b} c^{-4} B^3(\boldsymbol{k}), \tag{A.7}$$

where b is the dimensionless "breaking parameter."

Integrating $\Lambda(\boldsymbol{c})$ over θ then gives an expression for the mean length of of crests per unit area of ocean surface as a function of breaker speed,

$$\Lambda(c) = \int_{-\pi/2}^{\pi/2} \Lambda(\boldsymbol{c}) c d\theta. \tag{A.8}$$

Phillips (1985) assumed a constant value for the breaking parameter b and defined the saturation function as

$$B(\boldsymbol{k}) = \beta(\cos\theta)^p \left(\frac{u_*}{c}\right), \tag{A.9}$$

where β is a numerical constant, θ is the angle between the wind and the wavenumber $\boldsymbol{k}$, p is an empirical constant that describes spectral spreading, and u_* is the atmospheric friction velocity. Applying Equation A.9 to Equation A.8 yields

$$\Lambda(c) = 4g\gamma\beta^3 u_*^3 b^{-1} c^{-6} \int_{-\pi/2}^{\pi/2} (\cos\theta)^{3p} d\theta, \tag{A.10}$$

the well known $\Lambda(c) \sim c^{-6}$ relationship.

The breaking parameter b was originally estimated by *Duncan* (1981) to be $b = 0.009/\sin(\theta_{LS})$, where θ_{LS} is the local slope of the breaking wave. Further work by *Rapp and Melville* (1990), *Melville* (1994), *Banner and Peirson* (2007), *Drazen et al.* (2008), and this author (unpublished) much improved upon Duncan's work by using focussing wave packets instead of a towed hydrofoil. The slope dependence of b was nicely summarised by *Romero et al.* (2012) in which it was shown that although there is considerable spread in the data, the curve

$$b = 0.4(S - 0.08)^{5/2}, \tag{A.11}$$

where S is the maximum linear slope of the focussing packet, fits the data reasonably well. *Romero et al.* (2012) went on to model the wavenumber dependence of the breaking parameter. They proposed a form of

$$b(k) = A_1 \left[B(k)^{1/2} - B_T^{1/2}\right]^{5/2}, \tag{A.12}$$

where A_1 and B_T are empirically determined constants and

$$B(k) = \int B(\boldsymbol{k}) d\theta. \tag{A.13}$$

Appendix B

Review of spectra of turbulence

This appendix contains a review of classical spectral descriptions of turbulence and has been included as a reference for chapter 5. With the possible exception of section B.4.2, the discussion of directional vorticity spectra for 2D homogeneous isotropic turbulence, none of this is new material.

B.1 Introduction

Following *Batchelor* (1953) and *Pope* (2000), in homogeneous turbulence the velocity correlation tensor, R_{ij} is defined

$$R_{ij}(\boldsymbol{r}) = \overline{u_i(\boldsymbol{x})u_j(\boldsymbol{x}+\boldsymbol{r})}. \tag{B.1}$$

The autospectral density tensor $\Phi_{ij}(\boldsymbol{k})$ is defined as the Fourier transform of the velocity correlation tensor (e.g. *Bendat and Piersol* (2010), pp.118; *Pope* (2000), pp.221; *Batchelor* (1953), pp.32)

$$\Phi_{ij}(\boldsymbol{k}) = \mathcal{F}\left\{R_{ij}(\boldsymbol{r})\right\} = \frac{1}{(2\pi)^3}\iiint_{-\infty}^{\infty} R_{ij}(\boldsymbol{r})e^{-i\boldsymbol{k}\cdot\boldsymbol{r}}d\boldsymbol{r}, \tag{B.2}$$

with the inverse relation

$$R_{ij}(\boldsymbol{r}) = \mathcal{F}^{-1}\left\{\Phi_{ij}(\boldsymbol{k})\right\} = \frac{1}{(2\pi)^3}\iiint_{-\infty}^{\infty} \Phi_{ij}(\boldsymbol{k})e^{i\boldsymbol{k}\cdot\boldsymbol{r}}d\boldsymbol{k}. \tag{B.3}$$

This relation leads to

$$\overline{\frac{\partial u_i}{\partial x_k}\frac{\partial u_j}{\partial x_l}} = \iiint_{-\infty}^{\infty} k_k k_l \Phi_{ij}(\boldsymbol{k}) d\boldsymbol{k} \tag{B.4}$$

and

$$\epsilon = \iiint_{-\infty}^{\infty} 2\nu k^2 \tfrac{1}{2}\Phi_{ij}(\boldsymbol{k}) d\boldsymbol{k}. \tag{B.5}$$

The energy spectrum function $E(k)$ discards the directional information contained in the autocorrelation density spectrum and is defined as

$$E(k) = \oint \tfrac{1}{2}\Phi_{ii}(\boldsymbol{k}) d\mathcal{S}(k), \tag{B.6}$$

where $\mathcal{S}(k)$ is a sphere of radius k in wavenumber space. The integral of the energy spectrum function is equal to the turbulent kinetic energy

$$T.K.E. = \tfrac{1}{2}\overline{u_i(\boldsymbol{x})u_i(\boldsymbol{x})} = \int_0^{\infty} E(k) dk. \tag{B.7}$$

The spectrum of dissipation is then

$$D(k) = 2\nu k^2 E(k), \tag{B.8}$$

which can be integrated to get the total T.K.E. dissipation rate,

$$\epsilon = \int_0^{\infty} D(k) dk = 2\nu \int_0^{\infty} k^2 E(k) dk. \tag{B.9}$$

One dimensional spectra can also be extracted from the autospectral density tensor. For example, $E_{22}(k_1)$, the spectra of u_2 (transverse) velocity fluctuations measured in the x_1 direction is defined by

$$E_{22}(k_1) = 2 \iint_{-\infty}^{\infty} \Phi_{22}(\boldsymbol{k}) dk_2 dk_3, \tag{B.10}$$

and $E_{11}(k_1)$, the spectra of u_1 (longitudinal) velocity fluctuations in the x_1 direction is defined by

$$E_{11}(k_1) = 2 \iint_{-\infty}^{\infty} \Phi_{11}(\boldsymbol{k}) dk_2 dk_3. \tag{B.11}$$

The integrals of these directional spectra over all wavenumbers correspond to the variance of velocity fluctuations in that direction, ie.

$$\overline{u_2^2} = \int_0^{\infty} E_{22}(k_1) dk_1, \qquad \text{and} \qquad \overline{u_1^2} = \int_0^{\infty} E_{11}(k_1) dk_1 \tag{B.12}$$

B.2 Isotropic turbulence

In isotropic turbulence, the energy spectrum function, $E(k)$, contains all the information in $\Phi_{ij}(\boldsymbol{k})$. Again, from *Pope* (2000), pp. 222, in isotropic turbulence, the directional information can depend only on $\boldsymbol{k}$, so scalar multiples of δ_{ij} and $k_i k_j$ are the only possible components of the autospectral density tensor:

$$\Phi_{ij}(\boldsymbol{k}) = A(k)\delta_{ij} + B(k)k_i k_j. \tag{B.13}$$

Using Equation B.6 and incompressibility, $k_i \Phi_{ij}(\boldsymbol{k}) = 0$, it can be shown that

$$\Phi_{ij}(\boldsymbol{k}) = \frac{E(k)}{4\pi k^2}\left(\delta_{ij} - \frac{k_i k_j}{k^2}\right). \tag{B.14}$$

Substituting Equation B.14 into Equation B.11 gives

$$E_{11}(k_1) = 2\iint_{-\infty}^{\infty} \frac{E(k)}{4\pi k^2}\left(1 - \frac{k_1^2}{k^2}\right) dk_2 dk_3, \tag{B.15}$$

which can be rewritten as

$$E_{11}(k_1) = \int_{k_1}^{\infty} \frac{E(k)}{k}\left(1 - \frac{k_1^2}{k^2}\right) dk. \tag{B.16}$$

The longitudinal and transverse spectra can then be related (*Pope* 2000) by

$$E_{22}(k_1) = \tfrac{1}{2}\left(E_{11}(k_1) - k_1 \frac{dE_{11}(k_1)}{dk_1}\right). \tag{B.17}$$

Kolmogorov's similarity hypothesis predicts that in the inertial subrange, the energy spectrum function will have a form of

$$E(k) = C\epsilon^{2/3}k^{-5/3}, \tag{B.18}$$

where $C \sim 1.5$ is an experimentally derived constant (e.g. *Grant et al.* 1962). Substituting this relation into B.16 and B.17 give the well known inertial subranges for longitudinal and transverse velocity spectra

$$E_{11}(k_1) = \tfrac{18}{55}C\epsilon^{2/3}k^{-5/3} \tag{B.19}$$

$$E_{22}(k_1) = \tfrac{4}{3}E_{11}(k_1) = \tfrac{24}{55}C\epsilon^{2/3}k^{-5/3}. \tag{B.20}$$

B.3 Vorticity spectra and dissipation

Similarly to $R_{ij}(\boldsymbol{r})$ for velocity, a *vorticity* correlation tensor $Q_{ij}(\boldsymbol{r})$ can be defined

$$Q_{ij}(\boldsymbol{r}) \equiv \overline{\omega_i(\boldsymbol{x})\omega_j(\boldsymbol{x}+\boldsymbol{r})}. \tag{B.21}$$

The vorticity correlation tensor can be related to the velocity correlation tensor (using $\boldsymbol{x'} = \boldsymbol{x} + \boldsymbol{r}$) by

$$Q_{ij}(\boldsymbol{r}) = \overline{\omega_i(\boldsymbol{x})\omega_j(\boldsymbol{x'})} = \epsilon_{ilm}\epsilon_{jpq}\overline{\frac{\partial u_m(\boldsymbol{x})}{\partial x_l}\frac{\partial u_m(\boldsymbol{x'})}{\partial x'_p}} = -\epsilon_{ilm}\epsilon_{jpq}\frac{\partial^2 R_{mq}(\boldsymbol{r})}{\partial r_l \partial r_p} \tag{B.22}$$

$$= -\delta_{ij}\nabla^2 R_{ll}(\boldsymbol{r}) + \frac{\partial^2 R_{ll}(\boldsymbol{r})}{\partial r_i \partial r_j} + \nabla^2 R_{ji}(\boldsymbol{r}). \tag{B.23}$$

Following *Batchelor* (1953) pp. 38-39 the vorticity spectrum tensor Ω_{ij} is defined by

$$\Omega_{ij}(\boldsymbol{k}) = \mathcal{F}\left\{Q_{ij}(\boldsymbol{r})\right\} = \mathcal{F}\left\{\overline{\omega_i(\boldsymbol{x})\omega_j(\boldsymbol{x}+\boldsymbol{r})}\right\}. \tag{B.24}$$

and substituting into Equation B.23, the vorticity spectrum tensor can be written

$$\Omega_{ij}(\boldsymbol{k}) = (\delta_{ij}k^2 - k_i k_j)\Phi_{ll}(\boldsymbol{k}) - k^2\Phi_{ji}(\boldsymbol{k}). \tag{B.25}$$

Contributions to mean squared vorticity can then be related with

$$\Omega_{ii}(\boldsymbol{k}) = k^2\Phi_{ii}(\boldsymbol{k}), \tag{B.26}$$

or in the case of isotropy (applying Equation B.14),

$$\Omega_{ii}(\boldsymbol{k}) = \frac{E(k)}{4\pi}\left(1 - \frac{k_i^2}{k^2}\right). \tag{B.27}$$

Two dimensional spectra, $\phi_{\omega_i}(k_1, k_2)$, of vorticity in the horizontal directions k_1 and k_2 can then be formed by integrating $\Omega_{ii}(\boldsymbol{k})$ in the vertical (k_3) direction to give

$$\phi_{\omega_i}(k_1, k_2) = \int_{-\infty}^{\infty} \Omega_{ii}(\boldsymbol{k})dk_3. \tag{B.28}$$

Spectra calculated in this work from the sea-surface field of vertical vorticity are thought to represent isotropic turbulence, the theoretical 2D spectra of which is represented by

$$\phi_{\omega_3}(k_1, k_2) = \int_{-\infty}^{\infty} \frac{E(k)}{4\pi}\left(1 - \frac{k_3^2}{k^2}\right)dk_3. \tag{B.29}$$

One dimensional spectra, $\phi_{\omega_i}(k_1)$, of vorticity ω_i, in a single direction k_1 can be calculated

$$\phi_{\omega_i}(k_1) = \int\int_{-\infty}^{\infty} \Omega_{ii}(\boldsymbol{k}) dk_2 dk_3 = \int_{-\infty}^{\infty} \phi_{\omega_i}(k_1, k_2) dk_2, \tag{B.30}$$

where

$$\overline{\omega_i^2} = \int_{-\infty}^{\infty} \phi_{\omega_i}(k_1) dk_1 \tag{B.31}$$

Following *Antonia et al.* (1988), by assuming isotropy and then substituting B.14 and B.26 into B.30 to get

$$\phi_{\omega_i}(k_1) = \iint_{-\infty}^{\infty} \frac{E(k)}{4\pi} \left(1 - \frac{k_i^2}{k^2}\right) dk_2 dk_3, \tag{B.32}$$

it is possible to derive expressions for vorticity spectra in terms of the energy spectrum function $E(k)$:

$$\begin{aligned} \phi_{\omega_2}(k_1) = \phi_{\omega_3}(k_1) &= \frac{1}{2} k_1^2 \int_{k_1}^{\infty} \frac{E(k)}{k} dk + \frac{1}{4} \int_{k_1}^{\infty} \frac{E(k)}{k} (k^2 - k_1^2) dk \\ &= \frac{1}{4} k_1^2 \int_{k_1}^{\infty} \frac{E(k)}{k} dk + \frac{1}{4} \int_{k_1}^{\infty} kE(k) dk, \end{aligned} \tag{B.33}$$

$$\phi_{\omega_1}(k_1) = \frac{1}{2} \int_{k_1}^{\infty} \frac{E(k)}{k} (k^2 - k_1^2) dk. \tag{B.34}$$

The spectra of the surface vertical vorticity measurements presented here are $\phi_{\omega_3}(k_1)$ and $\phi_{\omega_3}(k_2)$, which are expected to have the form of Equation B.33.

B.4 Two-dimensional turbulence

In this work, the velocity field of turbulence is being measured at the sea surface, a region where the assumption of isotropy is difficult to justify. It seems that at the air-sea interface, vertical turbulent velocity fluctuations should be suppressed and turbulence may then behave like 2D turbulence. A similar behaviour has been observed in highly stratified atmospheric flows (*Lindborg* 2007).

Two dimensional turbulence behaves structurally very differently from 3D turbulence due to the lack of vortex stretching and tilting (*Salmon* 1998). In two dimensions, the stream function ψ can be defined by

$$u = -\frac{\partial \psi}{\partial y}, \qquad v = \frac{\partial \psi}{\partial x}. \tag{B.35}$$

which means

$$\omega = \nabla^2 \psi. \tag{B.36}$$

The enstrophy Z is then defined by

$$Z \equiv \iint \left(\nabla^2 \psi\right)^2 d\boldsymbol{x}. \tag{B.37}$$

The quantity $k^2 E(k)$ is the enstrophy spectrum, and it's integral, the second moment of the energy spectrum, is equal to the enstrophy

$$Z = \int_0^\infty k^2 E(k) dk. \tag{B.38}$$

Following is a derivation of the form of the 2D vorticity spectrum paralleling the method outlined above for 3D turbulence.

The two dimensional form of Equation B.1, the velocity correlation tensor,

$$R_{ij}(\boldsymbol{r}) = \overline{u_i(\boldsymbol{x}) u_j(\boldsymbol{x} + \boldsymbol{r})}. \tag{B.39}$$

is no different than that for 3D except that $\boldsymbol{x}$ and $\boldsymbol{r}$ are now two-dimensional vectors and i, j can only be cycled over 2 dimensions. It then follows that equations B.2 and B.3 can be re-written

$$\Phi_{ij}(\boldsymbol{k}) = \mathcal{F}\left\{R_{ij}(\boldsymbol{r})\right\} = \frac{1}{(2\pi)^2} \iint_{-\infty}^{\infty} R_{ij}(\boldsymbol{r}) e^{-i\boldsymbol{k}\cdot\boldsymbol{r}} d\boldsymbol{r}, \tag{B.40}$$

with the inverse relation

$$R_{ij}(\boldsymbol{r}) = \mathcal{F}^{-1}\left\{\Phi_{ij}(\boldsymbol{k})\right\} = \frac{1}{(2\pi)^2} \iint_{-\infty}^{\infty} \Phi_{ij}(\boldsymbol{k}) e^{i\boldsymbol{k}\cdot\boldsymbol{r}} d\boldsymbol{k}. \tag{B.41}$$

Just as in 3D, this relation leads to

$$\overline{\frac{\partial u_i}{\partial x_k} \frac{\partial u_j}{\partial x_l}} = \iint_{-\infty}^{\infty} k_k k_l \Phi_{ij}(\boldsymbol{k}) d\boldsymbol{k} \tag{B.42}$$

and

$$\epsilon = \iint_{-\infty}^{\infty} 2\nu k^2 \tfrac{1}{2} \Phi_{ij}(\boldsymbol{k}) d\boldsymbol{k}. \tag{B.43}$$

The energy spectrum function $E(k)$ is then defined as

$$E(k) = \oint \tfrac{1}{2} \Phi_{ii}(\boldsymbol{k}) d\mathcal{L}(k), \tag{B.44}$$

where $\mathcal{L}(k)$ is a circle of radius k in wavenumber space. The integral of the energy spectrum function is equal to the turbulent kinetic energy

$$\tfrac{1}{2}\overline{u_i(\boldsymbol{x})u_i(\boldsymbol{x})} = \int_0^\infty E(k)dk. \tag{B.45}$$

One dimensional spectra can also be extracted from the autospectral density tensor. For example, $E_{22}(k_1)$, the spectra of u_2 (transverse) velocity fluctuations measured in the x_1 direction is defined by

$$E_{22}(k_1) = 2\int_{-\infty}^{\infty} \Phi_{22}(\boldsymbol{k})dk_2, \tag{B.46}$$

and $E_{11}(k_1)$, the spectra of u_1 (longitudinal) velocity fluctuations in the x_1 direction is defined by

$$E_{11}(k_1) = 2\int_{-\infty}^{\infty} \Phi_{11}(\boldsymbol{k})dk_2. \tag{B.47}$$

B.4.1 2D Isotropic Turbulence

In 2D isotropic turbulence, the energy spectrum function $E(k)$ contains all the information in the autospectral density tensor $\Phi_{ij}(\boldsymbol{k})$. As in the 3D case (*Pope* (2000), pp. 222), directional information in $\Phi_{ij}(\boldsymbol{k})$ can only be contained in $\boldsymbol{k}$ and scalar multiples thereof. Thus

$$\Phi_{ij}(\boldsymbol{k}) = A(k)\delta_{ij} + B(k)k_ik_j, \tag{B.48}$$

because δ_{ij} and k_ik_j are the only second order tensors that can be formed from $\boldsymbol{k}$. Multiplying Equation B.48 by k_i and noting incompressibility, $k_i\Phi_{ij}(\boldsymbol{k}) = 0$, gives

$$B(k) = -A(k)/k^2. \tag{B.49}$$

Substituting B.49 into B.48 and then into B.45 gives

$$E(k) = \oint \tfrac{1}{2}A(k)\left(\delta_{ii} - \frac{k_ik_i}{k^2}\right)d\mathcal{L}(k). \tag{B.50}$$

Noting that

$$\oint d\mathcal{L}(k) = 2\pi k, \qquad \text{and} \qquad \oint k_ik_j d\mathcal{L}(k) = \pi k^3\delta_{ij}, \tag{B.51}$$

Equation B.50 can be reduced to

$$A(k) = \frac{E(k)}{\pi k}. \tag{B.52}$$

Substituting B.52 and B.49 into B.48 gives an expression for the autospectral density tensor in terms of the energy spectrum function for 2D turbulence,

$$\Phi_{ij}(\boldsymbol{k}) = \frac{E(k)}{\pi k}\left(\delta_{ij} - \frac{k_i k_j}{k^2}\right). \tag{B.53}$$

This differs by a factor of $1/(4k)$ from the analogous 3D representation, Equation B.14.

Now it is possible to write an expression for the one dimensional longitudinal spectrum, $E_{11}(k_1)$ in terms of the energy spectrum function $E(k)$ by substituting B.53 into B.47 to get

$$E_{11}(k_1) = \frac{4}{\pi}\int_0^\infty \frac{E(k)}{k}\left(1 - \frac{k_1^2}{k^2}\right) dk_2. \tag{B.54}$$

Here $k^2 = k_1^2 + k_2^2$, so $k_2 dk_2 = k dk$, for constant k_1. This allows B.54 to be re-written as

$$E_{11}(k_1) = \frac{4}{\pi}\int_{k_1}^\infty \frac{E(k)}{k}\left(1 - \frac{k_1^2}{k^2}\right)^{1/2} dk. \tag{B.55}$$

Similar expressions can be derived for the one-dimensional transverse spectrum, $E_{22}(k_1)$;

$$E_{22}(k_1) = \frac{4}{\pi}\int_0^\infty \frac{E(k)}{k}\left(1 - \frac{k_2^2}{k^2}\right) dk_2, \tag{B.56}$$

which can be re-written as

$$E_{22}(k_1) = \frac{4}{\pi}\int_{k_1}^\infty E(k)\frac{k_1^2}{k^2}\left(k^2 - k_1^2\right)^{-1/2} dk \tag{B.57}$$

Using the inertial range form for the energy spectrum function,

$$E(k) = C\epsilon^{2/3}k^{-5/3}, \tag{B.58}$$

Equations B.54 and B.56 can be numerically reduced to

$$E_{11}(k_1) \simeq 0.535 C\epsilon^{2/3}k^{-5/3} \tag{B.59}$$

and

$$E_{22}(k_1) \simeq 0.892 C\epsilon^{2/3}k^{-5/3}. \tag{B.60}$$

Assuming a general energy spectrum of the form $E(k) = ak^{-\alpha}$, a relationship between longitudinal and transverse velocity spectra can be found;

$$\alpha E_{11}(k_1) = E_{22}(k_1). \tag{B.61}$$

B.4.2 Vorticity spectra in 2D turbulence

In 2D turbulence, the vorticity correlation tensor in Equation B.21 simplifies to

$$Q(\boldsymbol{r}) = \overline{\omega_3(\boldsymbol{x})\omega_3(\boldsymbol{x}+\boldsymbol{r})}, \tag{B.62}$$

which is not a tensor, but rather a function of $\boldsymbol{r}$. The vorticity correlation function $Q(\boldsymbol{r})$ can be re-written in terms of the velocity correlation tensor $R_{ij}(\boldsymbol{r})$ as

$$\begin{aligned} Q(\boldsymbol{r}) &= \epsilon_{ij}\epsilon_{kl}\overline{\frac{\partial u_j(\boldsymbol{x})}{\partial x_i}\frac{\partial u_l(\boldsymbol{x'})}{\partial x'_k}} && \text{(B.63)} \\ &= -\left(\delta_{ik}\delta_{jl} - \delta_{il}\delta_{jk}\right)\frac{\partial^2 R_{jl}(\boldsymbol{r})}{\partial r_i \partial r_k} && \text{(B.64)} \end{aligned}$$

where $\boldsymbol{x'} = \boldsymbol{x} + \boldsymbol{r}$. Noting continuity,

$$\frac{\partial R_{ij}}{\partial r_i} = \frac{\partial R_{ij}}{\partial r_j} = 0, \tag{B.65}$$

Equation B.64 simplifies to

$$Q(\boldsymbol{r}) = -\delta_{ik}\delta_{jl}\frac{\partial^2 R_{jl}(\boldsymbol{r})}{\partial r_i \partial r_k} = -\nabla^2 R_{ll}(\boldsymbol{r}). = -\nabla^2\left(R_{11}(\boldsymbol{r}) + R_{22}(\boldsymbol{r})\right). \tag{B.66}$$

The expression for the vorticity spectra $\Omega(\boldsymbol{r})$ is then defined in terms of $Q(\boldsymbol{r})$ via the Fourier transform pair

$$\Omega(\boldsymbol{k}) = \mathcal{F}\left\{Q(\boldsymbol{r})\right\} = \frac{1}{(2\pi)^2}\iint_{-\infty}^{\infty} Q(\boldsymbol{r})e^{-i\boldsymbol{k}\cdot\boldsymbol{r}}d\boldsymbol{r}, \tag{B.67}$$

and its inverse

$$Q(\boldsymbol{r}) = \mathcal{F}^{-1}\left\{\Omega(\boldsymbol{k})\right\} = \frac{1}{(2\pi)^2}\iint_{-\infty}^{\infty} \Omega(\boldsymbol{k})e^{i\boldsymbol{k}\cdot\boldsymbol{r}}d\boldsymbol{k}. \tag{B.68}$$

Substituting B.66 into B.67 gives

$$\Omega(\boldsymbol{k}) = k^2\Phi_{ll}(\boldsymbol{k}) = k^2\left(\Phi_{11}(\boldsymbol{k}) + \Phi_{22}(\boldsymbol{k})\right), \tag{B.69}$$

which, using Equation B.53, can be written in terms of the energy spectrum function as

$$\Omega(\boldsymbol{k}) = k^2 \frac{E(k)}{k\pi} \left(1 - \frac{k_1^2}{k^2} + 1 - \frac{k_2^2}{k^2}\right) = \frac{kE(k)}{\pi}. \tag{B.70}$$

Directional vorticity spectra, $\phi_\omega(k_1)$ can then be written as

$$\phi_\omega(k_1) = \int_{-\infty}^{\infty} \Omega(\boldsymbol{k}) dk_2 = \frac{2}{\pi} \int_0^{\infty} kE(k) dk_2 = \frac{2}{\pi} \int_{k_1}^{\infty} \frac{k^2 E(k)}{(k^2 - k_1^2)^{1/2}} dk. \tag{B.71}$$

Appendix C

Instrument wakes in a wave field with a mean flow.

It is instructive to attempt to estimate very roughly the levels of dissipation that might be expected in wake of the LTMIs.

Measurements by *Lien and Sanford* (2009) of dissipation in the wake of a cylindrical bridge piling produced a nondimensional dissipation rate of

$$\frac{\epsilon}{u_\infty^3/d} = 0.01(x_*/12)^{-3}, \tag{C.1}$$

or alternatively

$$\frac{\epsilon}{u_\infty^3/d} = 0.008e^{-(x_*-12)/10}. \tag{C.2}$$

Here u_∞ is the far-field mean velocity, d is diameter of the cylinder, and $x_* = x/d$ with x being the downstream distance from the cylinder. For downstream distances between 10 and 50 d, both of these empirical fits to the data give similar results.

Choosing the second of these relations and re-writing to solve for dissipation gives

$$\epsilon = 0.008\frac{u_\infty^3}{d}e^{-(x/d-12)/10}. \tag{C.3}$$

It is then possible to estimate the order of magnitude of dissipation found in the wake of an instrument. Using values from SoCal 2010, for the period starting 2010/12/06 23:00 [UTC], of $H_s = 1.2$ m, $T_p = 5.1$ s, and a mean LTMI depth of 1 m, linear theory would predict orbital motions, at the depth of the instrument,

with a radius of 0.35 m and a velocity of 0.43 m/s. Using $d = 0.075$ m, the diameter of an Aquadopp, $u_\infty = 0.43$ m/s, and $d = 2\pi 0.35$ m, then gives a dissipation value of $\epsilon = 1.5 \times 10^{-3}$ m^2/s^3.

While this estimate of dissipation in a wake is very simplistic, it does make the point that wake turbulence must be considered. The calculated wake dissipation is a similar order of magnitude to the strong intermittent events shown in figure 5.7, and is two orders of magnitude larger than the background dissipation level.

It should also be noted that the results of *Lien and Sanford* (2009) were for conditions with Reynolds numbers of $\mathcal{O}(10^7)$, whereas the wake being discussed here has a Reynolds number $\mathcal{O}(10^4)$. This vast difference may affect the nondimensionalized dissipation.

Appendix D

Energy input definitions

Energy input has units of energy flux divided by density. Three different descriptions of energy input have been used in this work.

The first is integrated wave-field dissipation, F_{ds}, defined

$$F_{dsJ} = -g \int S_{dsJ}(k) dk, \tag{D.1}$$

where S_{ds} is from *Romero and Melville* (2010), and based on *Alves and Banner* (2003). Wind input for the model was calculated using the formulation of *Janssen* (1991). The corresponding wind input into the wave field is given by

$$F_{inJ} = -g \int S_{inJ}(k) dk. \tag{D.2}$$

Second, the wind input used by *Terray et al.* (1996), and *Drennan et al.* (1996), was defined as the integral of the growth rate, β, over the wave spectrum,

$$F_{TD} = g \int \beta S_{\eta\eta}(\sigma, \theta) d\sigma d\theta. \tag{D.3}$$

Here $S_{\eta\eta}(\sigma, \theta)$ was the directional frequency spectrum and either measured directly or derived from the 1D frequency spectrum using the $\mathrm{sech}^2(\alpha\theta)$ directional distribution of *Donelan et al.* (1985). The growth rate was parameterized with the formulation of *Donelan and Pierson* (1987).

A third energy input description is a simple parameterization in terms of wind stress (*Gemmrich et al.* 1994).

$$F_{ws} \equiv \tau c_{eff}/\rho_w \approx u_{*w}^2 c_{eff} \tag{D.4}$$

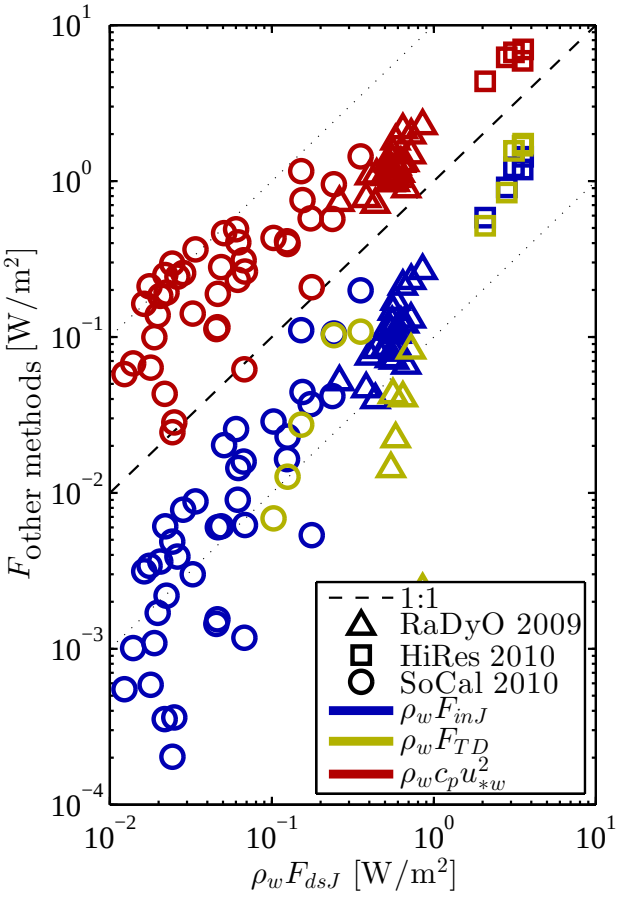

Figure D.1: Comparison of energy flux using three different energy input formulations. Fewer F_{TD} data are visible as that formulation frequently produced negative energy fluxes at low wave ages.

Comparisons with F_{TD} by *Terray et al.* (1996) found the ratio c_{eff}/c_p ranged from approximately $c_{eff}/c_p = 0.1$ for wave ages of 25 to approximately $c_{eff}/c_p = 0.5$ for wave ages of 12 and below.

A comparison of these energy inputs is given in figure D.1. It can be seen that as the energy flux increases (in this case corresponding to increasing wind and decreasing wave age), agreement between all three inputs improves.

References

Agrawal, Y., and C. Belting (1988), Laser velocimetry for benthic sediment transport, *Deep Sea Research Part A. Oceanographic Research Papers*, *35*(6), 1047 – 1068, doi:10.1016/0198-0149(88)90076-3.

Agrawal, Y. C., E. A. Terray, M. A. Donelan, P. A. Hwang, A. J. W. III, W. M. Drennan, K. K. Kahma, and S. A. Krtaigorodskii (1992), Enhanced dissipation of kinetic energy beneath surface waves, *Nature*, *359*, 219–220.

Alves, J. H. G. M., and M. L. Banner (2003), Performance of a saturation-based dissipation-rate source term in modeling the fetch-limited evolution of wind waves, *Journal of Physical Oceanography*, *33*, 1274–1298.

Anis, A., and J. Moum (1992), The superadiabatic surface layer of the ocean during convection, *Journal of Physical Oceanography*, *22*(10), 1221–1227.

Antonia, R. A., L. W. B. Browne, and D. A. Shah (1988), Characteristics of vorticity fluctuations in a turbulent wake, *Journal of Fluid Mechanics*, *189*, 349–365.

Banner, M., and W. L. Peirson (2007), Wave breaking onset and strength for two-dimensional deep-water wave groups, *Journal of Fluid Mechanics*, *585*, 93–115.

Banner, M. L., and D. H. Peregrine (1993), Wave breaking in deep water, *Annual Review of Fluid Mechanics*, *25*, 373–397.

Banner, M. L., I. S. F. Jones, and J. C. Trinder (1989), Wavenumber spectra of short gravity waves, *Journal of Fluid Mechanics*, *198*, 321–344.

Banner, M. L., J. R. Gemmrich, and D. M. Farmer (2002), Multiscale measurements of ocean wave breaking probability, *Journal of Physical Oceanography*, *32*, 3364–3375.

Batchelor, G. K. (1953), *The Theory of Homogeneous Turbulence*, Cambridge at the University Press.

Bendat, J. S., and A. G. Piersol (2010), *Random Data Analysis and Measurement Procedures*, Wiley.

Benetazzo, A. (2006), Measurements of short water waves using stereo matched image sequences, *Coastal Engineering*, *53*, 1013–1032.

Bouguet, J.-Y. (2010), Camera calibration toolbox for matlab, Website: `http://www.vision.caltech.edu/bouguetj/calib_doc/`.

Chickadel, C. C., S. A. Talke, A. R. Horner-Devine, and A. T. Jessup (2011), Infrared-based measurements of velocity, turbulent kinetic energy, and dissipation at the water surface in a tidal river, *IEEE Geoscience and Remote Sensing Letters*, *PP*, 849.

Corpetti, T., E. Memin, and P. Perez (2003), Extraction of singular points from dense motion fields: An analytic approach, *Journal of Mathematical Imaging and Vision*, *19*, 175–198.

Dickey, T., et al. (2012), Introduction to special section on recent advances in the study of optical variability in the near-surface and upper ocean, *Journal of Geophysical Research*, *117*, C00H20, doi:10.1029/2012JC007964.

Dillon, T. M., and D. R. Caldwell (1980), The batchelor spectrum and dissipation in the upper ocean, *Journal of Geophysical Research*, *85*, 1910–1916.

Donelan, M. A., and W. J. Pierson (1987), Radar scattering and equilibrium ranges in wind-generated waves with application to scatterometry, *Journal of Geophysical Research*, *92*, 4971–5029.

Donelan, M. A., J. Hamilton, and W. H. Hui (1985), Directional spectra of wind-generated waves, *Philosophical Transactions of the Royal Society of London. Series A, Mathematical and Physical Sciences*, *315*(1534), 509–562.

Donlon, C. J., and I. S. Robinson (1997), Observations of the oceanic thermal skin in the atlantic ocean, *Journal of Geophysical Research*, *102*(C8), 18,585–18,606, doi:10.1029/97JC00468.

Drazen, D. A., W. K. Melville, and L. Lenain (2008), Inertial scaling of dissipation in unsteady breaking waves, *Journal of Fluid Mechanics*, *611*, 307–332.

Drennan, W., M. Donelan, E. Terray, and K. Katsaros (1996), Oceanic turbulence dissipation measurements in swade, *Journal of Physical Oceanography*, *26*(5), 808–815.

Duncan, J. H. (1981), An experimental investigation of breaking waves produced by a towed hydrofoil, *Proceedings of the Royal Society of London A*, *377*, 331–348.

Duncan, J. H. (2001), Spilling breakers, *Annual Review of Fluid Mechanics*, *33*, 519–547.

Elgar, S., B. Raubenheimer, and R. T. Guza (2005), Quality control of acoustic doppler velocimeter data in the surfzone, *Measurement Science and Technology*, *16*(10), 1889.

Fusiello, A., and L. Irsara (2008), Quasi-euclidean uncalibrated epipolar rectification, in *International Conference on Pattern Recognition (ICPR)*.

Garbe, C. S., H. Spies, and B. Jähne (2003), Estimation of complex motion from thermographic image sequences, in *Thermosense XXV*, vol. 5073, edited by K. E. Cramer and X. P. Maldague, pp. 303–317, Proceedings of the SPIE.

Gargett, A. E. (1989), Ocean turbulence, *Annual Review of Fluid Mechanics*, *21*, 419–451.

Gargett, A. E. (1994), Observing turbulence with a modified acoustic doppler current profiler, *Journal of Atmospheric and Oceanic Technology*, *11*, 1592–1610.

Gargett, A. E. (1999), Velcro measurement of turbulence kinetic energy dissipation rate , *Journal of Atmospheric and Oceanic Technology*, *12*, 1973–1993.

Gargett, A. E., T. R. Osborn, and P. W. Nasmyth (1984), Local isotropy and the decay of turbulence in a stratified fluid, *Journal of Fluid Mechanics*, *144*, 231–280.

Gemmrich, J. (2010), Strong turbulence in the wave crest region, *Journal of Physical Oceanography*, *40*, 583–595.

Gemmrich, J. R., and D. M. Farmer (2004), Near-surface turbulence in the presence of breaking waves, *Journal of Physical Oceanography*, *34*, 10671086.

Gemmrich, J. R., T. D. Mudge, and V. D. Polonichko (1994), On the energy input from wind to surface waves, *Journal of Physical Oceanography*, *24*, 2413–2417.

Gemmrich, J. R., M. L. Banner, and C. Garrett (2008), Spectrally resolved energy dissipation rate and momentum flux of breaking, *Journal of Physical Oceanography*, *38*, 1296–1312.

Gerbi, G. P., J. H. Trowbridge, E. A. Terray, A. J. Plueddemann, and T. Kukulka (2009), Observations of turbulence in the ocean surface boundary layer: Energetics and transport, *Journal of Physical Oceanography*, *39*(5), 1077–1096.

Gonzalez, R. C., R. E. Woods, and S. L. Eddins (2009), *Digital Image Processing Using MATLAB*, Gatesmark Publishing.

Grant, H. L., R. W. Stewart, and A. Moilliet (1962), Turbulence spectra from a tidal channel, *Journal of Fluid Mechanics*, *12*(02), 241–268, doi:10.1017/S002211206200018X.

Grant, H. L., B. A. Hughes, W. M. Vogel, and A. Moilliet (1968a), The spectrum of temperature fluctuations in turbulent flow, *Journal of Fluid Mechanics*, *34*, 423–442.

Grant, H. L., A. Moilliet, and W. M. Vogel (1968b), Some observations of the occurrence of turbulence in and above the thermocline, *Journal of Fluid Mechanics*, *34*(03), 443–448, doi:10.1017/S0022112068002004.

Hartley, R., and A. Zisserman (2003), *Multiple View Geometry in Computer Vision*, Cambridge University Press.

Hasselmann, K. (1962), On the non-linear energy transfer in a gravity-wave spectrum part 1. general theory, *Journal of Fluid Mechanics*, *12*, 481–500.

Hilsenstein, V. (2005), Surface reconstruction of water waves using thermographic stereo imaging, in *Proceedings of Image and Vision Computing New Zealand (IVCNZ 2005)*, pp. 102–107, Dunedin, New Zealand, 28-29 November 2005.

Holmes, Q. A., D. R. Nuesch, and R. A. Shuchman (1984), Textural analysis and real-time classification of sea-ice types using digital sar data, *IEEE Transactions on Geoscience and Remote Sensing*, *GE-22*(2), 113 –120, doi:10.1109/TGRS.1984.350602.

IPCC (2007), *Climate Change 2007*, Intergovernmental Panel on Climate Change.

Jähne, B., J. Klinke, and S. Waas (1994), Imaging of short ocean wind waves: a critical theoretical review, *Journal of the Optical Society of America A*, *11*(8), 2197–2209.

Janssen, P. A. E. M. (1991), Quasi-linear theory of wind-wave generation applied to wave forecasting, *Journal of Physical Oceanography*, *21*, 1631–1642.

Jessup, A. T., and K. R. Phadnis (2005), Measurement of the geometric and kinematic properties of microscale breaking waves from infrared imagery using a piv algorithm, *Measurement Science and Technology*, *16*, 1961–1969.

Jessup, A. T., C. J. Zappa, M. R. Loewen, and V. Hesany (1997), Infrared remote sensing of breaking waves, *Nature*, *385*, 52–55.

Kitaigorodskii, S., M. Donelan, J. Lumley, and E. Terray (1983), Wave-turbulence interactions in the upper ocean. part ii. statistical characteristics of wave and turbulent components of the random velocity field in the marine surface layer, *Journal of Physical Oceanography*, *13*(11), 1988–1999.

Kleiss, J. M., and W. K. Melville (2010), Observations of wave breaking kinematics in fetch-limited seas, *Journal of Physical Oceanography*, *40*, 2575–2604.

Kleiss, J. M., and W. K. Melville (2011), The analysis of sea surface imagery for white cap kinematics, *Journal of Atmospheric and Oceanic Technology*, *28*, 219–243.

Kolmogorov, A. N. (1941), The local structure of turbulence in incompressible viscous fluid for very large reynolds numbers, *Doklady Akademii Nauk SSSR*, *30*, 299–303, english translation: A. N. Kolmogorov. The Local Structure of Turbulence in Incompressible Viscous Fluid for Very Large Reynolds Numbers Proc. R. Soc. Lond. A July 8, 1991 434:9-13.

Lacy, J. R., and C. R. Sherwood (2004), Accuracy of a pulse-coherent acoustic doppler profiler in a wave-dominated flow, *Journal of Atmospheric and Oceanic Technology*, *21*, 1448–1461.

Lien, R.-C., and T. Sanford (2009), Vorticity and turbulence in the wake of a bridge pier, *Oceanic Engineering, IEEE Journal of*, *34*(3), 307–314, doi:10.1109/JOE.2009.2019383.

Lindborg, E. (2007), Horizontal wavenumber spectra of vertical vorticity and horizontal divergence in the upper troposphere and lower stratosphere, *Journal of the Atmospheric Sciences*, *64*, 1017–1025.

Lohrmann, A., B. Hackett, and L. P. Røed (1990), High resolution measurements of turbulence, velocity and stress using a pulse-to-pulse coherent sonar, *Journal of Atmospheric and Oceanic Technology*, *7*, 19–37.

Lumley, J., and E. Terray (1983), Kinematics of turbulence convected by a random wave field, *Journal of Physical Oceanography*, *13*(11), 2000–2007.

Ma, Y., S. Soatto, J. Kosecka, and S. S. Sastry (2006), *An Invitation to 3-D Vision: From Images to Geometric Models*, Springer.

Melville, W. K. (1994), Energy dissipation in breaking waves, *Journal of Physical Oceanography*, *42*(10), 2041–2049.

Melville, W. K. (1996), The role of surface-wave breaking in air-sea interaction, *Annual Review of Fluid Mechanics*, *28*, 279–321.

Melville, W. K., and P. Matusov (2002), Distribution of breaking waves at the ocean surface, *Nature*, *417*, 58–63.

Meyer, T., M. Eriksson, and R. Maggio (2001), Gradient estimation from irregularly spaced data sets, *Mathematical Geology*, *33*, 693–717, 10.1023/A:1011026732182.

Mollo-Christensen, E. (1968), *Wind Tunnel Test of the Superstructure of the R/V Flip for Assessment of Wind Field Distortion*, M.I.T. [Department of Meteorology]. Fluid dynamics Laboratory.

Moum, J. N., M. C. Gregg, R. C. Lien, and M. E. Carr (1995), Comparison of turbulence kinetic energy dissipation rate estimates from two ocean microstructure profilers, *Journal of Atmospheric and Oceanic Technology*, *12*(2), 346–366.

Nasmyth, P. W. (1970), *Oceanic Turbulence*, University of British Columbia.

Osborn, T., D. M. Farmer, S. Vagle, S. A. Thorpe, and M. Cure (1992), Measurements of bubble plumes and turbulence from a submarine., *Atmosphere – Ocean (Canadian Meteorological & Oceanographic Society)*, *30*(3), 419 – 440.

Osborn, T. R., and C. S. Cox (1972), Oceanic fine structure, *Geophysical Fluid Dynamics*, *3*, 321–345.

Osborn, T. R., and R. G. Lueck (1985), Turbulence measurements with a submarine, *Journal of Physical Oceanography*, *15*, 1502–1520.

Phillips, O. M. (1985), Spectral and statistical properties of the equilibrium range in wind-generated gravity waves, *Journal of Fluid Mechanics*, *156*, 505–531.

Phillips, O. M., F. L. Posner, and J. P. Hansen (2001), High range resolution radar measurements of the speed distribution of breaking events in wind-generated ocean waves: Surface impulse and wave energy dissipation rates, *Journal of Physical Oceanography*, *31*, 450–460.

Pope, S. B. (2000), *Turbulent Flows*, Cambridge University Press, Cambridge.

Rapp, R. J., and W. K. Melville (1990), Laboratory measurements of deep-water breaking waves, *Philosophical Transactions of the Royal Society of London. Series A, Mathematical and Physical Sciences*, *A331*(1622), 735–800.

Rocholz, R., S.Wanner, U. Schimpf, and B. Jähne (2010), Combined visualization of wind waves and water surface temperature, in *The 6th International Symposium on Gas Transfer at Water Surfaces. Kyoto, Japan, May 17-21, 2010*, edited by S. Komori, W. McGillis, and R. Kurose, pp. 496–506, Kyoto University Press.

Romero, L., and W. K. Melville (2010), Numerical modeling of fetch-limited waves in the gulf of tehuantepec, *Journal of Physical Oceanography*, *3*, 466–486.

Romero, L., W. K. Melville, and J. M. Kleiss (2012), Spectral energy dissipation due to surface-wave breaking, *Journal of Physical Oceanography*, *42*, 1421–1444, doi:http://dx.doi.org/10.1175/JPO-D-11-072.1.

Saddoughi, S. G., and S. V. Veeravalli (1994), Local isotropy in turbulent boundary layers at high reynolds number, *Journal of Fluid Mechanics*, *268*, 333–372, doi: 10.1017/S0022112094001370.

Salmon, R. (1998), *Lectures on Geophysical Fluid Dynamics*, Oxford University Press, New York.

Shemdin, O. H., H. M. Tran, and S. C. Wu (1988), Directional measurement of short ocean waves with stereophotography, *Journal of Geophysical Research*, *93*, 13,891–13,901.

Shen, L., and D. K. P. Yue (2001), Large-eddy simulation of free-surface turbulence, *Journal of Fluid Mechanics*, *440*, 75–116.

Smith, J. A. (2008), Vorticity and divergence of surface velocities near shore, *Journal of Physical Oceanography*, *38*, 1450–1468.

Smith, J. A., and K. F. Rieder (1997), Wave induced motion of flip, *Ocean Engineering*, *24*(2), 95–110.

Taylor, G. I. (1935), Statistical theory of turbulence, *Proceedings of the Royal Society of London. Series A - Mathematical and Physical Sciences*, *151*(873), 421–444, doi:10.1098/rspa.1935.0158.

Tennekes, H., and J. L. Lumley (1972), *A First Course in Turbulence*, The MIT Press.

Terray, E. A., M. A. Donelan, Y. C. Agrawal, W. M. Drennan, K. K. Kahma, A. J. W. III, P. A. Hwang, and S. A. Kitaigorodskii (1996), Estimates of kinetic energy dissipation under breaking waves, *Journal of Physical Oceanography*, *26*(5), 792–807.

Thielicke, W., and E. J. Stamhuis (2010), Pivlab 1.2 - time-resolved digital particle image velocimetry tool for matlab, Website: http://pivlab.blogspot.com/.

Thomson, J. (2012), Wave breaking dissipation observed with 'swift' drifters, *Journal of Atmospheric and Oceanic Technology*, *29*, 1866–1882.

Thomson, J., J. R. Gemmrich, and A. T. Jessup (2009), Energy dissipation and the spectral distribution of whitecaps, *Geophysical Research Letters*, *36*(11), L11,601, doi:10.1029/2009GL038201.

Turney, D. E., A. Andere, and S. Banerjee (2009), A method for three-dimensional interfacial particle image velocimetry (3d-ipiv) of an airwater interface, *Measurement Science and Technology*, *20*, 045,403.

Veron, F., and W. K. Melville (1999), Pulse-to-pulse coherent doppler measurements of waves and turbulence, *Journal of Atmospheric and Oceanic Technology*, *16*(11), 1580–1597.

Veron, F., W. K. Melville, and L. Lenain (2008), Infrared techniques for measuring ocean surface processes, *Journal of Atmospheric and Oceanic Technology*, *25*, 307–326.

Veron, F., W. K. Melville, and L. Lenain (2009), Measurements of ocean surface turbulence and waveturbulence interactions, *Journal of Physical Oceanography*, *39*, 2310–2323.

Wiles, P. J., T. P. Rippeth, J. H. Simpson, and P. J. Hendricks (2006), A novel technique for measuring the rate of turbulent dissipation in the marine environment, *Geophysical Research Letters*, *33*, L21,608.

WISE, et al. (2007), Wave modelling the state of the art, *Progress in Oceanography*, *75*, 603–674.

Zappa, C. J., W. E. Asher, and A. T. Jessup (2001), Microscale wave breaking and air-water gas transfer, *Journal of Geophysical Research*, *106*(C5), 9385–9391, doi:10.1029/2000JC000262.

Zappa, C. J., M. L. Banner, H. Schultz, J. R. Gemmrich, R. P. Morison, D. A. LeBel, and T. Dickey (2012), An overview of sea state conditions and air-sea fluxes during radyo, *Journal of Geophysical Research*, *117*(C7), C00H19, doi: 10.1029/2011JC007336.